Matrix Permeability of Reservoir Rocks, Ngatamariki Geothermal Field, Taupo Volcanic Zone, New Zealand

---

A thesis submitted in partial fulfilment of the requirements for the degree

of

Master of Science in Engineering Geology

at the

University of Canterbury

by

Joseph Liam Cant

Department of Geological Sciences,

University of Canterbury,

Christchurch, New Zealand

2015

Abstract

Sixteen percent of New Zealand's power comes from geothermal sources which are primarily located within the Taupo Volcanic Zone (TVZ). The TVZ hosts twenty three geothermal fields, seven of which are currently utilised for power generation. Ngatamariki Geothermal Field is the latest geothermal power generation site in New Zealand, located approximately 15 km north of Taupo. This was the location of interest in this project, with testing performed on a range of materials to ascertain the physical properties and microstructure of reservoir rocks. The effect of burial diagenesis on the physical properties was also investigated.

Samples of reservoir rocks were taken from the Tahorakuri Formation and Ngatamariki Intrusive Complex from a range of wells and depths (1354-3284 mbgl). The samples were divided into four broad lithologies: volcaniclastic lithic tuff, primary tuff, welded ignimbrite and tonalite. From the supplied samples twenty one small cylinders (~40-50mm x 20-25mm) were prepared and subjected to the following analyses: dual weight porosity, triple weight porosity, dry density, ultrasonic velocity (saturated and dry) and permeability (over a range of confining pressures). Thin sections impregnated with an epoxy fluorescent dye were created from offcuts of each cylinder and were analysed using polarised light microscopy and quantitative fluorescent light microstructural microscopy.

The variety of physical testing allowed characterisation of the physical properties of reservoir rocks within the Ngatamariki Geothermal Field. Special attention was given to the petrological and mineralogical fabrics and their relation to porosity and matrix permeability. It was found that the pore structures (microfractures or vesicles) had a large influence on the physical properties. Microfractured samples were associated with low porosity and permeability, while the vesicular samples were associated with high porosity and permeability. The microfractured samples showed progressively lower permeability with increased confining pressure whereas samples with a vesicular microstructure showed little response to increased confining pressure.

An overall trend of decreasing porosity and permeability with increasing density and sonic velocity was observed with depth, however large fluctuations with depth indicate this trend may be uncertain. The large variations correlate with changes in lithology suggest that the lithology is the primary control of the physical properties with burial diagenesis being a subsidiary factor.

This project has established a relationship between the microstructure and permeability, with vesicular samples showing high permeability and little response increased confining pressure. The effects of burial diagenesis on the physical properties are subsidiary to the observed variations in lithology. The implications of these results suggest deep drilling in the Tahorakuri Formation may reveal unexploited porosity and permeability at depth.

Acknowledgements

Firstly I would like to thank Prof. Jim Cole and Dr Paul Siratovich for the amount of time and effort you have put into me and my project. Jim thanks for always having an open door and a quick turn around on anything that I might give you. Your knowledge of the TVZ blows me away and has been invaluable. Paul thanks for your help with the permeameter and passing along some of your understanding of permeability. Your brutal but well thought out edits and the occasional dress up party have helped me immensely.

Mighty River Power, you have given me the opportunity to do this project through a scholarship and allowing me to play with some of your rocks, and for that I am exceedingly grateful. Maxwell Wilmarth for showing me around the Ngatamariki Field, sorting out extra samples and your feedback has been priceless.

Thanks to the team on the first floor, Rob, Kathy, Janet, and Sarcha. Your help with the testing of samples saved me lots of heart ache and reduced my learning curve.

To all my friends in 401, and spread out across the fourth floor, thanks for keeping me going and providing endless humours and in depth conversations. Also for constantly helping me find that special word that's stuck on the tip of my tongue for 20 minutes!

Lastly I would like to thank my partner Kate, your support though the last two years has been nothing short of amazing. Your ability to cheer me up after a long day has made this project so much smoother. Love you long time.

Table of Contents

Table of Figures

1 Introduction

1.1 Project Background

Geothermal systems are the near surface expression of the interaction of groundwater with a magmatic intrusions, volcanic activity or an evenly distributed heat source near the surface (Glassley 2010).

Geothermal power accounts for approximately 16% of New Zealand's power generation (GNS 2014) and provides a renewable and reliable method of power generation. Geothermal power generation is a relatively new power source, with the first geothermal power generation plant constructed in 1904 at Larderello, Italy. Initially the steam was captured as it carried boric acid in suspension. The steam was originally used to further concentrate the acid. In 1904 a small steam engine was installed which drove a dynamo powering several lamp. A larger steam engine was installed in 1905 with a turbine installed in 1912 and further equipment being continually added to the point where over 100,000 kw of power being generated by 1941 (Keller & Valduga 1946). This remained the only geothermal power plant until 1958, when the high-temperature geothermal field in Wairakei, New Zealand, was commissioned (Modriniak & Studt 1959). The majority of New Zealand's geothermal resources are located in the Taupo Volcanic Zone (TVZ) which contains 23 high temperature (>250°C) geothermal fields within Quaternary pyroclastic basins (Bertrand et al. 2013). Seven of these fields have become geothermal power generation sites. The site of interest for this study is the Ngatamariki Geothermal Field (NGF) located approximately 15km north of Taupo (Figure 1.1).

Understanding the nature and behaviour of the geothermal reservoir at Ngatamariki is of upmost importance for the efficiency and longevity of the geothermal resource. Two key properties are porosity and permeability. Porosity is the measure of pore volume (empty space) within the rock

(or any other medium) and permeability indicates how easily a fluid can pass through a medium (Gueguen & Placiauskas 1994). Porosity does not provide any indication on the shape, size, distribution or degree of connectivity of the pores and therefore provides limited information on fluid flow through the rock. Porosity can be broken in to two distinct groups; connected porosity and unconnected porosity. Unconnected porosity refers to pore spaces that are not interconnected with the rest of the pore network and therefore cannot be accessed by fluids. Connected porosity refers to pore spaces that are interconnected and can therefore contribute to permeability. This study will only focus on connected porosity and all further reference to porosity will be to the connected porosity. The porosity is primarily controlled by rock type, with large differences between intrusive, volcanic and sedimentary rocks. However, within a geothermal system alteration, resorption and mineralisation associated with hydrothermal fluids results in a modified and much more complex system. Permeability is a quantitative description of fluid flow within a porous media that was put forward by Henry Darcy in the mid 1800s that applies to slow moving non-turbulent (Darcian) flow (Glassley 2010). It is largely scale dependant with a distinct differences between macro (large scale fractures) and micro (matrix) scale permeability. This can be partially attributed to the random distribution of pore characters throughout a rock mass (Glassley 2010). A common approach to modelling a geothermal system is to assume dual porosity/permeability where two interactive continua, matrix and fracture permeability, are assumed to have their own unique properties (Jafari & Babadagli 2011). Natural fractures within a geothermal system resulting from, unconformities, cooling joints and tectonic stresses strongly control fluid flow due to their high permeability (Murphy et al. 2004) and generally control the permeability in geothermal systems (Jafari & Babadagli 2011). Testing of macro scale fracture permeability is generally done in-situ with the use of injection flow rate tests which are used to identify areas of high permeability associated with fractured zones (Watson 2013). In this study only micro scale properties (i.e. matrix) have been studied. This was chosen as it does not require in-situ testing and can be completed in a laboratory with recovered core samples, it is also a property that can be overlooked in terms of reservoir modelling. To quantify the micro scale properties, detailed testing and analysis was completed, with special attention focused on porosity and permeability.

A high pressure and temperature Core Lab Pulse Decay Permeameter-200 has been used to test permeability. This machine can simulate pressure conditions that samples would have been subject to while in the deep reservoir environment. From the testing, we expect to ascertain the effects of different confining pressures on the matrix permeability of the tested samples. This testing is

completed alongside other rock property testing methods such as, dual weight porosity, triple weight porosity, dry density, ultrasonic compression wave (Vp) and shear wave (Vs) velocities. Thin section analysis has been performed on all samples tested to identify key mineralogy associated with hydrothermal fluids through the use of polarised light microscopy. Microstructural analysis was performed using fluorescent light microscopy that identifies areas of connected porosity therefore showing the nature of the microfractures and vesicles found within the samples.

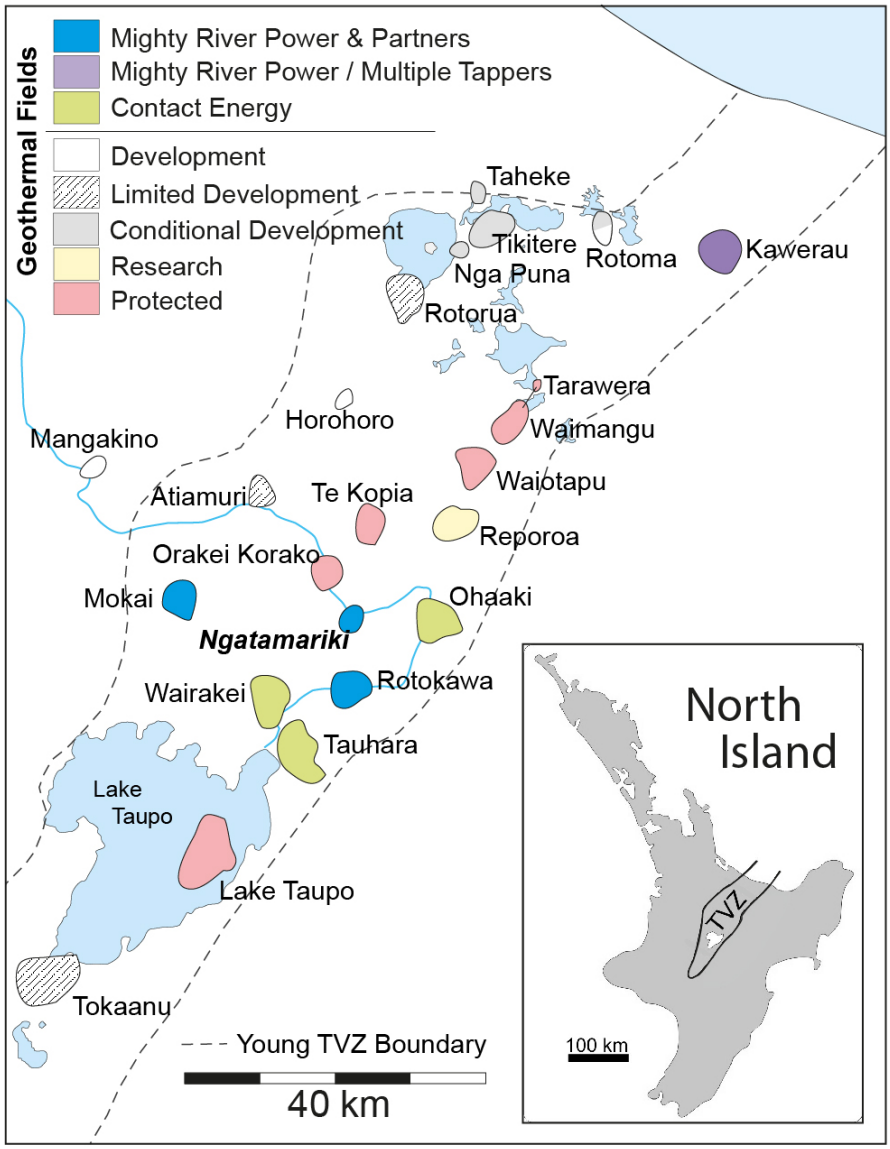

Figure 1.1: Known geothermal fields within the TVZ as defined by the resistivity boundaries given by Bibby et al. (1995) and the TVZ boundary by Wilson et al. (1995), original figure (Catherine Boseley 2010)

1.2 Project Objectives

The overall goal of this thesis is to establish the physical properties of the Tahorakuri Formation and Ngatamariki Intrusive Complex found at the NGF through non-destructive test methods. From the results of the testing, the intent is to answer the following questions:

- Are the physical and mechanical properties of the Tahorakuri Formation intrinsically linked to variation in lithology?
- What are the controlling factors of permeability for the samples from Ngatamariki?
- Does burial diagenesis have an effect on the physical and mechanical properties?
- Is there potential for further development of the geothermal resource (based off project findings)?

1.3 Previous Studies

Previous studies e.g. (Heard & Page 1982; Bourbie & Zinszner 1985; Rust & Cashman 2004; Stimac et al. 2004; Heap et al. 2014) show that porosity and matrix permeability are closely related, with high porosity values correlating to high permeability. However, it is important to note that permeability is not controlled by porosity but rather by the pore microstructure and morphology. Pore geometry plays a large role with pressure-dependent permeability, as fractures are more easily closed than isotropic pores (Guéguen & Palciauskas 1994). This results in fractured samples showing larger decrease in permeability (Bernabe 1986) when compared to samples with isotropic pores (David & Darot 1990). Nara et al. (2011) found high aspect ratio (length:width) microfractures maintaining their influence on permeability even at high confining pressure. They also found low aspect ratio macrofractures are associated with relatively high permeability at low confining pressures but are easily closed by increased confining pressures. Within the Tiwi Geothermal Fields (Philippines), a trend of lower porosity with depth was found within the studied geothermal system (from ~10% at the top of the reservoir to 2.5% at the bottom). This was ascribed to the increased overburden stresses and chemical reactions within the geothermal fluids. However, within this trend there was a large fluctuation in porosity associated with the localised variation in, texture, tectonic stresses and hydrothermal processes. The principal control on

porosity in the near surface rocks was found to be the primary lithology. Within the deeply buried and hydrothermally altered volcanic sequences it was found that primary lithology played a smaller role and that burial diagenesis and hydrothermal alteration significantly reduced the porosity (Stimac et al. 2004).

1.4 Geological Setting

The study area of this project is within the TVZ, located in the North Island of New Zealand. This is a zone of arc-related volcanism and extension associated with the subduction of the Pacific plate beneath the Australian plate. This commences to the east of the North Island at the Hikurangi Trench (Spinks et al. 2005). In the TVZ the two plates are obliquely converging at approximately 42 mm/year (Reyners et al. 2006). However the lithosphere in the central TVZ is extending at an average rate of 8 ± 2 mm/yr with up to 15 mm/yr in some areas. The extension rate is much greater than can be accounted for by seismic strain alone (Darby et al. 2000). This has caused the continental crust within the TVZ to become substantially thinner than most continental crusts with an estimated thickness between 15-20 km (Bibby et al. 1995; Cole & Spinks 2009). The TVZ extends from White Island in the north east to Ohakune in the south west and covers an area of 17,500 km^2 (Bibby et al. 1995). Over the last 2 Ma, 20,000 km^3 of volcanic material has been erupted from the central TVZ. In fact, silicic volcanism in the central TVZ is on the same scale as Yellowstone (USA) in terms of size, longevity, thermal flux and magma output rates (Houghton et al. 1995; Spinks et al. 2005) and over the last 340 Ka the central TVZ has been the most active rhyolitic centre in the world, producing and average of 0.3 m^3s^{-1} of volcanic material (Wilson et al. 1995). The TVZ is divided into 3 distinct segments based on the composition of the erupted material. The north-eastern (White Island) and south-western (Ruapehu and Tongariro) segments of the TVZ are characterised by andesitic to dacitic composite volcanoes while the central section (125 km x 60 km) has erupted overwhelmingly rhyolitic magma (Houghton et al. 1995; Spinks et al. 2005).

The primary reason for TVZ's morphology is the presence of the Wadati-Benioff zone which is located beneath the TVZ at depth of ~80 – 100 km below the surface (Reyners et al. 2006). At this depth, volatiles within the subducted Australian plate cause partial melting within the lithosphere

resulting in a density differential and giving rise to the magmatic systems seen throughout TVZ. These magmatic systems have been active in TVZ for approximately 2 Ma and are dominated by large rhyolitic caldera volcanoes (Cole 1990). It has been found that there exists a positive relationship between extension and eruptive volumes, with pure extension associated with the largest erupted volumes (Spinks et al. 2005). Within the TVZ, localised zones of shallow electrical resistivity have been associated with geothermal fields. These zones exist due to hydrated clays deposited by the circulating geothermal fluids. This method has been used in the mapping of geothermal fields within the TVZ that have little to no surface expression (Bromley 2002). The shallow zones of low resistivity have been correlated with deep resistivity within the basement greywacke (Bibby et al. 1994) inferring upwelling and conductive heat transport through the saline fluids (Bertrand et al. 2013). This method can be used to estimate the extent of the geothermal resource and its location. This suggests that upwelling of high temperature fluid is flowing through zones of fractured basement rock from a deep magmatic source. Dipping conductive zones have been observed connecting the deep and shallow conductive zones within the Ohaaki geothermal system (Bertrand et al. 2013). This form of fluid upwelling through the basement rock may explain the many geothermal hotspots seen throughout the TVZ.

1.5 Ngatamariki Site Geology

The study area is the NGF which is operated as a geothermal power generation site by Mighty River Power Limited. The NGF is sited on the boundary of the Whakamaru Caldera as defined by Wilson et al. (1995). To date twelve production scale boreholes have been drilled at Ngatamariki since 1980 with the most recent completion of NM12 in 2014. Figure 1.2 shows the location of these wells. There are currently four production wells and four injection wells along with the several monitoring wells. Monitoring wells are used primarily to observe the interaction of the hydrothermal system and the nearby protected field of Orakei-Korako.

The subsurface stratigraphy encountered at Ngatamariki has been well described (Bignall 2009; Boseley 2010; Boseley et al. 2012; Chambefort et al. 2014). Table 1.1 shows the encountered stratigraphy at the NGF.

Ngatamariki Stratigraphy		
Formation Name	**Thickness (m)**	**Lithological Description**
Orakonui Formation, (Surficial deposits)	0-10	Pumice breccia, with common volcanic lithics, quartz and minor feldspar.
Orunanui Formation	15-85	Cream to pinkish vitric-lithic tuff, with vesicular pumice and lava lithics, plus quartz feldspar and rare pyroxene crystal fragments.
Huka Falls Formation	>70-285	Coarse to medium grained sandstone, minor gravel (Laminated lacustrine sediments)
Waiora Formation	0-10	An upper level interval of Waiora Formation, comprises pumice-rich vitric tuff, with Volcanic lithics, quartz rare biotite and pyroxene crystals.
Rhyolite lava	115-315	Glassy rhyolite lava, with perlithic textures, Phenocrysts are quartz, feldspar pyroxene and magnetite.
Waiora Formation	0-240	A lower interval of Waiora Formation, comprising pumice rich vitreous tuff, intercalated with crystal tuff, tuffaceous coarse sandstone and tuffaceous siltstone.
Wairakei Ignimbrite	100-200	Crystal-lithic tuff/breccia , with abundant quartz, minor feldspar, rare biotite and pyroxene, minor volcanic lithics and pumice, in a fine ash
Rhyolite lava	0-285	Hard porphyritic quartz-rich rhyolite lava with phenocrysts of quartz, minor feldspar, and minor ferromagnesian minerals.
Tahorakuri Formation (Tuffs and sediments)	460-700	White to pale grey lithic tuff/breccia intercalated with fine sediments. In NM6 it is intercalated with 310 m of andesite lavas and breccias.
Tahorakuri Formation (Akaterewa Ignimbrite)	>200-840	Play grey, lithic tuff/breccia containing dark grey/brown lava, rhyolite pumice grey wacke-argillite and sandstone clasts in a silty matrix.
Tahorakuri Formation (andesite lava, breccia)	>830	Pale grey porphyritic (feldspar, pyroxene and amphibole andesite lava and breccia
Torlesse greywacke	Undefined	Pale grey to grey, massive meta-sandstone which lack obvious bedding, quartz veins

Table 1.1 Subsurface Lithology of Ngatamariki as determined from Borehole NM1-7 as described by Bignall (2009)

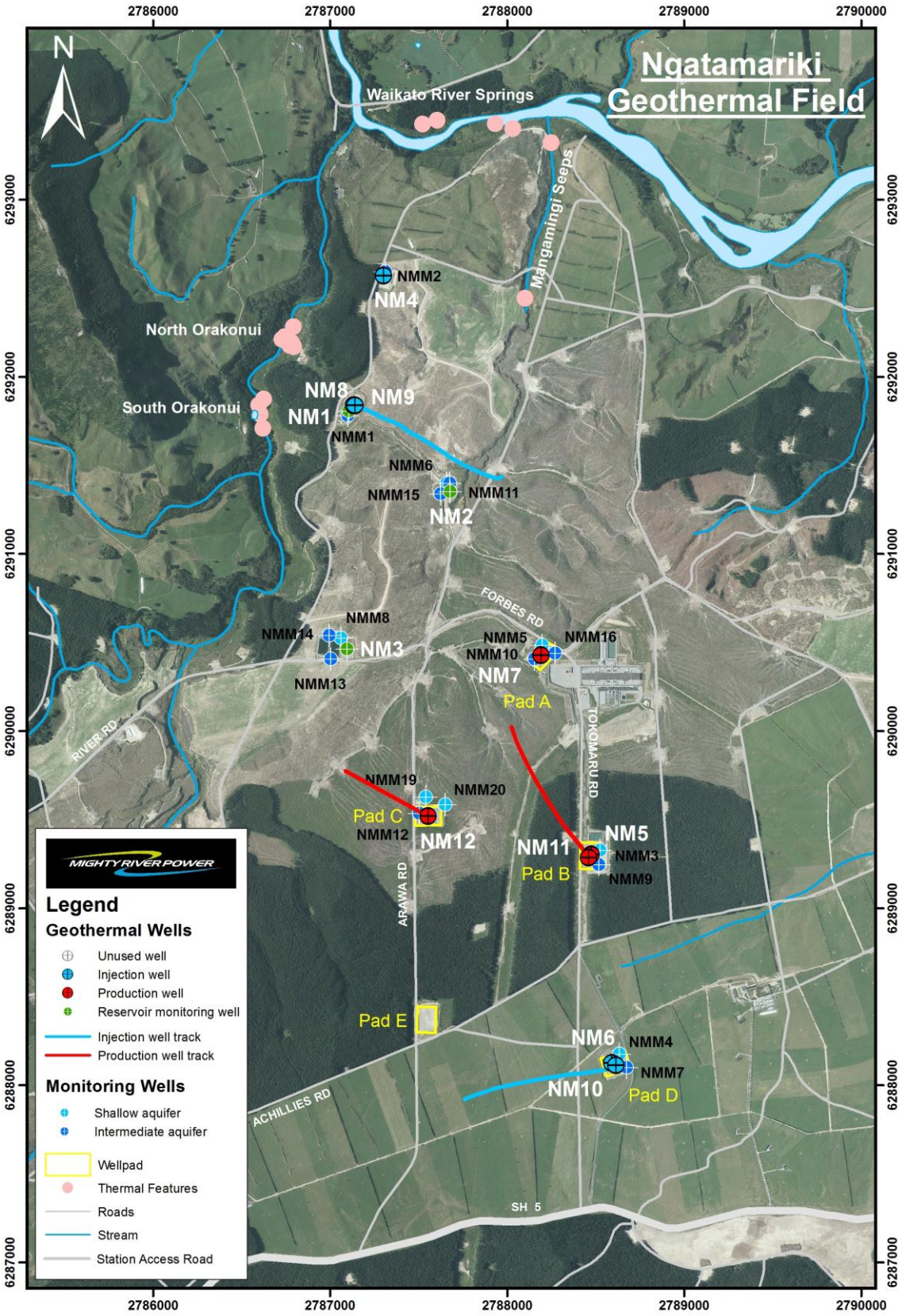

Figure 1.2 Aerial photo of the Ngatamariki geothermal field with geothermal wells and monitoring wells shown (MRP personal communication).

The Tahorakuri Formation is the unit of primary interest in this study for several reasons. Firstly the formation is the major host of the geothermal reservoir at Ngatamariki. There is also a sizable amount of core recovered from a wide range of depths within this unit. This allows observations of the physical properties with depth. It is comprised of thick sequences of sediments, lithic tuff, breccias and welded quartz-poor ignimbrite. The Tahorakuri Formation is defined as the volcaniclastic and sedimentary deposits between the Whakamaru Group Ignimbrites and the Greywacke basement. At Ngatamariki the Tahorakuri Formation comprises a thick pyroclastic sequence of tuff and ignimbrite, overlain by sediments and tuffs in the northern and central part of the field (Coutts 2013). Beneath the Tahorakuri is believed to be the Torlesse greywacke basement, however only one of the boreholes (NM6) has encountered this basement rock (Bignall 2009). In the NNW of the field a quartz-phyric tonalite volcanic intrusive has been encountered in three boreholes. The Tahorakuri Formation has been further described by Eastwood (2013) who described a large volume of samples from two boreholes within the Tahorakuri Formation. The Tahorakuri Formation has a thickness of >1 km at NGF, while at the nearby Rotokawa Geothermal Field it is considerably thinner. Figure 1.3 shows a cross section of NGF from NNW to SSE with locations of supplied cores shown. The Tahorakuri Formation forms a thick layer (0.8-1.2 km) over andesite in the south and the Tonalite intrusive in the north. Dating of the Tahorakuri Formation performed by Eastwood (2013) has found that the unit was deposited over 1.22 Ma.

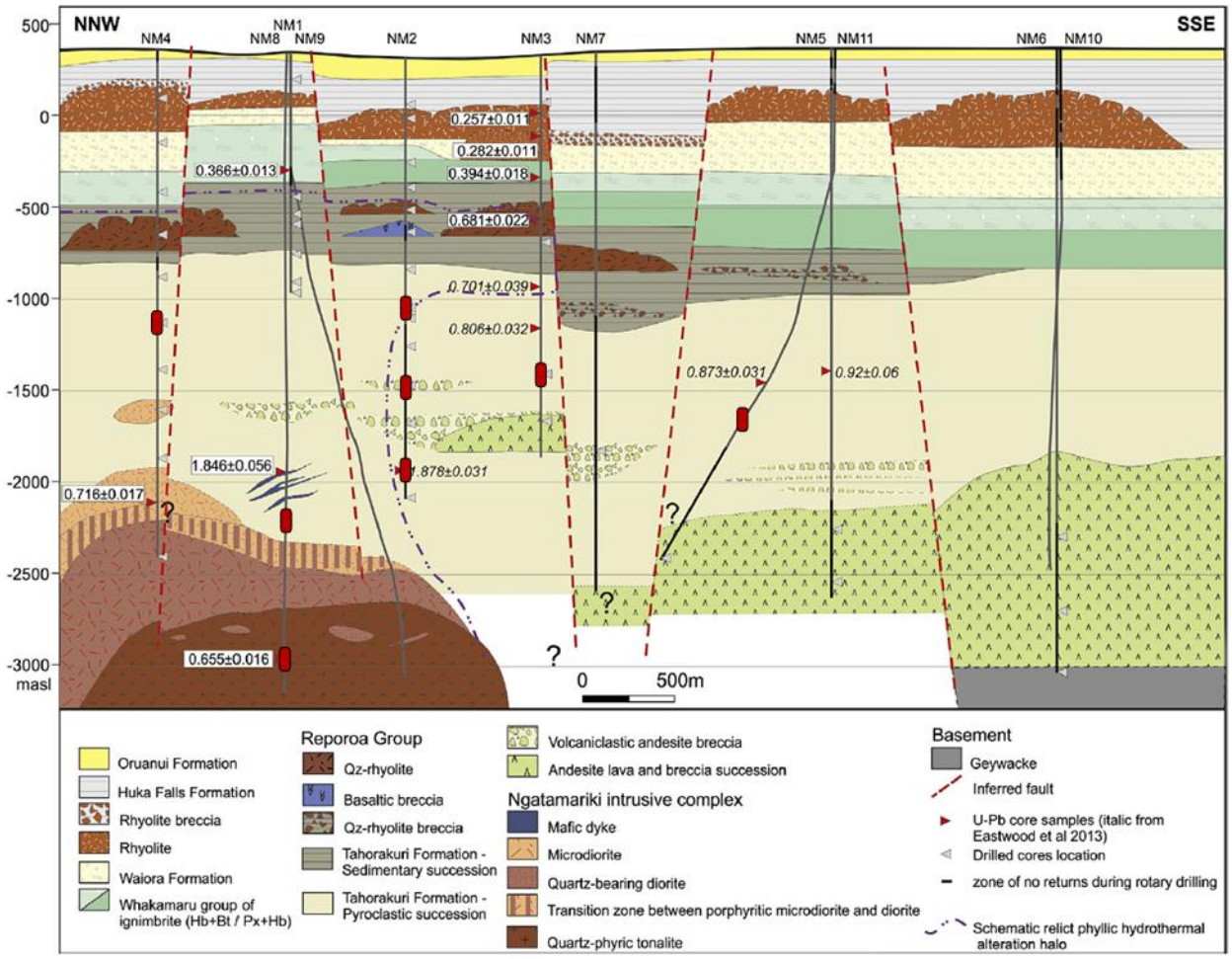

Figure 1.3 Geological Cross section of the Ngatamariki field from the NW to the SE with boreholes NM1-NM11 projected (Chambefort et al. 2014). Red rectangles represent the locations of supplied core used in this study.

1.6 Geothermal Resource

When evaluating the potential of a geothermal resource gaining an understanding of the processes is essential to fully understand the extent and character of the potential reservoir. An understating of the convection system allows for characterisation of the geothermal field to begin, one key factor is to understand the source of the fluids. Isotopic evidence can be used to distinguish between meteoric waters and deep circulation allowing a basic model to be formed (Grant 1982). Once exploration wells have been drilled both fluid and rock samples can be extracted which can further develop the conceptual model by inputting; reservoir geology, downhole geophysics,

reservoir temperature, reservoir pressure, permeability distribution, zonation within the reservoir, fluid chemistry, hydrothermal alteration and well discharges. This results in a conceptual model that can provide an idea of the geothermal resource and be used to guide development of exploitation.

The NGF is one of 23 high enthalpy geothermal systems within the TVZ. The field was first documented in 1937 and was geologically mapped in 1972 (O'Brien et al. 2011). Electrical resistivity surveys were undertaken at Ngatamariki between 1963 and 1967 as part of a wider survey of the area. This resulted in an inferred reservoir boundary of 7 km^2 based of an area of low apparent resistivity defined by the 20 Ωm resistivity contour. This was assumed to be associated with the hydrated clays deposited by circulating geothermal fluids. Further resistivity surveys have since been completed to further constrain the field and infer key geological features. Magnetic surveys completed in the area and published by Hunt and Whiteford (1979) found that the 20 Ωm contour coincided with negative magnetic anomalies which in New Zealand have been associated with the demagnetisation of the volcanic host rock by high temperature geothermal systems (Hochstein 1971). Based off a combination of electrical resistivity survey and magnetic surveys a geothermal field of 7-12 km^2 was inferred (Bignall 2009). Four exploratory wells drilled by the New Zealand Government in the 1980's discovered high temperature fluids at the site, with no further development until 2008 when three further wells were drilled. The field was further developed with the binary geothermal power plant opening in 2013.

The NGF is composed of three distinct aquifers. A deep reservoir (below 1000 mbgl) which contains the primary geothermal fluids. An intermediate aquifer (~250 – 500 mbgl) sitting directly above the reservoir within the clay cap and a third unconfined shallow aquifer (<100 mbgl). This aquifer is located in the shallow formations with its base being the top of the Huka Falls Formation. This formation forms an aquitard which separates it from the intermediate aquifer (O'Brien et al. 2011).

Within the deep reservoir, liquid and gas compositions suggest that up flow to the field is located to the west of NM3 and has an approximate temperature of 280 C° based on the Na-K-Ca geothermometer. Within the intermediate aquifer it appears there are two distinct groups of waters, meteoric recharge water that is uninfluenced by the deep geothermal reservoir and dilute geothermal fluids mixed with regional groundwater. The distinction of these two water groups is illustrated using the chemical composition of the water (O'Brien et al. 2011). Chloride was used to map the up flow from the deep aquifer to the intermediate aquifer, reflected by the hydrothermal

alteration of the reservoir rocks in this location. As of 2010 Mighty River Power were given a resource consent to extract 60,000 tons of fluid per day with ninety eight percent reinjection, with the condition that extraction does not affect the nearby protected Orakei Korako geothermal field (Boseley 2010).

2 Methodology

2.1 Sample Preparation

The samples were taken from a range of core, supplied by Mighty River Power Ltd. and Te Pumautanga o Te Arawa Trust, from the NGF. The supplied core samples had diameters of ~120 - 60 mm and lengths of ~300 - 40 mm. A drill press was used to extract 25 - 20 mm diameter cylinders from the supplied core using a diamond tipped coring bit. The cylinders were all oriented parallel to the long axis of the core samples, making them approximately vertical within the stratigraphic column. A small section of each sample was removed for thin sectioning, petrophysical analysis and investigation. The samples were then cut and ground flat using both Controls 55-C0201/b and Controls 45-D0536 core grinders. The final dimensions of the sample have a length to diameter ratio between 1:1.8 – 1:2.2 as recommended by Ulusay and Hudson (2007) for UCS testing. After coring and grinding of the samples, they were placed in an ultra-sonic cleaning bath with distilled water to clean and remove loose fractured material or clays formed during core drilling and grinding.

2.2 Porosity and Density Measurements

Two methods were used to calculate the density and porosity. The first used saturated and dry weight with calliper measurements of the sample. The second used saturated, submerged and dry weight and is commonly referred to as the Archimedes method. The Archimedes method is the recommended test for samples with an irregular geometry (Ulusay & Hudson 2007), while the samples are roughly cylindrical there are slight irregularities related to the extraction of the samples making the Archimedes the preferred method. A comparison of the results of the two methods can be seen as section 3.4 on page Results section.

The calliper method involved submerging the samples in a desiccator with distilled water under vacuum at ≈-100 kPa for 24 hours. The samples were then removed from the desiccator, the surface water removed with tissue paper and the sample weighed. Next, three measurements of diameter and three measurements of length were taken using calibrated callipers. These measurements were taken at different locations along the sample and the results averaged to yield averaged sample dimensions. The samples were then placed in the laboratory oven at 105°C for a minimum period of 24 hours to record the dry weight of the samples. The following equations (Ulusay & Hudson 2007) were used to calculate the porosity and density:

$$n = \left(\frac{100V_v}{V}\right)\% \quad (1)$$

$$\rho_d = \frac{M_s}{V} \quad (2)$$

Where

n = porosity (%)

V_v= is the pore volume calculated from the saturated and dry weights m^3

V = volume in m^3 (calculated from Vernier calliper measurements)

M_s = saturated mass (kg)

ρ_d = dry density (kg/m^3)

The Archimedes method requires the samples to be submerged in the same vacuum conditions as the calliper method. The samples are then transferred to a submerged basket in an immersion bath and weighed. After removal from the bath, the surface water is removed with tissue paper, then weighed. The samples are then placed in the laboratory oven at 105°C for a minimum period of 24 hours, then the dry weight of the samples is recorded. Equations for calculating porosity and density remain the same but the volume is calculated in a different way. The bulk volume calculation is as follows:

$$V = \frac{M_{sat} - M_{sub}}{\rho_w} \quad (3)$$

Where

M_{sat} = saturated mass (kg)

M_{sub}= submerged mass (kg)

ρ_w = density of water (kg/m^3)

This method of volume calculation is more accurate as is takes into account any variations in the shape of the sample that may be missed by the calliper method. Therefore it provides greater accuracy for both density and porosity.

2.3 Ultrasonic Wave Velocity Measurements

Axial P (pressure) and S (shear)-wave velocities were measured using a GCTS (Geotechnical Consulting and Testing Systems) Computer Aided Ultrasonic Velocity Testing System (CATS ULT–100) device. Piezoelectric transducers within the device are used to measure the arrival time of the compressional and shear waves from which the velocity can be calculated. A load of 2.7 KN (5 MPa axial stress) was applied to the samples by the Technotest KE 300 ECE compression testing machine to provide solid contact between the sample and the Piezoelectric transducers as this allows for a consistent waveform for all velocity measurements. The stress of 5 MPa was relatively low when, however there was a concern that the extensively altered nature of the rock mass might cause plastic deformation at low loads.

Ultrasonic wave velocities were performed on the samples twice; once when the samples were oven dried and again when the samples had been saturated in distilled water under a vacuum. Samples were oven dried and stored in a desiccator before testing.

One hundred and forty four waveforms were captured for both the dried and saturated samples. First, seventy two waveforms were captured, then the sample was flipped within the UCS device, the confining pressure was reapplied and the remaining waveforms captured. The values were then compared and averaged to give a representative value for the sample, this accounts for any anisotropy of wave propagation. The saturated samples were kept saturated in the desiccator until they were required for test in which the surface water was removed using tissue paper. The obtained waveform velocities were used to calculate dynamic Poisson's ratio and Young's Modulus using the following equations (Guéguen & Palciauskas 1994):

$$v = \frac{Vp^2 - 2Vs^2}{2(Vp^2 - Vs^2)} \quad (4)$$

$$E = \frac{\rho Vs^2 (3Vp^2 - 4Vs^2)}{Vp^2 - Vs^2} \quad (5)$$

Where:

v = Poisson's ratio

Vp = compressional P wave velocity (m/s)

Vs = shear S wave velocity (m/s)

E = Young's modulus (Pa)

ρ = density (kg/m^3)

2.4 Thin Section Analysis

Thin sections were prepared at the University of Canterbury sample preparation room. Twenty of the twenty one samples had thin sections prepared with sample NM11 2083.34 B too small to create a thin section. The thin sections were uncovered, vacuum fluorescent epoxy impregnated and polished, and initially evaluated using a Meiji MT9200 bi-focal polarising microscope with 4x, 10x and 40x magnification and a rotating stage. Microstructure was characterised using a Nikon Eclipse 80i epifluorescence microscope. The epifluorescent microscope uses a high pressure mercury lamp that radiates ultraviolet light, which interacts with the fluorescent epoxy resin impregnated within the sample. Areas where the resin has accumulated (vesicles, vugs, fractures, etc.), glow under the light emitted by the mercury bulb. The advantage of this method of impregnation is the fluorescent dye only accumulates in the connected pore spaces. The Nikon Eclipse 80i also has a standard microscope bulb so features can be compared in fluorescent light and plane polarised light. This enables areas that have been identified as void spaces in fluorescent light to be confirmed using plane polarised light.

2.4.1 Polarised Light Microscopy

Thin sections were analysed to assess and identify the primary and secondary mineralogy and textures within the samples. This allowed the rock type to be identified and establish the depositional environment of the sample. The internal structure along with key minerals present

were used to identify the hydrothermal alteration and post depositional stress changes. Figure 1 shows representative examples of petrographic types.

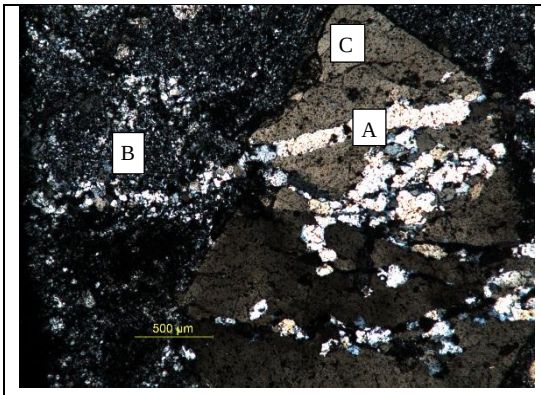

Quartz vein (A) traversing through the devitrified glass matrix (B) and a quartz crystal (C), NM8a 2525.25 mbgl

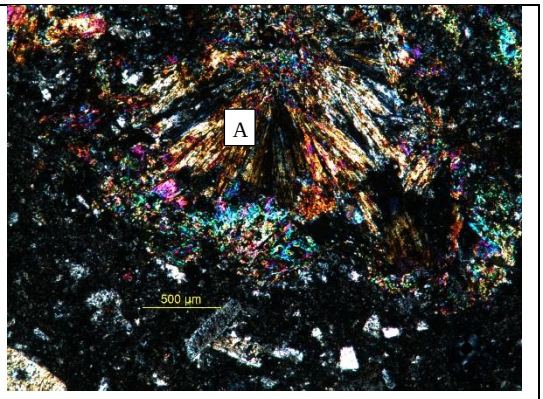

Radial epidote (A), 2083.34 mbgl, NM11

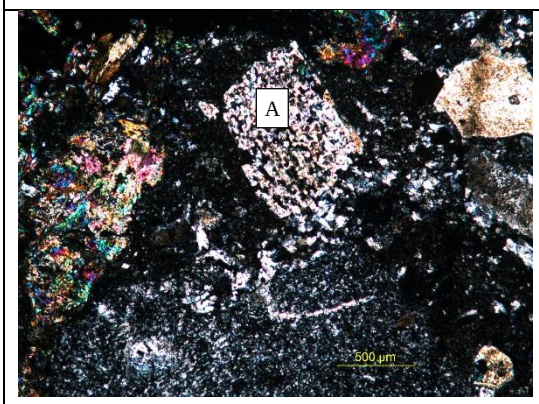

Resorbed quartz crystal (A) 2083.34 mbgl, NM11

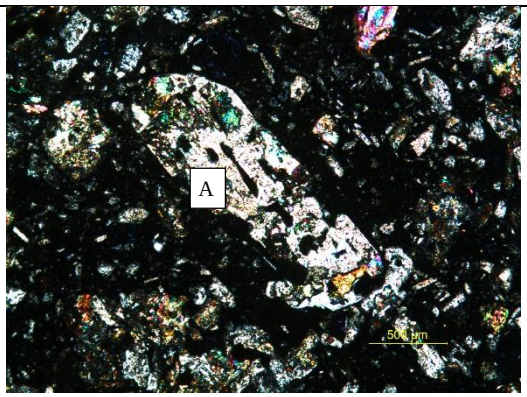

Resorbed feldspar (A) 1788 mbgl, NM2

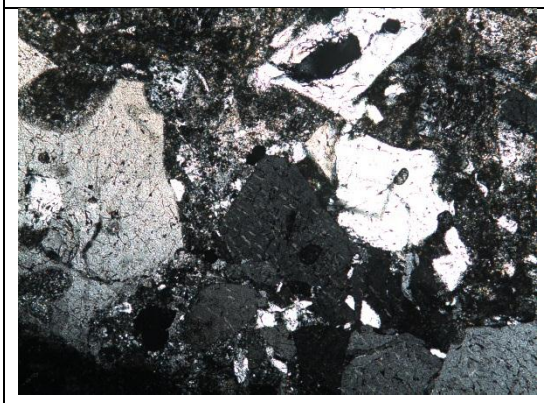

Large sub-rounded, fractured quartz, 2254 mbgl, NM2

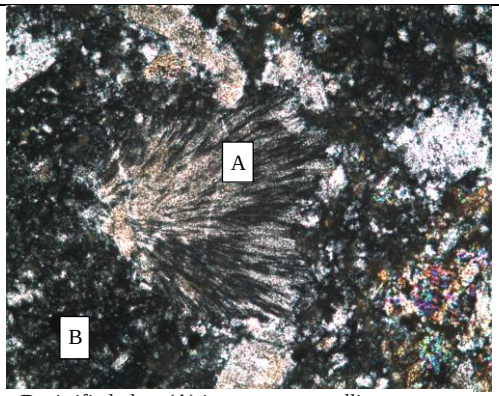

Devitrified glass (A) in a cryptocrystalline quartz feldspar matrix (B), 2087 mbgl, NM11

Figure 2.1 Photographs taken using polarised light to identify key textures and minerals

2.4.2 Fluorescent light Microscopy

Photomicrograph maps were created from each thin section for analysis of the two dimensional microstructure using fluorescent light. The computer program Autostitch was use to stitch the 16-20 individual photographs into one large image (Figure 2.2). The open source software Image J was then used to identify and isolate areas in which the fluorescent dye had aggregated, typically vesicles and microfractures. Figure 2.2 to Figure 2.4 show the process in which these areas where isolated.

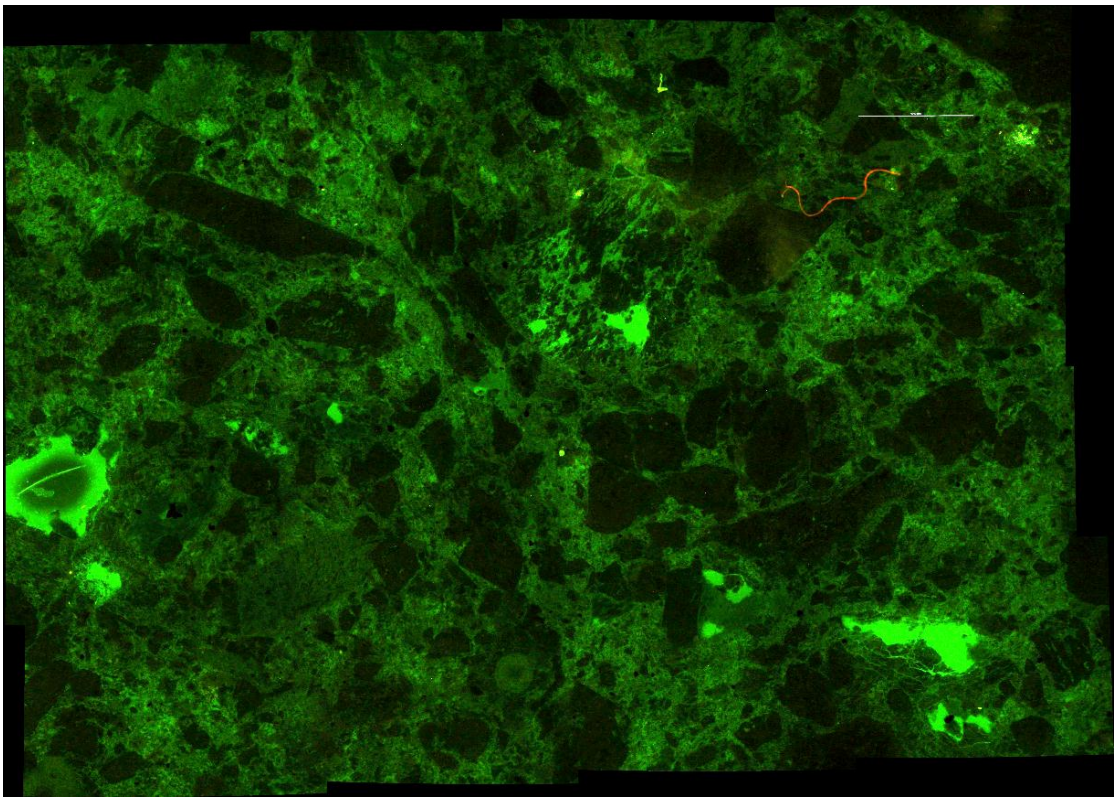

Figure 2.2 Raw image from Autostitch after colour balance adjusted in Image J. Note the scale bar in the top right shows 1.212 mm. Image is from TS3, NM11 2087.4 mbgl. The bright green areas of the image are areas where the fluorescent epoxy die has aggregated, it can be seen that there are several large vugs within the groundmass. A foreign object is also visible as an orange irregular shaped line in the top right. This is likely hair or clothing fibre that has been trapped in the epoxy resin.

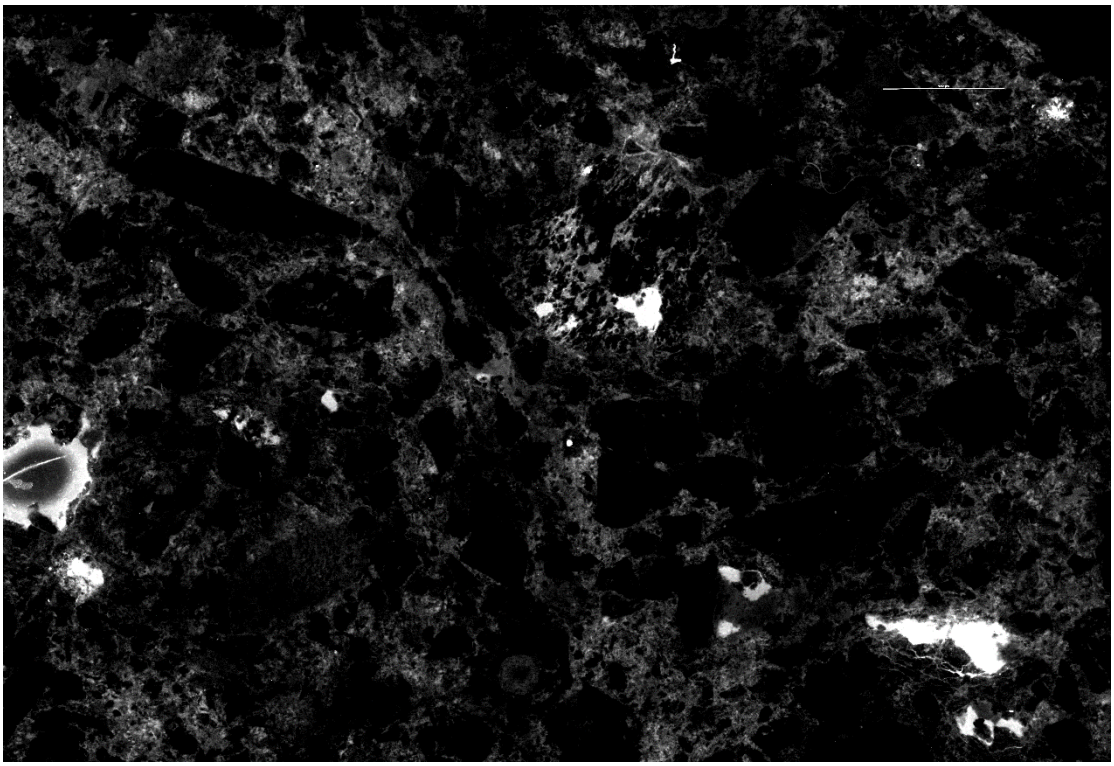

Figure 2.3 After colour thresholds are adjusted, the image is converted to a RGB (red, green, blue) stack. The red and blue images are discarded leaving a black and white image that shows the intensity of the green light captured. When this image is compared with Figure 2.2 the white areas correspond well with the bright green areas. The large vug on the left has a darker circle within its centre. This is quite common in the larger vesicles and is likely a bubble within the fluorescent resin. This dark centre can be removed before analysis. In the top right near the scale bar is an area of white. This is a mineral or foreign object that is interacting with the fluorescent light. Due to its shape and slightly different colour (Figure 2.2) it can be identified and removed before analysis. During the capturing process it is easy to switch between fluorescent and plane polarised light to identify what is and isn't pore space.

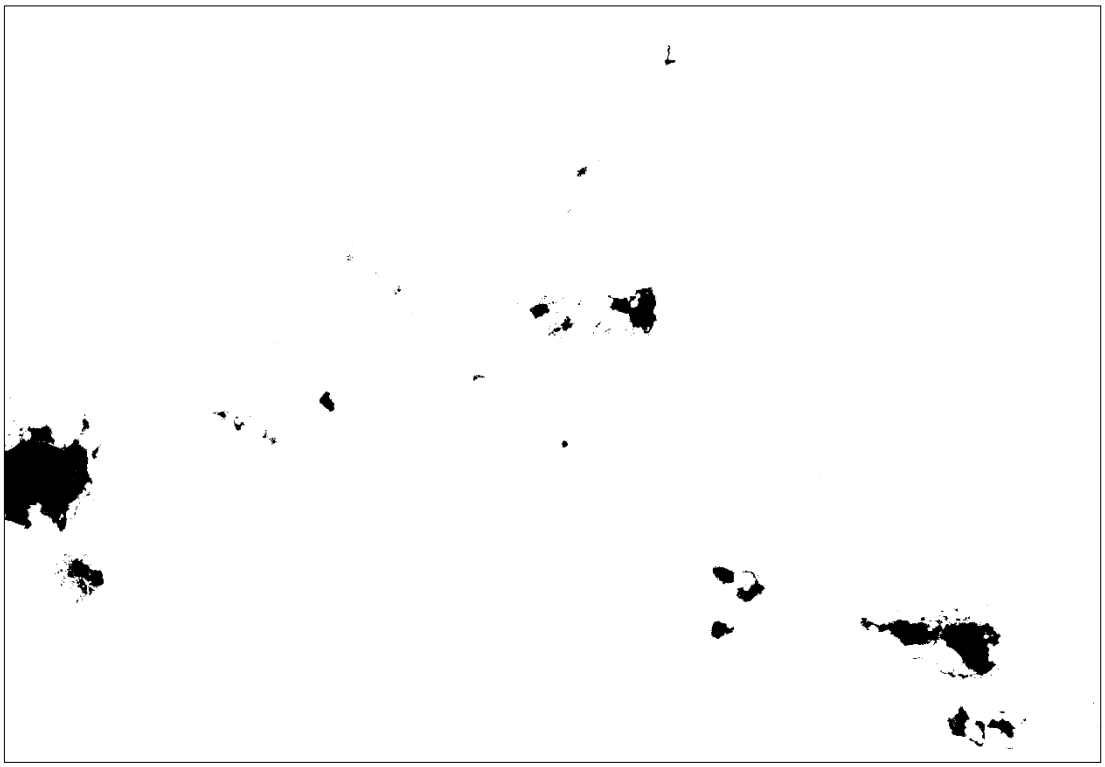

Figure 2.4 A threshold is then passed over the image where the user chooses on a sliding scale which white level is to be used as the identifier of void spaces. The threshold is set where identified voids are included but the non-void spaces that are also nearing white in colour are not included in the final image. This results in a binary image with the connected voids in black and unconnected voids and the minerals making up the rock mass in white. This is a time consuming process as considerable photo manipulation is required to get the desired image. In the bottom right of the image there is visibly less fractures surrounding the vug when compared to Figure 2.3. This is due to the white intensity in the background of the image. If the threshold was set to allow for the microfractures surrounding the vug several other falsely identified "void spaces" in the background were also identified. While there are small areas of voids that are not identified in the final image there is a high degree of confidence that all identified void spaces are true pore spaces.

The resultant image seen in Figure 2.4 has completely isolated the void spaces from the groundmass. This means quantitative analysis can be performed with confidence that all connected porosity within the thin section have been identified. Using the analytical functions in ImageJ the thin section connected porosity was calculated on all binary thin section images using equation 6:

$$Connect\ porosity\ (\%) = \left(\frac{area\ of\ black\ (pore\ space) in\ binary\ image}{total\ area\ of\ binary\ image}\right)100 \qquad (6)$$

Further analysis of the binary images was divided into two main groups depending on the type of pore spaces found in the images; microfractures or vesicles. Section 4.1.1 on page 51 discusses the effects and significance of these two pore structures in greater detail.

2.4.3 Microfracture Analysis

Microfracture surface area was measured using classical stereological techniques outlined by Underwood (1969) and further described by Wu et al. (2000) and Heap et al. (2014). Using the binary images created in ImageJ (similar to Figure 2.4) the number of cracks intersecting a grid of parallel and perpendicular lines spaced at 0.1 mm is recorded. The crack density per mm in each plane is then calculated from the known length and width of the image giving values for P‖ (cracks intercepting parallel lines per mm) and P⊥ (cracks intercepting perpendicular lines per mm). This allowed the calculation of crack surface area per unit volume using equation 7:

$$Sv = \frac{\pi}{2} P\perp + (2 - \frac{\pi}{2}) P\parallel \quad (7)$$

Where

Sv = Surface area per unit volume, mm^2/mm^3

P⊥ = crack density for intercepts perpendicular to orientation axis, mm^{-1}

P‖ = crack density for intercepts parallel to orientation axis, mm^{-1}

Anisotropy of the crack intercept distribution was also calculated using equation 8:

$$\Omega_{2,3} = \frac{P\perp - P\parallel}{P\perp} + (\frac{4}{\pi} - 1) P\parallel \quad (8)$$

Where

$\Omega_{2,3}$= Anisotropy of microfracture distribution

2.4.4 Vesicle Analysis

Pore analysis was performed in ImageJ to ascertain the aspect ratio, circularity and roundness of the pores. A minimum vesicle area of 0.0002 mm^2 was used during all pore analysis. This value was selected due to the quality of the images used. Below that value the void spaces become very pixilated and no longer provide good representation of the voids they characterise. To analyse the pores, first they must be converted into best fit ellipses to allow ImageJ to perform the quantitative analysis. These ellipses have the same area, orientation and centroid as the original selection and the same fitting algorithm is used to measure the major and minor axis lengths and angles. Henceforth all reference to the quantitative vesicle analysis will be refer to the measurements performed on the best fit ellipses. The pore parameters were automatically calculated by the ImageJ software using the equations 9 to 12:

$$aspect\ ratio = \frac{long\ axis}{short\ axis} \quad (9)$$

$$area = \pi(major\ axis)(minor\ axis) \quad (10)$$

$$circularity = 4\pi(\frac{area}{perimeter^2}) \quad (11)$$

$$Roundness = 4(\frac{area}{\pi(major\ axis)^2}) \quad (12)$$

2.5 Lithostatic Stress Model

When investigating the effects of burial diagenesis it is important to replicate the conditions from which the samples were taken during laboratory testing. This has not been possible for the mechanical properties already discussed in this chapter. Due to the PDP 200's ability to test the permeability of samples at a range of confining pressures it is possible to replicate the lithostatic pressure from where each sample was taken. To achieve this, a lithostatic model was compiled using the cross section and lithologies as defined by (Chambefort et al. 2014) and seen as Figure 1.3 on page 18. Due to the extensional nature of the TVZ, σ_1 was assumed to be vertical (Hurst et al. 2002); this allowed the true lithostatic stress to be calculated using the following equations 13:

$$\varrho_{true} = \varrho_{bulk\ litho} - \varrho_{hydro} \quad (13)$$

Where:

ϱ_{true} = true lithostatic stress

$\varrho_{bulk\ litho}$ = bulk lithostatic stress

ϱ_{hydro} = hydrostatic stress

The bulk lithostatic stress is the combined stress of each overbearing unit as applied to each sample which varies sample to sample due to differing burial depths and/or different overlying lithological units. The hydrostatic stress is the total stress applied by the groundwater. The hydrostatic stress is equal in all directions and results in a stress that acts against the lithostatic stress. This stress is experienced at pore and fracture boundaries within the rock mass. Due to limited published data on the hydrology of the field, a very simple hydrostatic model was used that assumed that a connected water column throughout the field of cold water (to maintain a constant density for calculation). To calculate the stresses applied by the overlying intact rock and the groundwater equation 14 used:

$$\varrho = \rho g h \qquad (14)$$

Where:

ϱ = effective stress

ρ = rock mass density (kg/m^3)

g = gravitational force (m/s)

h = height or thickness of layer (m)

To ascertain the rock mass density as required by equation 14 the intact rock densities of each lithological unit were first given a dry density. When possible these densities were taken from the laboratory testing performed in this thesis. When that was not possible, a literature search was performed to determine the densities of the same or similar units as tested in other projects. In some situations no published data could be found on certain lithological units and averaged data of similar rock type from text books was used. This method of density allocation was used as the lithologies at Ngatamariki have a complex alteration history that has likely changed the densities of the lithologies from the expected range found in text books. Table 2.1 shows the density data used to develop a lithostatic model for Ngatamariki. It should be noted that while all attempts were made to provide accurate data, the values provided may vary from that of the in-situ formation.

The stresses from each lithological unit are summed to give the bulk stress for each sample. To calculate the true lithostatic stress the hydrostatic stress must be accounted for.. This method of calculation uses equation 14 where density is that of water = 1000 kg/m^3.

Formation	Source	Intact Rock Density (kg/m^3)
Oruanui (tephra)[1]	(Palmer 1982)	1450
Huka Falls (Volcaniclastic Sandstone)[2]	(Read et al. 2001)	1033
Rhyolite lava[2]	(Wyering et al. 2014)	1819
Waiora Formation (tuff)[3]	(Vutukuri & Lama 1940)	2140
Whakamaru group ignimbrite[3]	(Vutukuri & Lama 1940)	2045
Tahorakuri sedimentary succession (lacustrine sediments and tuff)[2]	(Wyering et al. 2014)	1960
Quartz – rhyolite[2]	(Wyering et al. 2014)	2325
Tahorakuri pyroclastic succession (Volcaniclastic)	This thesis	2360
Volcaniclastic andesite breccia	This thesis	2470
Volcaniclastic andesite breccia	This thesis	2470
Porphyritic microdiorite – diorite[3]	(Vutukuri & Lama 1940)	2729
Quartz bearing diorite[3]	(Vutukuri & Lama 1940)	2729
Tonalite	This thesis	2510

Table 2.1 Density data for the lithological units found at Ngatamariki. 1, Data used was from a source outside of the TVZ but with similar descriptions. 2, Data used from a source from the same/similar lithological unit but measured at a location that is not Ngatamariki. 3, Data used from averages supplied by textbooks.

The thickness of the individual formations was measured for each well using the cross section provided by Chambefort et al. (2014). This created a model that takes into account formation thickness variability across the field. Table 2.2 below shows the variations in the unit thicknesses across the field. Several formations are only present in two or three of the wells and there is a large variation in the thicknesses of the formations between the wells.

	NM2	NM3	NM4	NM8a	NM11
Formation	**Thickness (m)**				
Oruanui	115	110	45	52	55
Huka falls	155	155	150	170	175
Rhyolite	165	305	240	75	160
Waiora Formation	35	-	215	85	185
Whakamaru group ignimbrite	200	105	180	325	570
Tahorakuri sedimentary succession	365	325	120	360	250
Quartz - rhyolite	70	180	180	-	-
Tahorakuri pyroclastic succession	1075	740	980	1655	1200
Volcaniclastic andesite breccia	190	-	-	105	-
Porphyritic microdiorite - diorite	-	-	-	145	-
Quartz bearing diorite	-	-		215	-
Tonalite	-	-	-	455	-

Table 2.2 Formation thicknesses across tested wells at Ngatamariki

Using the parameters defined in Table 2.1 and Table 2.2 both the bulk lithostatic and hydrostatic stresses for each formation were calculated. Table 2.3 shows the stresses applied by each formation at each well.

Bulk stress applied by lithostatic pressure and hydrostatic pressure (MPa)										
	NM2		**NM3**		**NM4**		**NM8a**		**NM11**	
Formation	Litho.	Hydro.	Litho.	Hydro.	Litho.	Hydro.	Litho.	Hydro.	Litho.	Hydro.
Oruanui	1.6	1.1	1.6	1.1	0.64	0.44	0.74	0.51	0.78	0.54
Huka falls	1.6	1.5	1.6	1.5	1.5	1.5	1.7	1.7	1.8	1.7
Rhyolite	2.9	1.6	5.4	3.0	4.3	2.4	1.3	0.74	2.9	1.6
Waiora Formation	0.73	0.34			4.5	2.1	1.8	0.83	3.9	0.18
Whakamaru group ignimbrite	4.0	2.0	2.1	1.0	3.6	1.8	6.5	3.2	1.1	5.6
Tahorakuri sedimentary succession	7.0	3.6	6.2	3.2	2.3	1.2	6.9	3.5	4.8	2.5
Quartz - rhyolite	1.6	6.9	4.1	1.8	4.1	1.8				
Tahorakuri pyroclastic succession	25	11	17	7.3	23	9.6	38	16	28	12
Volcaniclastic andesite breccia	1.3	0.54					2.5	1.0		
Volcaniclastic andesite breccia	3.3	1.3								
Porphyritic microdiorite - diorite							3.9	1.4		
Quartz bearing diorite							5.8	2.1		
Tonalite							11	4.5		

Table 2.3 Bulk lithostatic and hydrostatic stress (MPa) applied by each formation at Ngatamariki

Table 2.4 shows the tested samples and the corresponding effective lithostatic stress. Permeability testing of all samples was performed in 10 MPa steps. The calculated lithostatic stress was compared to the tested confining pressures and rounded to the nearest value. The permeability value of this confining pressure is then defined as the in-situ matrix permeability for that particular sample.

Borehole and depth (mbgl)	**Calculated Lithostatic Stress(MPa)**	**Closest tested confining pressure (MPa)**	**Associated permeability value (m^2)**
NM2 1788 A	17.79	15	2.70E-17
NM2 1354.2 A	12.00	15	4.94E-17
NM2 1354.2 B	12.00	15	2.29E-17
NM2 1354.4 A	12.00	15	2.04E-17
NM2 2254.7	24.09	25	1.76E-18
NM3 1743 A	16.98	15	8.62E-19
NM3 1743 C	16.98	15	8.62E-19
NM4 1477.2 A	14.53	15	6.76E-19
NM8a 2525.5 C	28.02	25	5.80E-18
NM8a 3280 C	34.34	35	3.63E-19
NM8a 3284.7 C	34.62	35	8.74E-19
NM11 2083 A	21.03	25	1.60E-16
NM11 2083 B	21.03	25	1.55E-16
NM11 2083 C	21.03	25	1.49E-16
NM11 2083.34 A	21.03	25	2.43E-16
NM11 2083.34 B	21.03	25	2.26E-16
NM11 2087.4 A	21.09	25	1.29E-16
NM11 2087.4 B	21.09	25	1.92E-16
NM11 2087.4 C	21.09	25	1.85E-16
NM11 2087.4 D	21.09	25	1.48E-16

Table 2.4 Lithostatic stress (confining pressure) for each sample and the corresponding permeability test values

2.6 Permeability Measurements

Permeability measurements were made at the University of Canterbury Soils Laboratory using a Core Lab PDP 2000 Pulse decay permeameter. The permeameter along with all the related parts of the operation are enclosed within a glass cabinet that is temperature controlled via two electronically controlled heaters. The first heater provide a constant temperature for all componentry of the test, therefore making the testing repeatable and consistent. The second heater provides heat to the testing cylinder. This allows testing of the samples over a range of temperature which can simulate in-situ conditions. Figure 2.5 shows a basic schematic diagram of the permeameter used for testing. One heater maintains the ambient air temperature while the other is applied directly onto the testing cell. The sample is placed inside a Viton tube inside the testing cell. A confining pressure is then applied via hydraulic fluid controlled by a manual hydraulic pump. Pressurised nitrogen from the gas cylinder is applied to the sample and left to "soak" for an appropriate amount of time for the sample to equalise to the test pressure and temperature. The gas valves are then shut off and the nitrogen gas is bled from the downstream side of the core holder using the needle value until the desired pressure differential is achieved. The needle value is then closed and the pressure differential across the sample is monitored as the nitrogen gas equalises by traveling through the sample. The gas differential across the sample decays in logarithmic fashion that is recorded by the PDP 200's software.

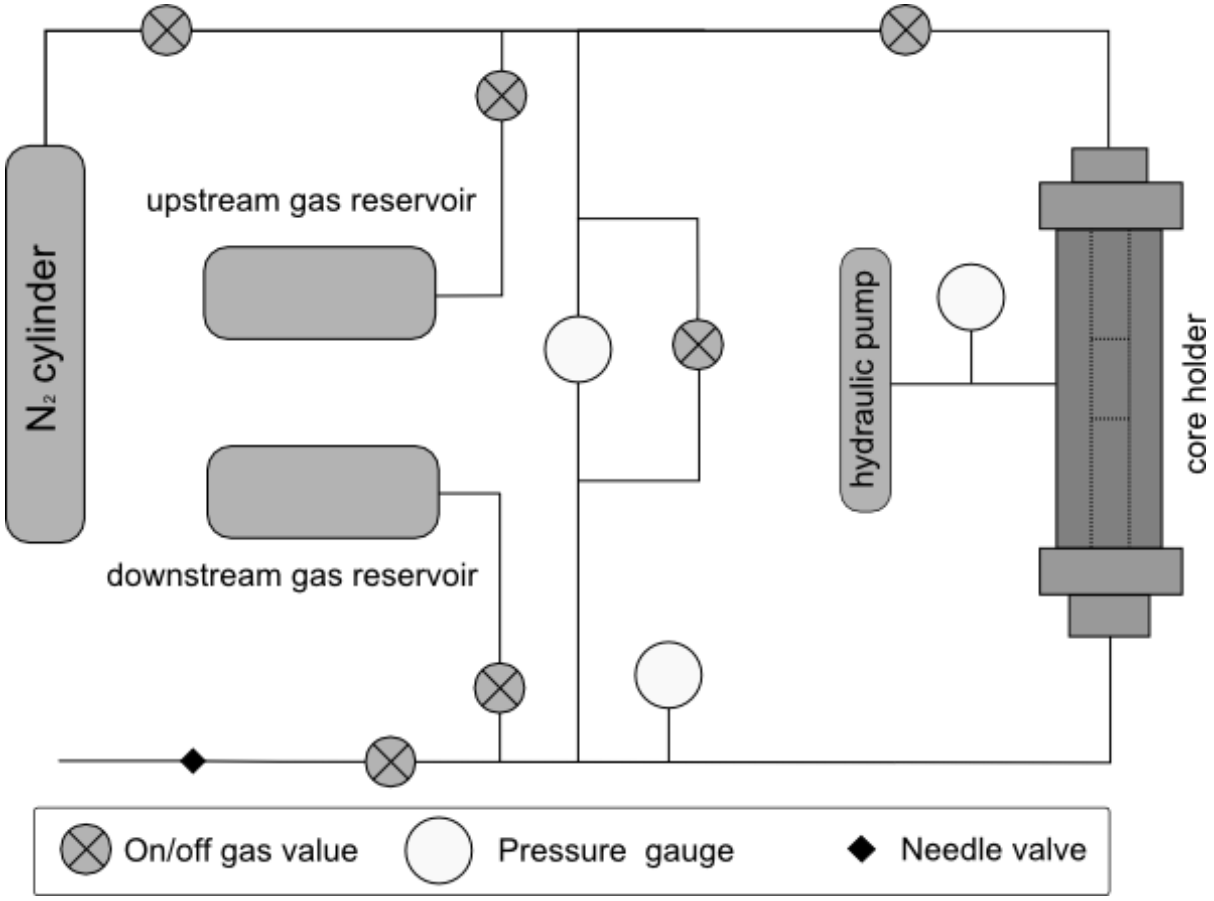

Figure 2.5 Schematic of the pulse decay permeameter used for testing

A testing procedure was followed for each of the samples to achieve an accurate and repeatable result. The test started at the lowest possible confining pressure (5 MPa) where three to five apparent gas permeability tests would be measured. The confining pressure would then be increased by 10MPa and the sample would be left to "soak" for the appropriate amount of time before testing the permeability in the method listed above. This is repeated until the confining pressure reaches 65 MPa.

2.6.1 Permeability Calculation

The calculation of gas permeability is completed using a modified version of Darcy's law (Brace et al. 1968) and is as follow:

$$k_{gas} = \left(\frac{2\eta L}{A}\right)\left(\frac{V_{up}}{P_{up}^2 - P_{down}^2}\right)\left(\frac{\Delta P_{up}}{\Delta t}\right) \quad (15)$$

Where:

k_{gas} = gas permeability

η = viscosity of the pore fluid

L = length of the sample

A = cross sectional area of the sample

V_{up} = volume of upstream pore pressure circuit

P_{up} = upstream pore pressure

P_{down} = downstream pore pressure

t = time

The equation above is used by the PDP 200's software to calculate the gas permeability of the differential pressure decay curve and results in gas permeability measurements. To determine the true permeability a Klinkenberg correction is required (Klinkenberg 1941). This correction accounts for gas slippage within the sample and requires the gas permeability test to be performed at several different pore pressures.

$$k_{true} = k_{gas}\left(1 + \frac{b}{P_{mean}}\right) \quad (16)$$

Where:

k_{true} = True permeability

b = Klinkenberg slip factor

P_{mean}= Mean pore fluid pressure

This results in a series of gas permeability tests being run at a constant confining pressure while varying the pore pressure. Figure 2.6 shows four data points on the graph represent four tests completed at different pore pressures. The data shows a decrease in gas permeability with a decrease in 1/P-mean. The true permeability can be seen as the y-axis value where the trend line intercepts the zero point on the x-axis. Therefore in the example below the true permeability is $2.048e^{-16}$ m^2 as can be seen in the linear regression equation (Figure 2.6). This method for calculating the true permeability was completed on each sample at each confining pressure.

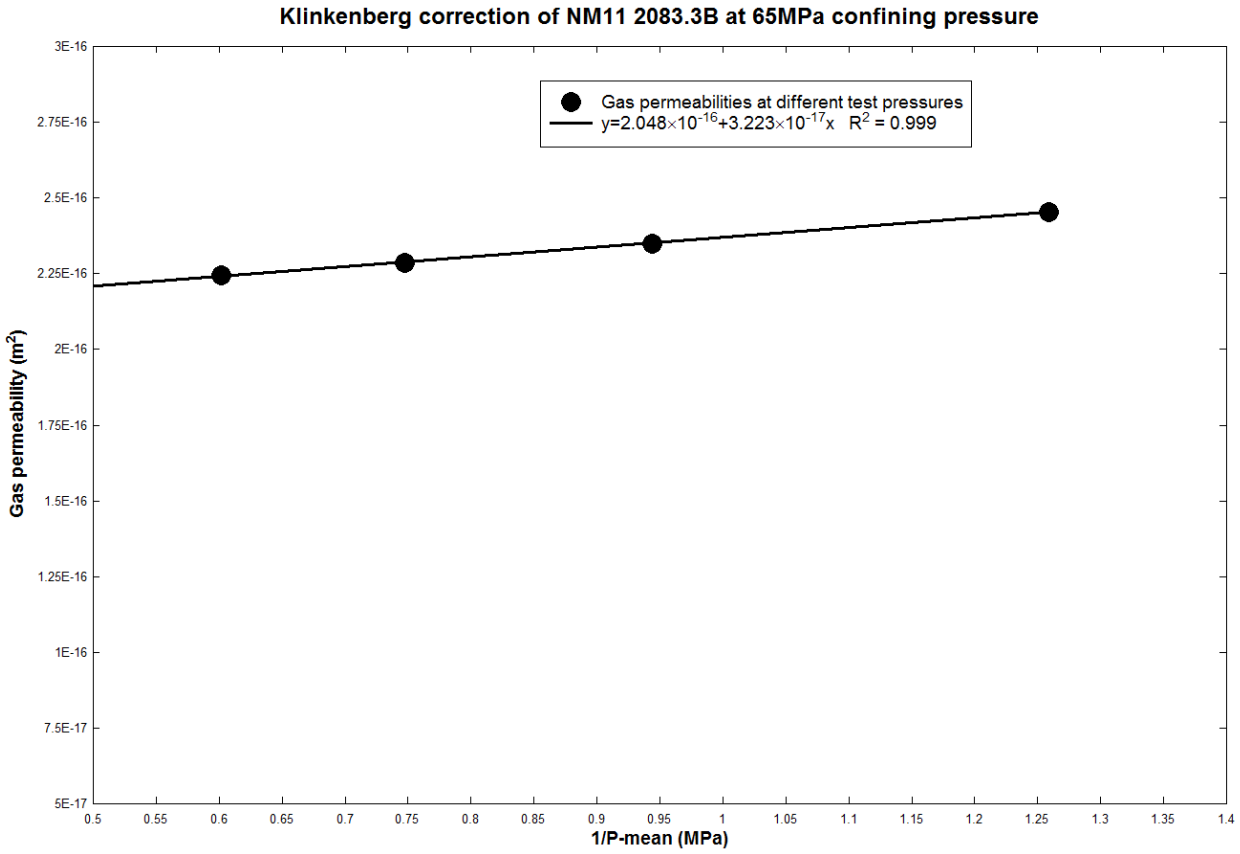

Figure 2.6 Example of Klinkenberg correction on gas permeability results

3 Results

3.1 Samples

Twenty cores were taken from the provided drill core. Table 3.1 shows the wells and depths from which samples were taken along with the associated thin section number and formation name.

Sample ID	Formation name	Thin section	Well	Depth (mbgl)
NM11 2087.4 A	Tahorakuri Formation	TS8	NM11	2087.40m
NM11 2087.4 B	Tahorakuri Formation	TS11	NM11	2087.40m
NM11 2087.4 C	Tahorakuri Formation	TS3	NM11	2087.40m
NM11 2087.4 D	Tahorakuri Formation	TS7	NM11	2087.40m
NM11 2083.34 A	Tahorakuri Formation	TS6	NM11	2083.34m
NM11 2083.34 B	Tahorakuri Formation	-	NM11	2083.34m
NM2 1788 A	Tahorakuri Formation	TS9	NM2	1788.00m
NM2 2254.7 A	Tahorakuri Formation	TS4	NM2	2254.70m
NM8a 2525.5 B	Tahorakuri Formation	TS2	NM8a	2525.50m
NM8a 2525.5 C	Tahorakuri Formation	TS12	NM8a	2525.50m
NM11 2083 A	Tahorakuri Formation	TS10	NM11	2083.00m
NM11 2083 B	Tahorakuri Formation	TS1	NM11	2083.00m
NM11 2083 C	Tahorakuri Formation	TS5	NM11	2083.00m
NM4 1477.2 A	Tahorakuri Formation	TS13	NM4	1477.20m
NM8a 3284.7 C	Ngatamariki Intrusive Complex	TS14	NM8a	3284.70m
NM8a 3280 C	Ngatamariki Intrusive Complex	TS15	NM8a	3280.00m
NM2 1354.4 A	Tahorakuri Formation	TS16	NM2	1354.40m
NM2 1354.2 A	Tahorakuri Formation	TS17	NM2	1354.40m
NM2 1354.2 B	Tahorakuri Formation	TS18	NM2	1354.04m
NM3 1743 A	Tahorakuri Formation	TS19	NM3	1743.00m
NM3 1743 C	Tahorakuri Formation	TS20	NM3	1743.00m

Table 3.1 Sample cores and their associated sample ID, depth, formation name and well number.

3.2 Lithological Units

All samples were analysed from both hand specimens and thin sections to classify them into broad lithological units based off primary and secondary textures, and mineral composition. This has resulted in four different lithologies.

3.2.1 Volcaniclastic Lithic Tuff (Tahorakuri Formation)

Hand samples appeared greeny grey with white grey and green phenocrysts, visible pumice lithics were also visible. Thin sections showed large quartz and feldspar crystals (~1 – 3 mm), sub-rounded to rounded. The groundmass consists of a devitrified glass matrix of small interlocking quartz and feldspar crystals which forms a crypto crystalline matrix. Secondary mineralisation and recrystallization is common with micro-spherulites, radial epidote and sieve textures within plagioclase crystals. These features indicate alteration and the accompanying recrystallization has occurred post deposition. In TS6 a large piece of devitrified glass has been re-crystalized. Plagioclase crystals show partial dissolution with secondary epidote recrystallized within the plagioclase crystals. Epidote veins have formed within some of the samples. Dark blue areas seen in plane polarized and cross polarized light are likely clay minerals.

3.2.2 Primary Tuff (Tahorakuri Formation)

Hand samples appeared light grey with visible lithic fragments (<2mm) dark grey to light grey. Visible pore space was observed in test cylinders. Thin sections showed crystals (~70%) of angular plagioclase and quartz (~1 - ~3 mm) are highly altered with significant resorption within the plagioclase crystals. Groundmass consists of a crypto-crystalline quartz/plagioclase matrix. Large mafic minerals like chlorite and epidote suggest post deposition alteration.

3.2.3 Welded Ignimbrite (Tahorakuri Formation)

Hand samples displayed light grey to greeny grey groundmass with lithic fragments (<2mm). Thin sections showed large (≥2 mm) angular to sub angular interlocking quartz crystals throughout the thin section suggest a volcaniclastic nature to the large phenocrysts. The majority of the sample consists of an altered groundmass with sparse lithic fragments. The groundmass consists of a crypto-crystalline quartz matrix, this suggest the samples are probably ignimbrite. Quartz veining is visible in hand samples and thin sections. The quartz veins along with radial epidote suggest significant alteration and recrystallization. Plagioclase crystals have been altered with some showing resorption. Displacement along fractures within quartz crystals show compression since emplacement. Hand sample appears relatively hard and dense with a creamy white colour.

3.2.4 Tonalite (Ngatamariki Intrusive Complex)

Hand samples showed a light grey matrix speckled black and white. Test cylinders showed no fractures or voids. Thin sections showed large quartz (~40%) and feldspar (~60%) phenocrysts (≥5 mm) are sub rounded to rounded, highly fractured with evidence of resorption. Plagioclase phenocrysts appear angular, and highly altered. Strongly porphyritic (glomeroporphyrictic texture) with an inter-grown quartz/feldspar matrix. Opaques are clustered around chlorite crystals.

3.3 Thin Section Analysis

Thin sections were broken down into two distinct groups. Figure 3.1 shows a thin section which consists solely of "vesicular" pore space with few/no visible fracture. In this type of thin section the following quantitative analysis was performed; vesicle area, circularity, aspect ratio, thin section porosity and roundness. Figure 3.2 shows a thin section in which the pore space is solely microfractures. In this type of thin section the following quantitative analysis was performed; crack density (from which crack area per unit volume and anisotropy can be calculated). Each method provides relevant and comprehensive information on the particular void type that contributes to a better understanding of the microstructure.

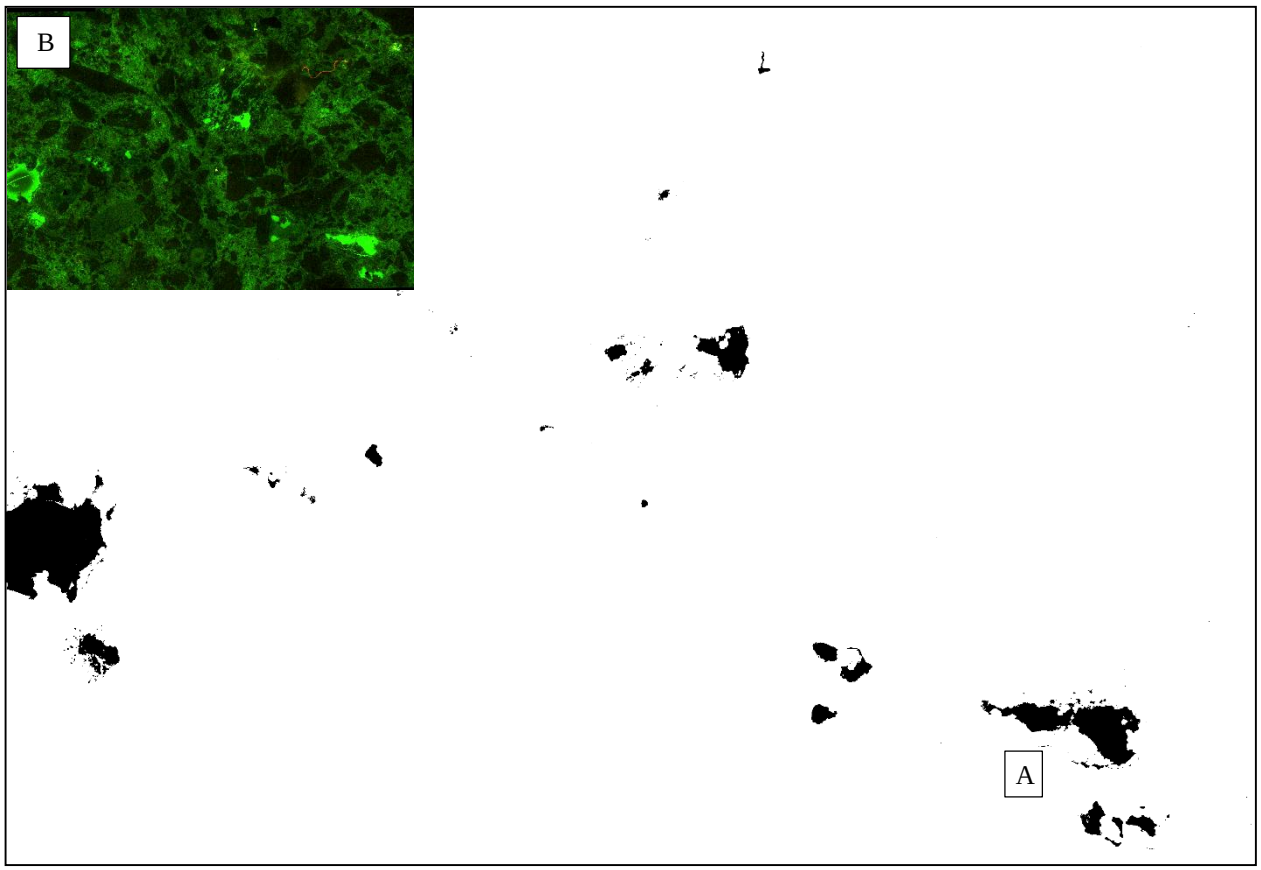

Figure 3.1 Vesicle dominated thin section with only one minor fracture visible, likely a result of the lithostatic stress applied on the vesicle (A), original figure seen as (B), TS3 (image dimensions 11x7.6mm)

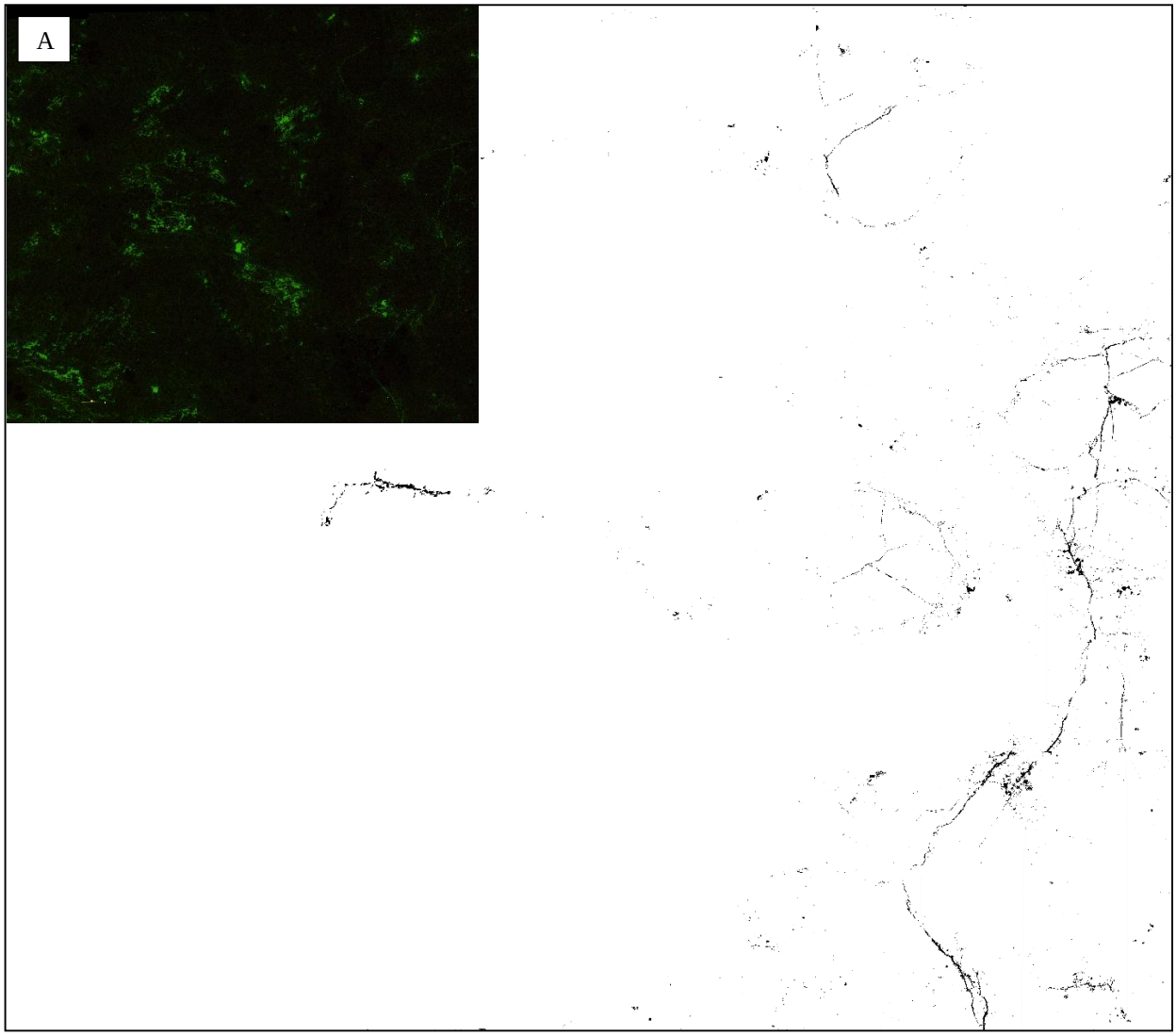

Figure 3.2 Thin section with fractures, no visible pores, TS14, original image (A) (image dimensions 10x8.8mm)

For the samples that were fracture dominated the following analysis was performed: Crack density in both parallel and perpendicular orientations, crack area per unit volume, anisotropy and thin section porosity. Table 3.2 shows the results of this testing.

Sample #	Crack density per mm^{-1} parallel to orientation axis (P∥)	Crack density per mm^{-1} perpendicular to orientation axis (P⊥)	Crack area per unit volume mm^2/mm^3(Sv)	Anisotropy ($\Omega_{2,3}$)	porosity %	Thin section porosity (%)
NM8a 2525.5 B	2.66	0.77	4.51	0.66	2.5	0.015
NM4 1477.2 A	4.67	2.00	8.19	0.51	2.9	0.064
NM8a 3284.7 C	16.59	13.30	31.77	0.16	4.0	0.296
NM8a 3280 C	10.74	25.94	28.00	0.85	3.1	1.409
NM2 1354.2 B	10.24	9.06	19.97	0.09	18.6	0.136
NM3 1743 A	4.67	4.64	9.32	0.00	6.0	0.055
NM3 1743 C	1.10	1.29	2.28	0.13	6.3	0.02

Table 3.2 Quantitative analysis of microfractures in samples from Ngatamariki

For thin sections that were dominated by vesicles, different analytical methods were used to ascertain the following properties: vesicle porosity, average vug area, maximum vug area, average circularity, average aspect ratio, maximum aspect ratio, average roundness. Table 3.3 results of quantitative analysis on thin sections that contained vug pore space shows the results of this analysis.

Sample #	NM11 2083 B	NM11 2087.4 C	NM2 2254.7 A	NM11 2083 C	NM11 2083.34 A	NM11 2087.4 D	NM11 2087.4 A	NM11 2083 A	NM11 2087.4 B	NM8a 2525.5 C
Thin section #	**TS1**	**TS3**	**TS4**	**TS5**	**TS6**	**TS7**	**TS8**	**TS10**	**TS11**	**TS12**
Vug porosity %	1.2	1.6	9.5	3.1	0.1	0.4	4.4	1.6	1.5	2.4
average area of vug (mm^{-2})	0.001315	0.002158	0.029259	0.002118	0.001284	0.000117	0.004042	0.000516	0.001168	0.001168
maximum area of vug (mm^{-2})	0.032008	0.061561	0.612151	0.069097	0.004424	0.000428	0.334661	0.011978	0.093196	0.093196
Average circularity	0.41	0.46	0.32	0.34	0.47	0.37	0.33	0.37	0.37	0.39
Average aspect ratio	1.99	2.05	2.10	2.02	1.73	1.89	2.12	2.45	2.45	2.32
Maximum aspect ratio	3.94	6.96	3.78	5.53	2.32	3.24	7.35	7.89	7.89	9.78
Average roundness	0.56	0.57	0.53	0.56	0.63	0.60	0.55	0.49	0.49	0.51

Table 3.3 results of quantitative analysis on thin sections that contained vug pore space

3.4 Dry Density

Densities of all samples was determined using two methods, the Archimedes method and the Calliper method. Table 3.4 shows the tested densities. The difference between test methods can be observed to be very low (less than 3%). The observed variations are likely due to human error during the testing or slight variations in diameter along the cylinder as this would not be accounted for in the Calliper method. Overall both methods appear to give accurate measurements of dry density with minimal testing errors.

Sample ID	Dry Density (kg/m^3) Calliper method	Dry Density (kg/m^3) Archimedes method	Difference between methods (kg/m^3)
NM11 2087.4 A	2350	2350	0
NM11 2087.4 B	2310	2290	-20
NM11 2087.4 C	2320	2300	-20
NM11 2087.4 D	2340	2320	-20
NM11 2083.34 A	2300	2240	-60
NM11 2083.34 B	2280	2270	-10
NM2 1788 A	2470	2470	0
NM2 2254.7 A	2570	2540	-30
NM8a 2525.5 B	2600	2620	+20
NM8a 2525.5 C	2580	2580	0
NM11 2083 A	2290	2280	-10
NM11 2083 B	2270	2260	-10
NM11 2083 C	2290	2280	-10
NM4 1477.2 A	2670	2670	0
NM8a 3284.7 C	2490	2500	+10
NM8a 3280 C	2510	2520	+10
NM2 1354.4 A	2160	2170	+10
NM2 1354.2 A	2070	2080	+10
NM2 1354.2 B	2100	2120	+20
NM3 1743 A	2540	2550	+10
NM3 1743 C	2510	2520	+10

Table 3.4 Dry Density results from Calliper and Archimedes method

3.5 Porosity

Porosity of samples was determined using three methods; the Archimedes methods, Calliper method and two dimensional thin section porosity. Table 3.5 shows the tested densities for the first two methods. The difference between test methods can be observed to be very low (less than 2%). The samples that have the greatest difference between the test methods were the volcanoclastic samples. This lithology has high porosity that consists primarily of vesicles. Overall both methods appear to give relatively accurate measurements of porosity with minimal testing errors especially in the low porosity samples.

Sample ID	Porosity (%) Calliper Method	Porosity (%) Archimedes method	Difference between methods (%)
NM11 2087.4 A	12.9	12.9	0.0
NM11 2087.4 B	14.5	14.4	-0.1
NM11 2087.4 C	14.2	14.1	-0.1
NM11 2087.4 D	13.5	13.4	-0.1
NM11 2083.34 A	14.4	14.0	-0.4
NM11 2083.34 B	14.9	14.9	0.0
NM2 1788 A	10.0	10.0	0.0
NM2 2254.7 A	4.9	4.9	0.0
NM8a 2525.5 B	2.5	2.5	0.0
NM8a 2525.5 C	3.3	3.3	0.0
NM11 2083 A	14.4	14.3	-0.1
NM11 2083 B	15.4	15.3	-0.1
NM11 2083 C	14.8	14.7	-0.1
NM4 1477.2 A	2.9	2.9	0.0
NM8a 3284.7 C	4.0	4.0	0.0
NM8a 3280 C	3.1	3.1	0.0
NM2 1354.4 A	19.2	19.3	+0.1
NM2 1354.2 A	20.1	20.3	+0.2
NM2 1354.2 B	18.4	18.6	+0.2
NM3 1743 A	5.9	6.0	+0.1
NM3 1743 C	6.2	6.3	+0.1

Table 3.5 Porosity using Calliper and Archimedes method

Table 3.6 shows the results of the thin section porosity measurements. This method calculates the porosity from a "snapshot" of the thin section. It is a two dimensional "cross sectional" slice of a sample. When graphically compared to the Archimedes method no clear correlation is observed however a general trend of increased thin section porosity with increase Archimedes porosity is observed. (Figure 3.3). This trend has many large variations. The study by (Heap et al. 2014) found a relatively good correlation between Archimedes porosity and thin section porosity. The significance of this will be discussed in section 4.1.4 of the discussion.

Sample ID	Thin section porosity (%)
NM11 2087.4 A	4.4
NM11 2087.4 B	1.5
NM11 2087.4 C	1.6
NM11 2087.4 D	0.37
NM11 2083.34 A	0.14
NM2 2254.7 A	9.5
NM8a 2525.5 B	0.02
NM8a 2525.5 C	2.4
NM8a 3284.1 A	1.6
NM8a 3284.1 B	1.2
NM8a 3284.1 C	3.1
NM4 1477.2 A	0.06
NM8a 3284.7 C	0.30
NM8a 3280 C	1.4
NM2 1354.2 B	0.14
NM3 1743 A	0.06
NM3 1743 C	0.02

Table 3.6 Thin section porosity, measured using binary fluorescent light photomicrograph maps

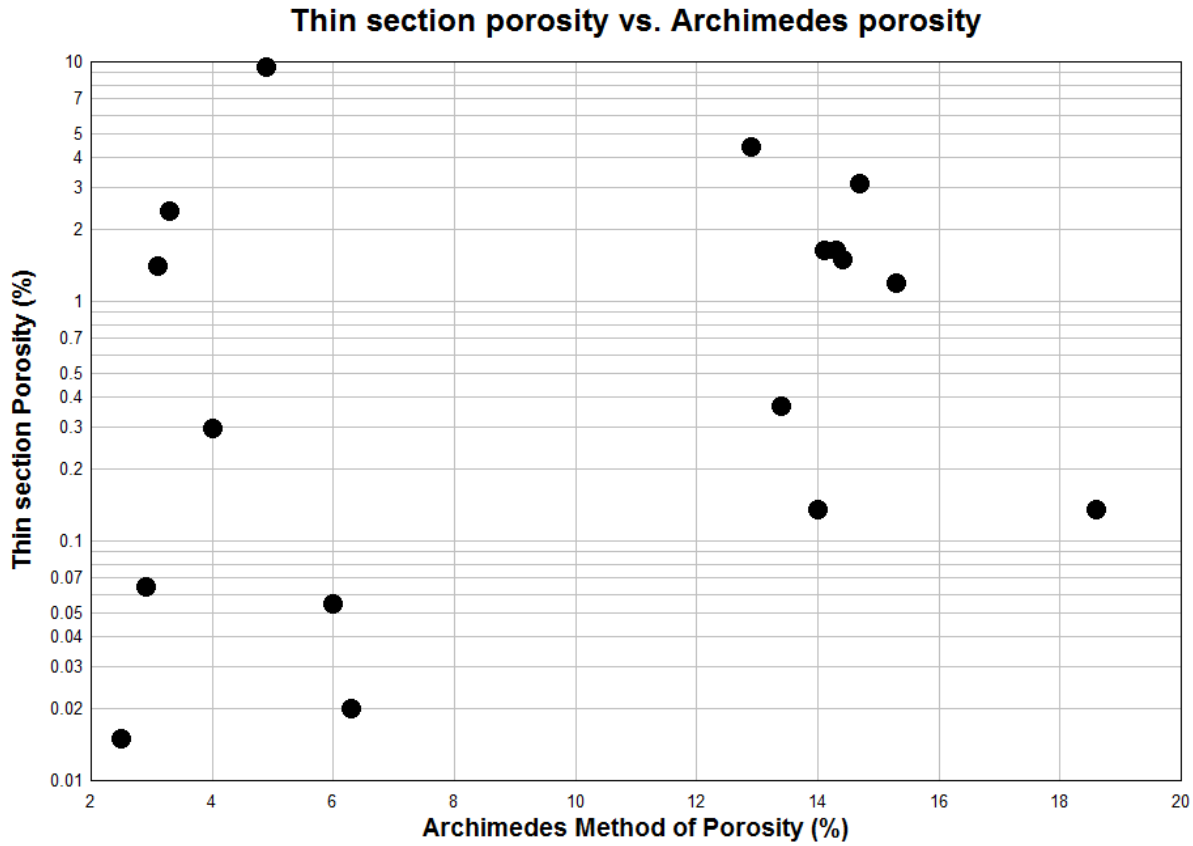

Figure 3.3 Thin section porosity % (log) vs. Archimedes porosity % (linear)

3.6 Sonic velocity

Sonic velocity was performed on both saturated and oven dried samples. Using the equations seen in section 2.3 on page 16 the Young's Modulus and Poisson's Ratio can be calculated. The presence of water in the sample generally increases the p wave velocity, with an average increase of 147m/s. The presence of water generally decreases the S wave velocity, with an average decrease of 35 m/s. The variations observed between the saturated and dry sample are what would expected as described in Section 2.3. A consistent technique of picking the arrival times of the P an S-wave was used therefore removing any subjective interpretation

Sonic Wave velocity (oven dried)					Sonic Wave velocity (saturated)			
Sample ID	**P wave Velocity m/s**	**S wave Velocity m/s**	**Young Modulus (GPa)**	**Poisson's Ratio**	**P wave Velocity m/s**	**S wave Velocity m/s**	**Young Modulus (GPa)**	**Poisson's Ratio**
NM11 2087.4 A	3284	1967	22.2	0.22	3348	1990	22.8	0.23
NM11 2087.4 B	3175	1914	20.4	0.21	3364	1904	21.0	0.26
NM11 2087.4 C	3319	1884	20.6	0.26	3297	1902	20.8	0.25
NM11 2087.4 D	3182	1968	21.4	0.19	3340	1963	22.1	0.24
NM11 2083.34 A	3186	1887	19.6	0.23	3233	1855	19.3	0.25
NM11 2083.34 B	3147	1947	20.5	0.19	3288	1961	21.4	0.22
NM2 1788 A	3536	2225	28.7	0.17	3568	2122	27.3	0.23
NM2 2254.7 A	3833	2913	35.2	0.17	4381	2484	39.6	0.26
NM8a 2525.5 B	4141	2464	39.0	0.23	4491	2543	42.8	0.26
NM8a 2525.5 C	4149	2488	38.9	0.22	3953	2432	36.5	0.20
NM11 2083 A	3212	1989	21.4	0.19	3287	1881	20.3	0.26
NM11 2083 B	3124	1935	20.1	0.19	3395	1872	20.3	0.28
NM11 2083 C	3270	2057	22.6	0.17	3366	1959	21.8	0.24
NM4 1477.2 A	3927	2400	37.0	0.20	4077	2330	36.5	0.26
NM8a 3284.7 C	3883	2180	30.2	0.27	4434	2234	33.2	0.33
NM8a 3280 C	3714	2146	29.0	0.25	3969	2346	34.2	0.23
NM2 1354.4 A	3308	1892	19.5	0.26	3568	1692	16.8	0.35
NM2 1354.2 A	3132	1850	17.5	0.23	3038	1609	14.1	0.31
NM2 1354.2 B	3327	1894	19.2	0.26	2975	1769	16.3	0.23
NM3 1743 A	3401	2238	28.6	0.12	3668	2192	30.0	0.22
NM3 1743 C	3580	2275	30.3	0.16	3873	2239	31.6	0.25

Table 3.7 Sonic wave velocities, oven dried and saturated.

3.7 Permeability

Permeability testing was performed on all oven dried samples, except for NM8a 2525.5 B which was fractured during the permeability test setup. Permeability testing was performed at a range of pore pressures appropriate to each sample. The pore pressure was selected based off the expected permeability of the sample. The higher the permeability the lower the pore pressure had to be to avoid turbulent gas flow, as Darcy's law requires laminar flow. Testing was performed at a range of confining pressures from 5MPa to 65MPa at 10 MPa intervals. Due to time and laboratory booking restrictions several samples were only tested from 5MPa to 55 MPa. The raw data output from the PDP-200 software, gas permeability and Klinkenberg corrected results can be found on the Digital Appendix. Table 3.8 shows the results of the permeability testing, note that results are the klinkenberg corrected results and therefore are considered true permeability results.

Sample ID	Confining Pressures (MPa)						
	5	15	25	35	45	55	65
NM2 1354.2 A	7.80E-17	4.94E-17	3.83E-17	3.39E-17	3.11E-17	2.78E-17	2.63E-17
NM3 1743 A	6.17E-19	8.62E-19	4.98E-19	3.62E-19	2.57E-19	1.70E-19	1.30E-19
NM8a 2525.5 C	2.01E-17	8.15E-18	5.80E-18	4.70E-18	3.98E-18	3.27E-18	2.68E-18
NM2 2254.7 A	5.16E-18	2.57E-18	1.76E-18	1.35E-18	9.91E-19	6.91E-19	6.12E-19
NM2 1788 A	3.46E-17	2.70E-17	2.36E-17	2.24E-17	2.22E-17	2.12E-17	2.07E-17
NM3 1743 C	2.95E-18	1.43E-18	9.61E-19	7.17E-19	5.63E-19	4.58E-19	4.29E-16
nm8a 3284.7 C	5.98E-18	3.02E-18	1.33E-18	8.74E-19	5.45E-19	3.76E-19	3.15E-19
NM2 1354.2 B	5.26E-17	2.29E-17	2.23E-17	1.91E-17	1.71E-17	1.62E-17	1.52E-17
NM11 2087.4 A	1.54E-16	1.38E-16	1.29E-16	1.27E-16	1.23E-16	1.21E-16	1.20E-16
NM11 2083.34 A	2.80E-16	2.55E-16	2.43E-16	2.34E-16	2.33E-16	2.27E-16	2.23E-16
NM11 2087.4 B	2.25E-16	2.01E-16	1.92E-16	1.88E-16	1.84E-16	1.81E-16	1.78E-16
NM11 2087.4 C	2.23E-16	1.95E-16	1.85E-16	1.79E-16	1.72E-16	1.72E-16	1.70E-16
NM11 2083.34 B	2.63E-16	2.39E-16	2.26E-16	2.19E-16	2.13E-16	2.08E-16	2.05E-16
NM8a 3284.1 B	1.83E-16	1.64E-16	1.55E-16	1.51E-16	1.47E-16	1.45E-16	1.42E-16
NM8a 3284.1 A	1.86E-16	1.66E-16	1.60E-16	1.57E-16	1.52E-16	1.51E-16	1.48E-16
NM8a 3284.1 C	1.68E-16	1.51E-16	1.49E-16	1.41E-16	1.39E-16	1.40E-16	*
NM11 2087.4 D	1.81E-16	1.56E-16	1.48E-16	1.45E-16	1.42E-16	1.30E-16	*
NM8a 3280	2.41E-18	1.29E-18	6.59E-19	3.63E-19	1.40E-19	1.27E-19	*
NM2 1354.4 A	3.87E-17	2.04E-17	1.57E-17	1.41E-17	1.30E-17	1.24E-17	1.18E-17
NM4 1477.2 A	1.58E-18	6.76E-19	1.32E-19	6.16E-20	2.27E-20	9.79E-21	*

Table 3.8 True permeability results. The symbol * represents an uncompleted test due to laboratory booking restrictions or time constants. This resulted in several samples only being tested from 5MPa to 55MPa confining pressure.

4 Discussion

4.1 Controls on Matrix Permeability

4.1.1 Pore Structure/Microstructure

The morphology of a rock is controlled by composition, mode of emplacement and subsequent history. A key component of morphology in the consideration of permeability is the pore structure; at the micro-scale this is the controlling property for fluid flow through a medium. The original pore structure can be modified by post depositional processes. Intrusive rocks have little initial porosity due to their formation process which results in a holocrystalline matrix. Much of their porosity forms in response to post-cooling tectonic and thermal stresses in the form of macroscopic and microscopic fractures (Lane & Gilbert 2008). Volcanic rocks have a wide range of porosities due to variables such as cooling time and gas content (Olalla et al. 2010). In addition to these variables volcaniclastic materials are also influenced by weathering and transport. Sedimentary rocks also have wide range of porosities due to the intergranular pore spaces being controlled by the size and distribution of particles. At the NGF a range of depositional process have been observed; with the intrusive tonalite from the Ngatamariki Intrusive Complex and the primary tuff, ignimbrite and volcaniclastic units observed within the Tahorakuri Formation. The type of depositional processes has resulted in variations in microstructure throughout the geothermal field.

The samples in this project were selected due to a lack of macro-scale fractures, constraining fluid flow in the sample to the micro-scale (matrix permeability).

With respect to matrix permeability, the microfracture morphology dominates the ability of fluid to flow through a rock. Two samples of vesicular basalt from Oregon Cascades had vastly different porosities, 3% and 85% , but similar permeabilities in the order of $10^{-12}m^2$ (Saar & Manga 1999). Both permeability and porosity in these samples appear to be depend upon the microstructure of the sample. Within homogenous rock types, power law regression curves have been used to describe the relationship between the porosity and permeability (Heard & Page 1982; Bourbie & Zinszner 1985; Rust & Cashman 2004; Heap et al. 2014). These relationships rely on similar microstructure throughout the samples and their correlations are often difficult to establish. The use of power law regression curves is merely a means to describe a particular data set and the correlation between porosity and permeability should not be confused with causation. When observed as a group the samples from this project appear heterogeneous with several lithologies identified, therefore a poor correlation between lithology types is expected.

To analyse the microstructure in the rocks of Ngatamariki, binary photomicrograph maps were created for each sample to identify areas of connected porosity. This was completed using the fluorescent light microscopy outlined in Section 2.4.2, with binary outputs for each thin section in available in the Digital Appendix. Two types of micro-porosity have been observed in the binary images from the Tahorakuri Formation and the Ngatamariki Intrusive Complex; microfractures and vesicles. To differentiate the two forms of porosity the definition applied by Heap et al. (2014) was used, where microfractures have a length to width ratio (aspect ratio) typically above 1:100 and vesicles typically range from 1:1 (perfectly circular) to 1:10 (oval). No sample displayed both microfracture and vesicle porosity, however the thin sections only show a two dimensional snapshot of the microstructure. These two micro-porosity morphologies have different processes of formation and react differently to changes in stress regime; increasing confining stress causes microfractures to progressively close resulting in a reduction in permeability, while elliptical pores/vesicles/vugs show very little change with increased confining stress (Guéguen & Palciauskas 1994). Microfracture closure is primarily controlled by elastic deformation, with surface roughness controlling further closure. Nara et al. (2011) found that samples with high aspect ratio microfractures maintained their influence on permeability even at the highest confining pressure (90 MPa). Low aspect ratio macrofractures are associated with relatively high permeability at low confining pressures but are easily closed by increased confining pressures. This suggests that high aspect ratio microfractures will play a large role in matrix permeability with increased lithostatic pressure.

4.1.1.1 Microfracture Analysis

Seventeen thin sections were analysed for this project with seven of these displaying microfracturing. One sample (NM2 1788 A) had no visible fractures or vesicles within the photomicrographed area. Samples NM2 1354.4 A and NM2 1354.2 A showed signs of material loss during the thin sectioning process and were removed from analysis. Crack density (area per unit volume) ranged from 2.28 – 31.77 mm^2/mm^3 with anisotropy factors ranging from 0.00 (isotropic, equal number of microfracture intercepts on predetermined x,y plane) to 0.85 (fairly anisotropic, significantly more microfracture intercepts on one plane). Figure 4.1 shows porosity plotted against microfracture density; no correlation is observed. One sample has a porosity much higher than would be expected of a sample that is controlled primarily by microfracture. Sample NM2 1354.2 B was one of two samples extracted from the same piece of core several centimetres apart. The other sample (NM2 1354.2 A), does not display any visible microfractures but had several vesicles. Sample NM2 1354.2 B displayed only microfractures in thin section, however, with such a high porosity (>18%) it can be assumed that vesicular pore spaces has contributed to the total porosity resulting in an outlying data point. This shows how variable the samples can be with two samples centimetres apart showing different pore structures.

A correlation between increased microfracture density and increased porosity has been observed in the Rotokawa andesite in the TVZ (Siratovich et al. 2014). One possible explanation for the lack of correlation in this study is that the method used to measure microfracture density only measures the number of microfractures encountered on a predefined x and y plane, it does not take into account the aperture of these fractures or their length. Also, as the microfracture density is measured from a single thin section it only represents a "snapshot" of the pore space, while the archimedean and dual-weight porosities are measured for whole samples.

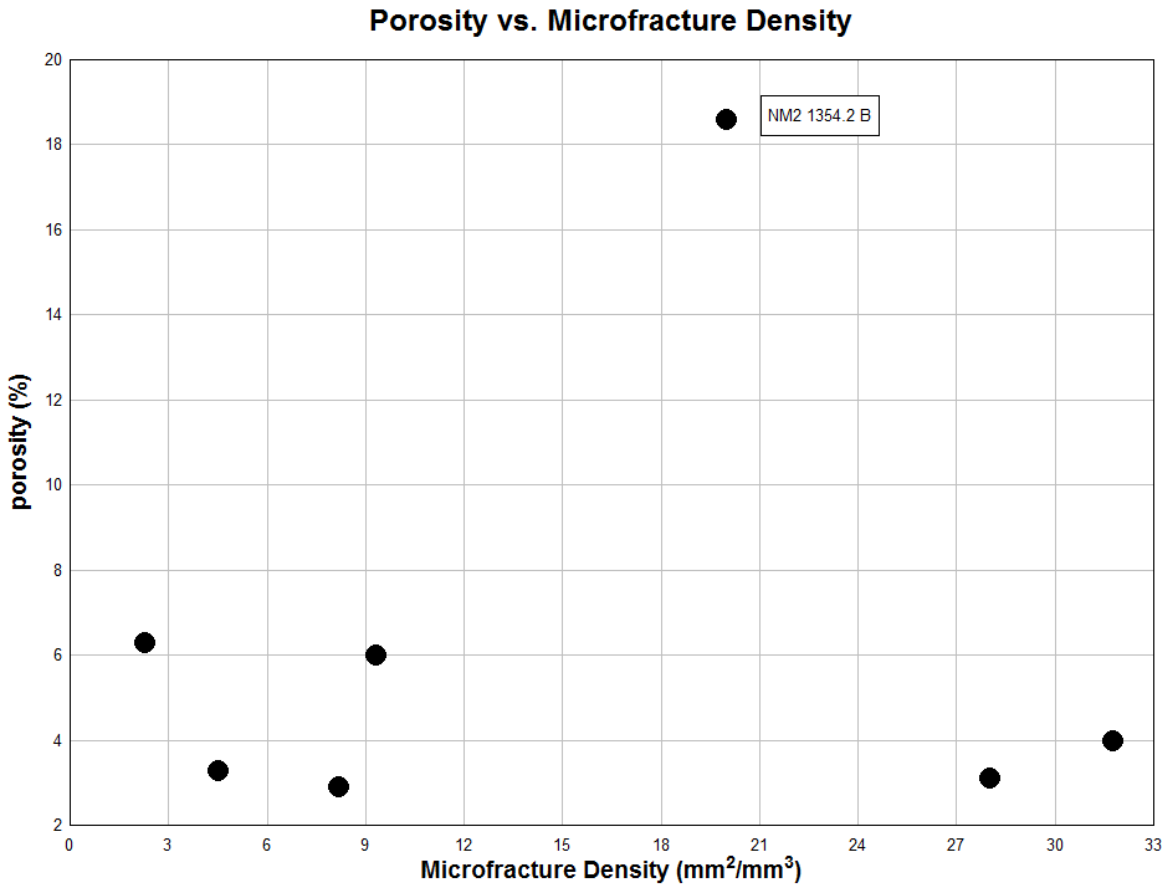

Figure 4.1 Porosity vs Microfracture density. NM2 1354.2 B appears as an outlier with a distinctively higher porosity

The microfracture density results were plotted against permeability (Figure 4.2) in an attempt to correlate microfracture density with permeability. The permeability results in Figure 4.2 are for the lowest confining pressure of 5MPa compared to microfracture density which was measured at atmospheric pressure (~0.1MPa). This provides the closest comparison between the test conditions of the microfracture density and the permeability. No clear correlation between permeability and microfracture density was observed. However, a relationship does appear to exist between the two properties however there are several large fluctuations within the data and a linear regression showed a correlation coefficient with an $R^2 = 0.11$ (poor correlation). As no other microfracture analysis was performed it is difficult to ascertain the source of the variations within the data. One possible source of error is the pressure difference between the permeability testing (5MPa) and the microfracture analysis condition (~1MPa), which could cause closure of some of the microfractures and may explain the lack of clear correlation seen in Figure 4.2.

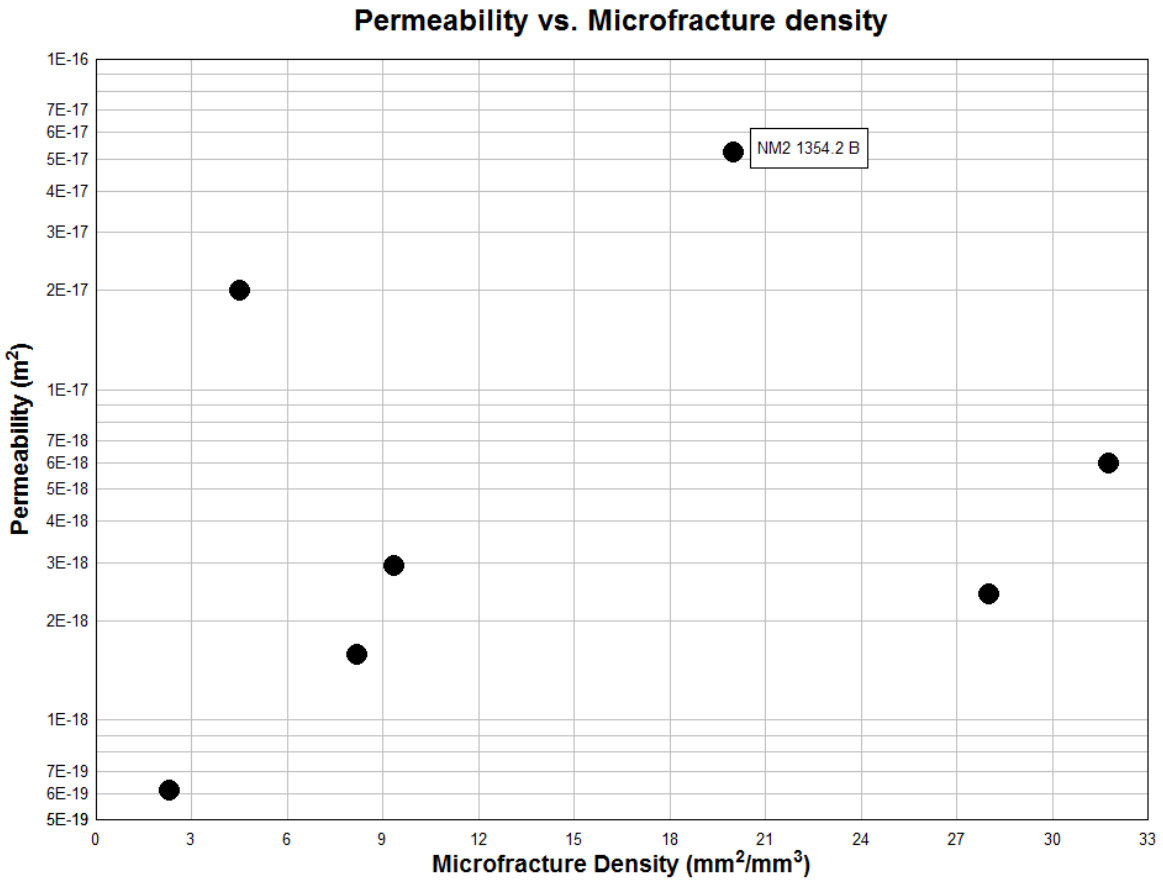

Figure 4.2 Microfracture density verses permeability. No observable trend, The outlier of the porosity vs. microfracture graph in Figure 4.1 (NM2 1354.2 B) appear to have a relatively high permeability, however is less of an outlier in this figure

4.1.1.2 Vesicle Analysis

Thin sections that displayed pores/vugs/vesicles within the field of view were further investigated to determine their influence on permeability. A series of quantitative measurements were performed using the computer software program ImageJ. The vesicular thin sections primarily consisted of samples from NM11 within a depth range of 2083-2087 mbgl, with only one other sample, NM2 2254.7 A, also displaying vesicularity. The photomicrograph image from NM2 2254.7 A, displayed one large vesicle with little other visible porosity (Figure 4.3). This is markedly different from the remaining samples from NM11 which display many smaller connected vesicle spaces, (for example Figure 4.4). Sample NM2 2254.7 A also displayed a much lower permeability than any of the samples from NM11 and it is therefore assumed that while only vesicles were observed in thin section, it is not what is controlling the permeability. Consequently it has been removed from the pore structure analysis outlined below. The following measurements were recorded: thin section porosity, average area of pore space, maximum area of pore space, average circularity, average aspect ratio, maximum aspect ratio and average roundness. The results of this analysis can be found in Section 3.3. The permeability associated with the lowest confining pressure (5MPa) was used as this provided the closest comparison between the test conditions of the two tests.

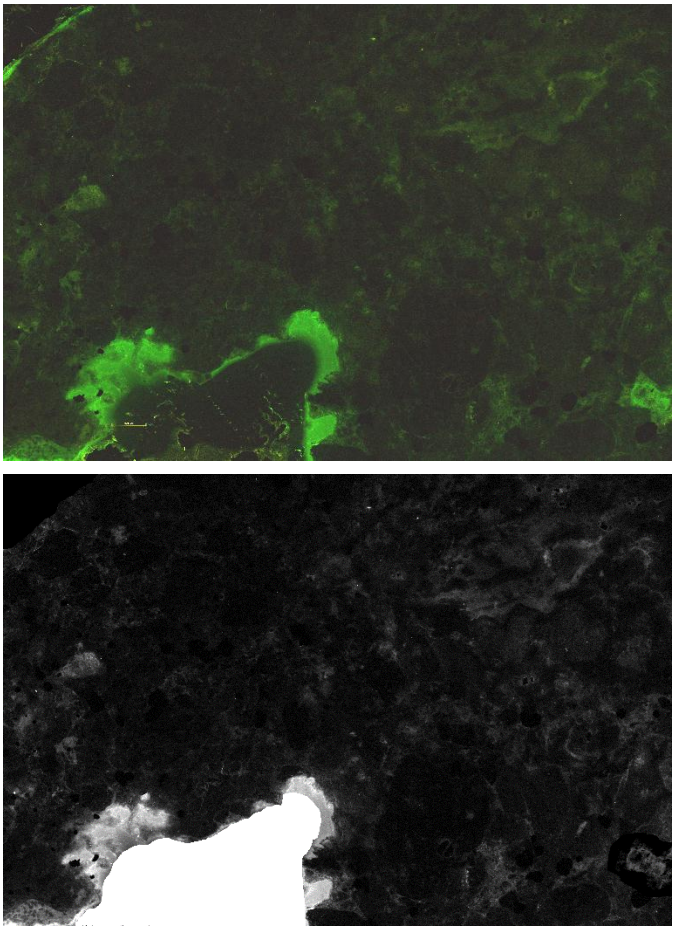

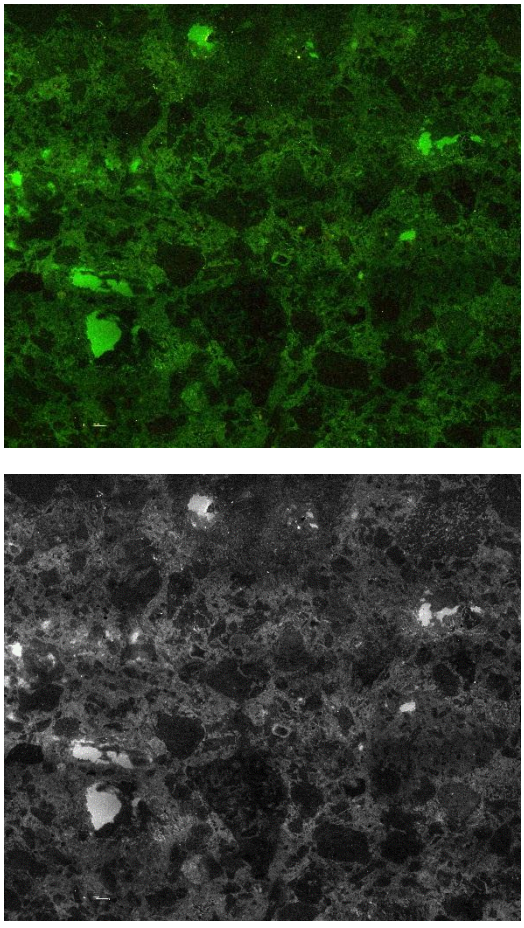

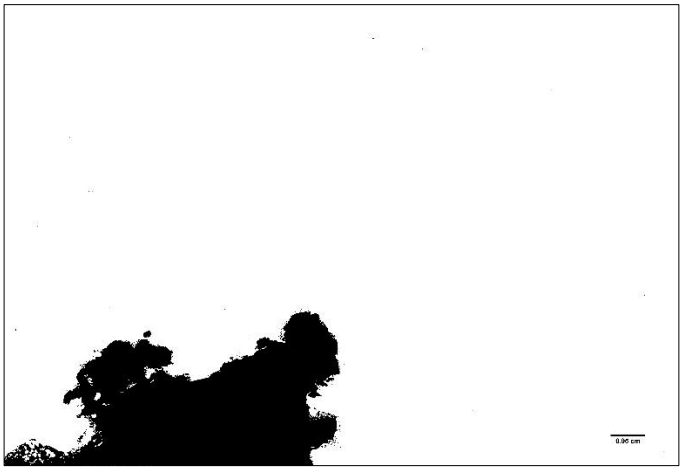

Figure 4.3 NM2 2254.7 A, large vesicle ~0.2mm with little other visible connected porosity

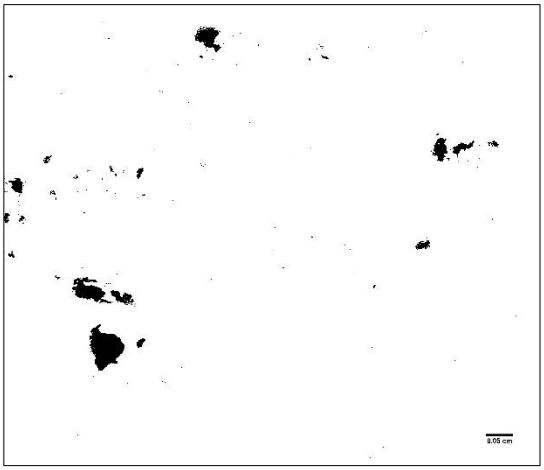

Figure 4.4 NM11 2083 B, a series of connected vesicle spaces ranging in size from ~0.07mm to ~0.005mm

Of all the quantitative vesicle analysis measurements performed only one property correlated with permeability. When circularity is plotted vs permeability a linear trend of increased permeability with increase vesicle circularity is observed (Figure 4.5).

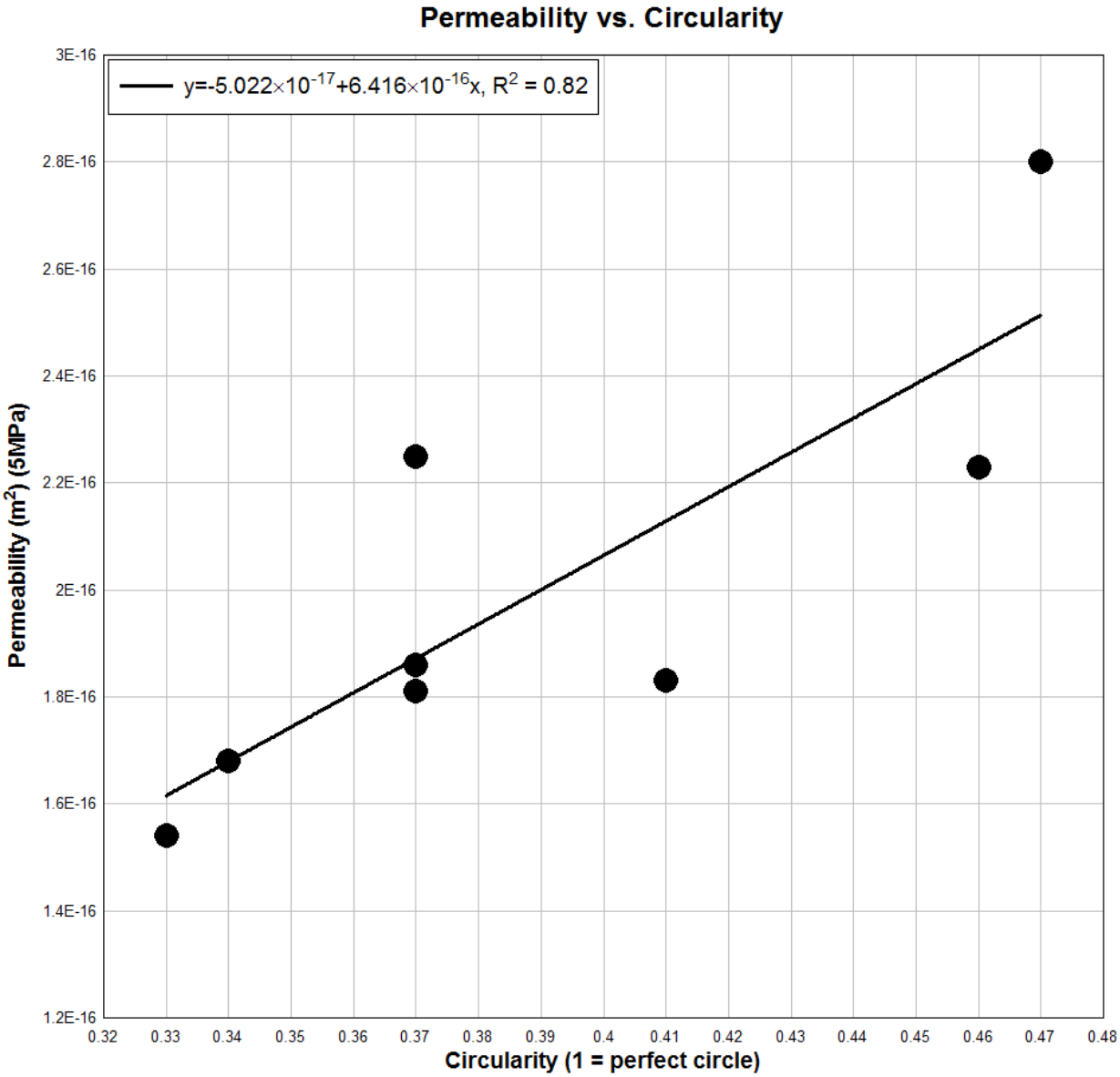

Figure 4.5 Circularity vs. Permeability. Visible trend of increasing permeability with increasing circularity. Linear Regression line has a correlation coefficient of 0.82

4.1.2 Porosity-Permeability Relationship

To compare porosity and permeability of the samples, the permeability of the lowest confining pressure (5MPa) was plotted against Archimedes porosity. Figure 4.6 shows the relationship between porosity and permeability of the samples. A series of trends were plotted to find the greatest correlation, it was found that a power law trend line gave the greatest correlation coefficient with an $R^2 = 0.65$. Other studies have found power laws to describe this relationship in volcanic rocks with Rust and Cashman (2004) describing the relationship for obsidian flow and tephra samples dominated by vesicular porosity. It was observed that considerable variation in the result was associated with the complex geometry of the partially collapsed bubble network resulting in reduced pore apertures and highly tortuous flow paths. A power law relationship is also observed in sedimentary rocks with Bourbie and Zinszner (1985) using the power law to describe the porosity-permeability relationship for sandstones samples from Ile de France region around Paris. This suggests that porosity permeability relationship are not constrained to one rock type. Heap et al. (2014) found the power law also described the porosity-permeability relationship for andesites found at Volcan de Colima in Mexico, where two "families" were identified different power law exponents. The first family consisted of samples with relatively low porosity (7 to 12%) and had a relatively high exponent of 15.9. The second family contained samples with relatively high porosity (15 to 24%) and had a relatively low exponent of 3.2. This resulted in what Heap et al. (2014) described as a cross over porosity where the two power fit trends intercept at approximately 12% porosity. An attempt was made to divide the data from this study into two distinct groups but no cross over trend was observed. Heap et al. (2014) also commented that a simple relationship between porosity and permeability in volcanic rocks simply does not exist.

There is a degree of scatter within the data from this project, where the trend is accentuated within the micro fractured samples. This trend of decreasing permeability with decreasing porosity has been observed in several other studies (Heard & Page 1982; Stimac et al. 2004; Heap et al. 2014; Siratovich 2014).

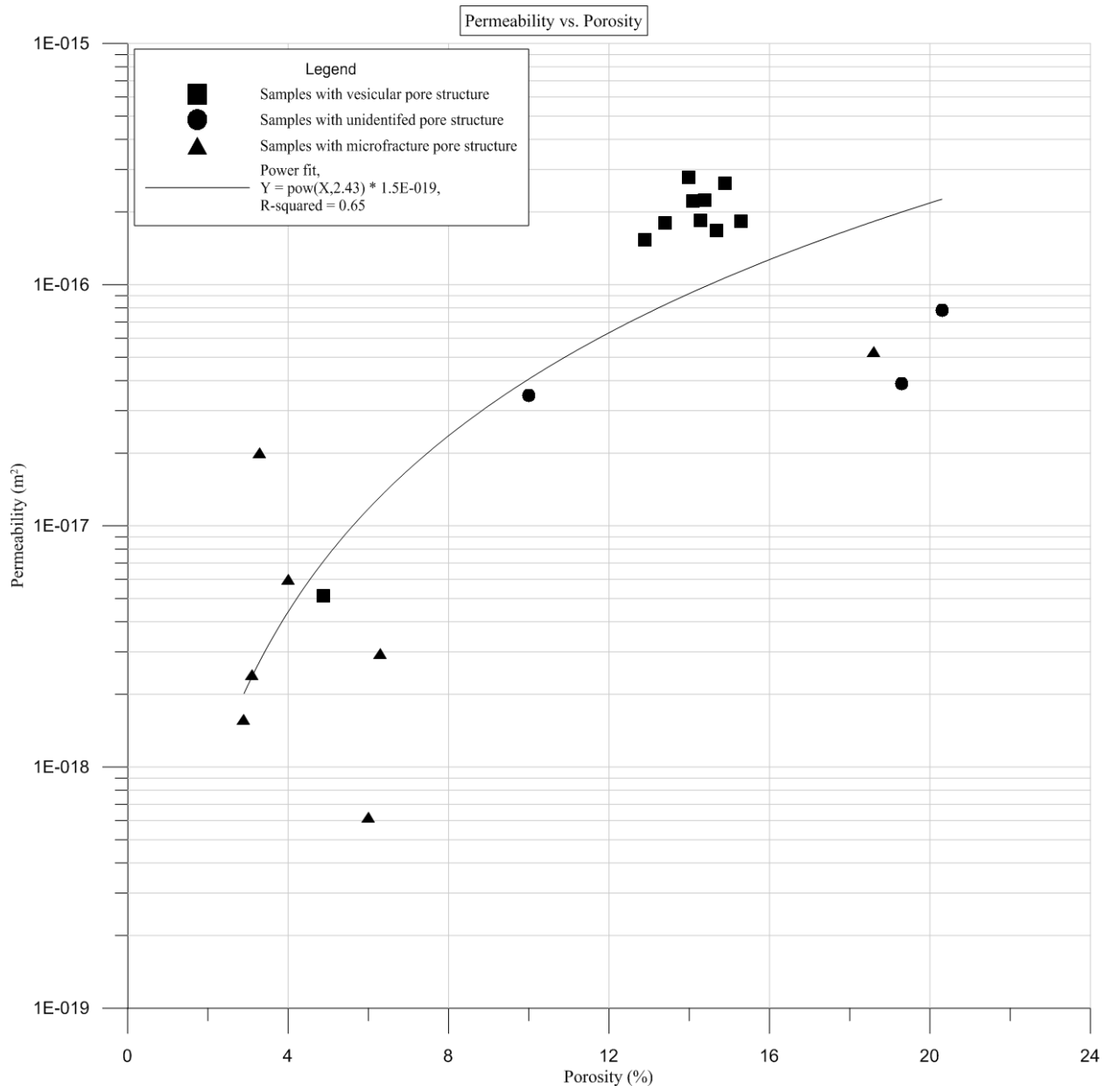

Figure 4.6 Permeability vs. porosity. Line of best fit was found to be a power fit with an R^2 value of 0.65

To further investigate the relationship between porosity and permeability, lithology types were identified to ascertain the effect on the porosity permeability relationship. Figure 4.7 shows the permeability vs porosity, with the broad lithologies identified.

The primary tuff samples have a relatively small range of permeability from 3.46E-17 m^2 to 7.80E-17 m^2 with relatively high variation in porosity from 10.0% to 20.3%. Analysis of the microstructure was only possible on one of the four primary tuff samples due to the size limitations of the received samples and difficulties creating thin sections. The one available thin section showed porosity consisting of microfractures with no visible vesicles. However as only one primary tuff sample could be analysed, limited confidence should be put on this result. Interestingly the primary tuff samples generally have a higher connected porosity than the volcaniclastics yet have a lower permeability.

Within the volcaniclastic samples there is a large variation in both the porosity and permeability with a trend of decreasing permeability with decreasing porosity. The large grouping of volcaniclastic samples with a porosity ~14% corresponds with samples from 2083-2087 mbgl at NM11 from which several samples were made. The samples with porosity values lower than 8% have a microfracture pore structure while the samples with porosity greater than 12% have a porosity consisting of vesicles. It appear that the pore structure of the volcaniclastic lithological unit can be highly varied and have large influence on the porosity and permeability

Two samples of tonalite were measured, with a relatively low porosity and permeability. There appears to be a correlation between decreased porosity and decreased permeability, however due the small sample size, this trend is tentative.

When permeability is plotted against porosity there appear to be grouping within each lithological unit (Figure 4.7). From this we can draw the conclusion that the broad lithological units have a significant role in controlling the porosity and permeability. However, the volcaniclastic rocks displayed both microfracture porosity and vesicle porosity each with vastly different permeability results. From this we must assume that the depositional processes of the volcaniclastic samples is varied resulting in different microstructure which in turn controls the porosity and permeability. This suggests that the lithologies do not constrain the microstructure of the samples.

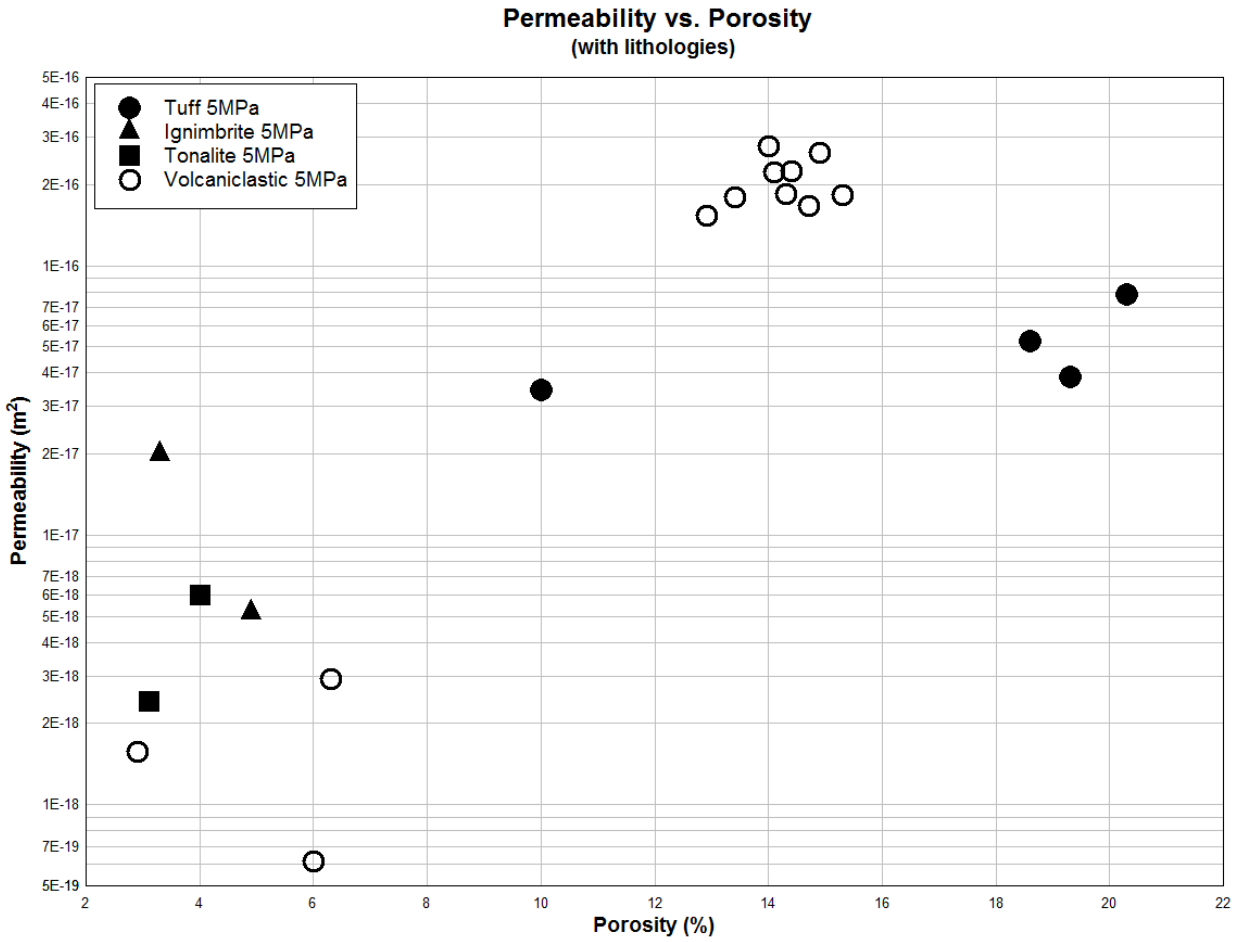

Figure 4.7 Permeability (5 MPa) vs. porosity (~0.1MPa), with lithologies identified. Observable grouping within each lithological unit however the volcaniclastic unit show several outlier associated with different microstructure.

4.1.3 Effect of Changing Confining Pressure

Permeability testing was completed over a range of confining pressures to determine the effect of pore structure on permeability with increased confining pressure. All permeability results over the full range of confining pressures can be found in Section 0. Figure 4.8 shows each sample at the lowest confining pressure (5MPa) and at the highest confining pressure that all samples were tested at (55MPa). It can be seen that the microstructure plays a large role in how each sample reacts to the changing confining pressure.

The discussion below has divided the samples into two main groups: group one consisting of all microfractured samples except NM2 1354.2B and includes sample NM2 2254.7 A (vesicular pore structure). Group two consists of all remaining samples.

Group 1: (transparent red Figure 4.8) show a relatively large decrease in permeability with increasing confining pressure. This group has a relatively low porosity and primarily consists of samples that have microfracture porosity. The one exception is the ignimbrite sample NM2 2254.7 A, which displays a very similar reaction to increased confining pressure as the microfractured samples however, thin section analysis has observed a vesicle-based porosity in this sample. The relatively large decrease in permeability for the samples is likely due to the closure of microfractures due to elastic deformation reducing both porosity and permeability within the sample.

Group 2: (transparent blue Figure 4.8) consists of samples with relatively high porosity and shows a relatively small decrease in permeability with increased confining pressure. This group consists of the volcaniclastic units and the primary tuff units with predominantly vesicular pore structure. This pore structure is likely the cause of the relatively small decrease in permeability, as increase confining pressure has little effect on elliptical pores. Of the two lithologies observed in group 2, the volcaniclastic samples show a much smaller decrease in permeability when compared to the primary tuff samples. This may indicate that the primary tuff samples have some microfractures that contribute to permeability at low confining stresses but are closed with increased confining stress resulting in a decrease in permeability.

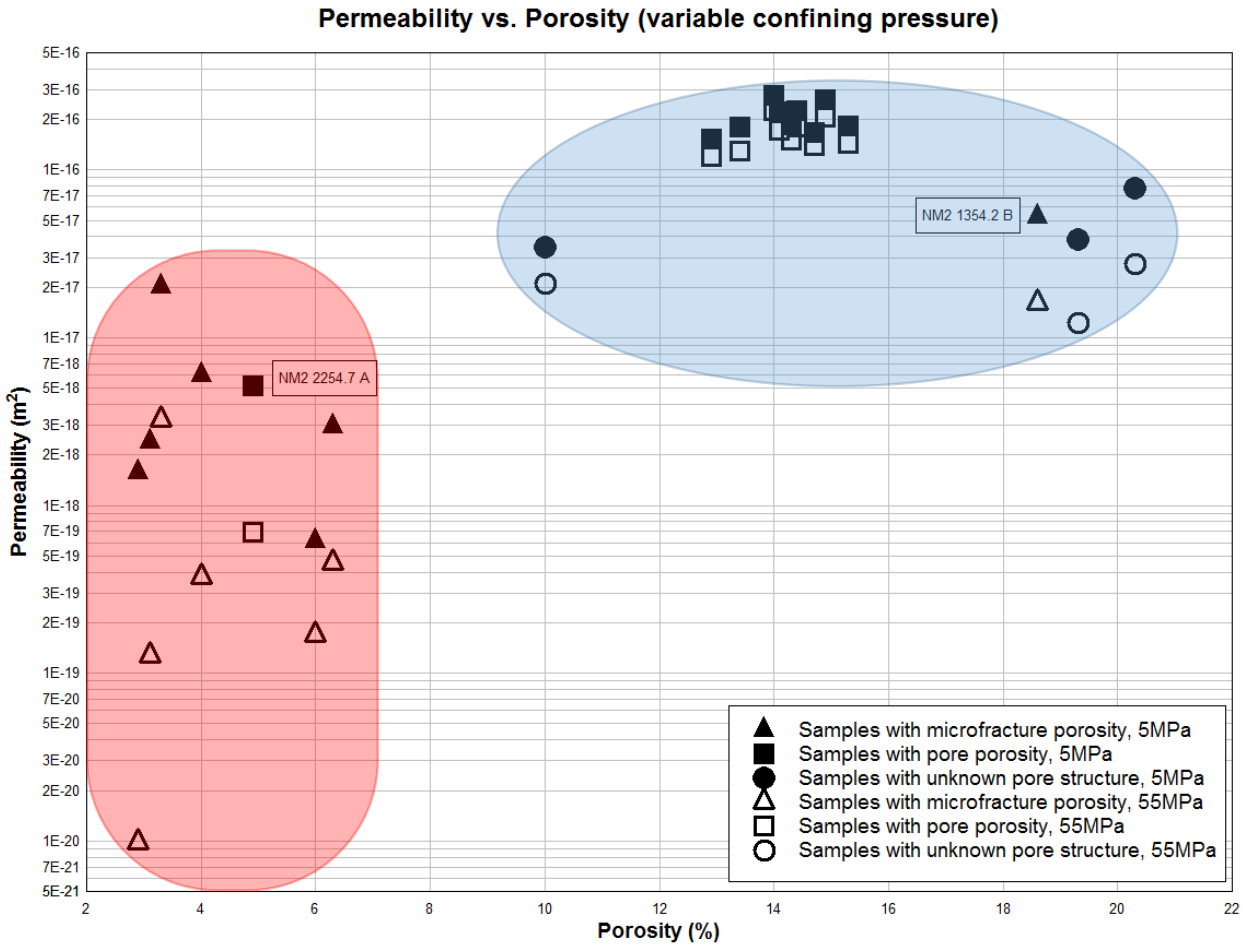

Figure 4.8 Permeability vs. Porosity, showing permeability results from both 5MPa and 55MPa confining pressures. Samples in group two (blue) have porosity primarly consisting of vesicles and show very little change in permeability with increased confining pressure. Group one (red) have porosity that primarly consists of microfractures; these samples show a large decrease in permeability with increased confining pressure. Outliers from both vesicles and microfractures exist in both groups and are discussed in the section.

Figure 4.8 indicates that the type of microstructure has a large influence on the permeability with increased confining pressure. There is also a clear correlation between microstructure type and porosity, where relatively low porosity correlates with microfractured samples and relatively high porosity correlates with porosity consisting of vesicles. There are two major outliers in Figure 4.8, this is samples NM2 2254.7 A and NM2 1354.2 B. These samples do not behave in a similar fashion to samples with the same observed microstructure. The likely explanation for this is that the microstructure identified is not representative of the tested sample. As microstructure was observed from an area of ~1 cm^2 the observed textures and pore structures may not be representative of the microstructure that controls the permeability of the sample. While sample NM2 2254.7 showed vesicular microstructure, the porosity and reduction in permeability with increased confining pressure suggest that microfractures control both the porosity and permeability

of the sample. NM3 1354.2 B displayed a microstructure consisting of microfractures, however the high porosity and reaction to increased confining pressure suggest that the pore structure is dominated by vesicles.

The decreased permeability with increased confining pressure has been attributed to the progressive closing of pore spaces. To further investigate the effect of confining pressure on permeability the permeability results at each pressure change has been plotted against confining pressure for both the microfracture porosity and the vesicle porosity (Figure 4.9 and Figure 4.10). Samples of unknown microstructure (Three primary tuff samples, NM2 1788 A, NM2 1354.2 A, NM2 1354.4 A) have been plotted with the vesicle porosity samples in Figure 4.9.This was done due to the similarity in porosity, permeability and effect of confining pressure observed in Figure 4.8.

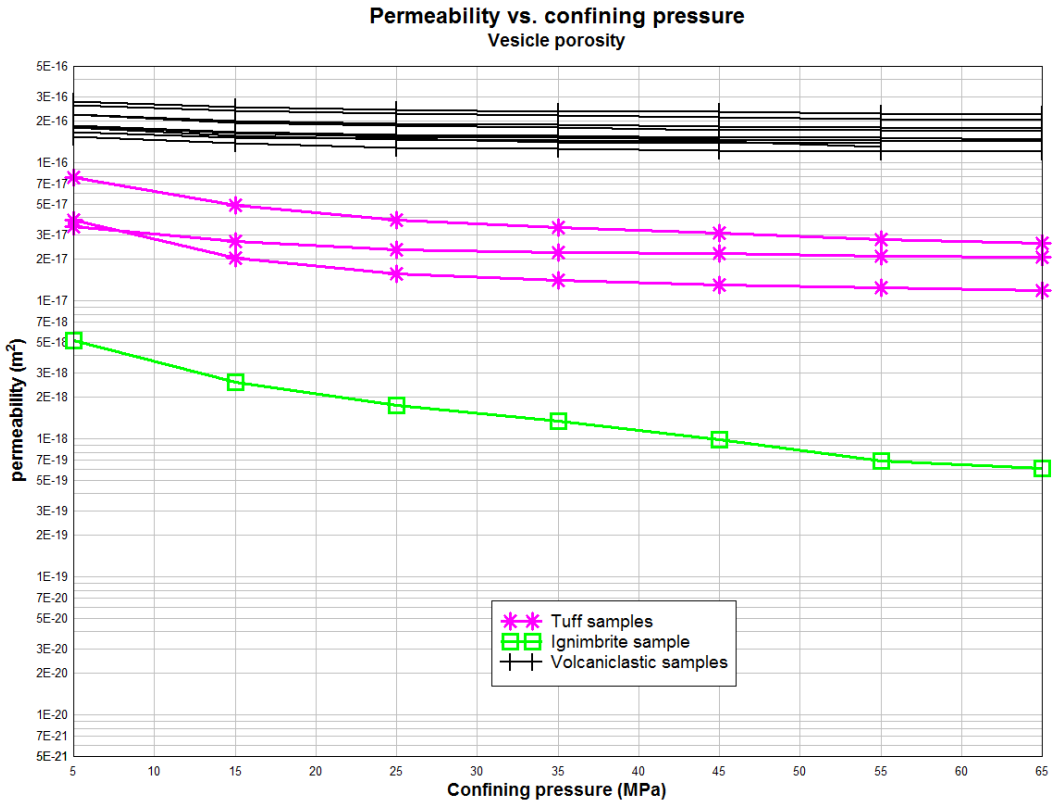

Figure 4.9 Permeability vs. confining pressure for vesicle porosity (as established through thin section analysis)

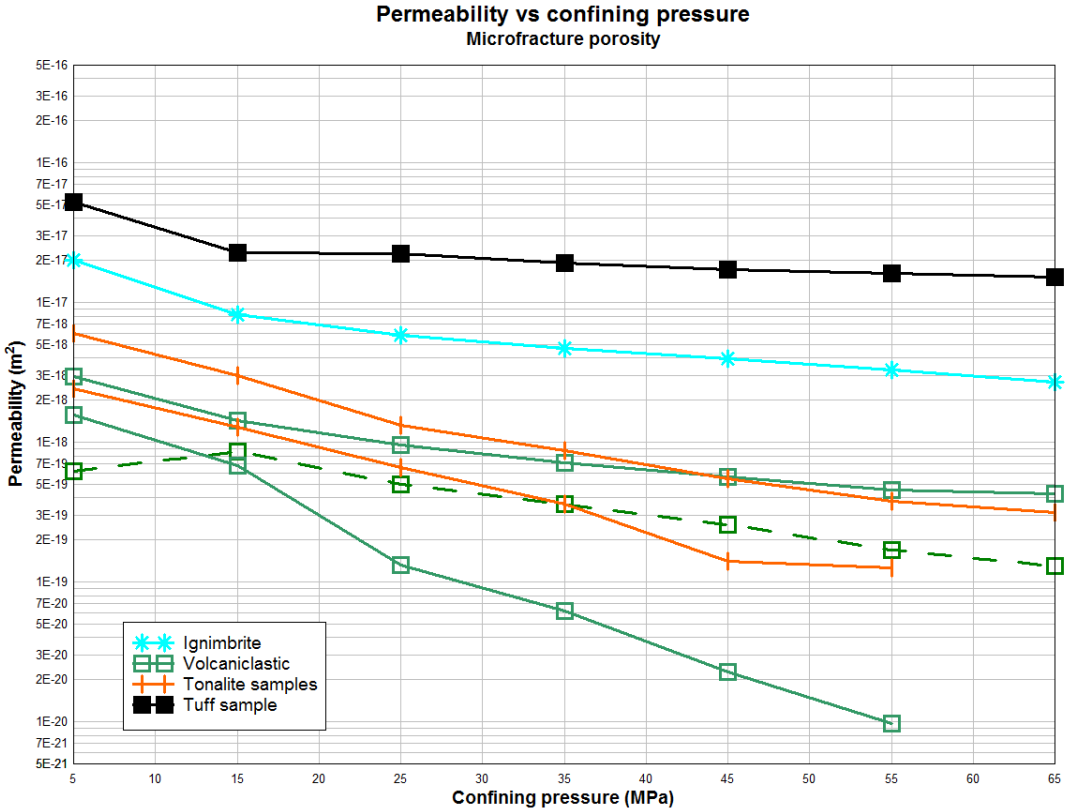

Figure 4.10 Permeability vs. confining pressure for microfracture porosity (as established through thin section analysis). Note dashed Volcaniclastic sample displays an increase in permeability between the 5MPa and 15MPa confining pressure. This is likely due to sample not being in equilibrium during testing

Vesicle porosity: From Figure 4.9 it is apparent that increasing confining pressure has little effect on the permeability for the majority of the samples. The volcaniclastic samples show the lowest decrease in permeability with increased confining pressure. The steepest gradient is between 5-15MPa for all samples. The primary tuff samples show a steeper gradient than the volcaniclastic samples. The ignimbrite sample shows a steeper gradient than both the volcaniclastic and primary tuff samples. This is the sample NM2 2254.7 A observed in Figure 4.8 as having similarities with the microfractured samples. The gradient remains relatively constant from 5-65MPa suggesting that pore were being steadily closed by the increased confining pressure. When compared to the ignimbrite sample in Figure 4.10, it can be seen that both trends are very similar suggesting that they have a similar microstructure. The trend observed with the Ignimbrite sample is very different to all other vesicular porosity samples and is further evidence that sample NM2 2254.7 A contains predominantly microfracture pores. A linear regression fit of the average vesicle curve was performed. The gradient of the fit was $-7.177e^{-19}$.

Microfracture porosity: In Figure 4.10 a clear correlation between increased confining pressure and decreased permeability can be observed. For most samples the gradient appears steepest at the lower confining pressures (5-25MPa) and a slightly shallower gradient as the confining pressure increased (25-65MPa). The volcaniclastic sample with the permeability value of $9.79E^{-21}$ m^2 at 55mpa, shows a much steeper gradient than the other samples; this gradient does not decrease with increased confining pressure as observed in the other samples. This suggests that microfractures were increasingly being closed by each increase in confining pressure. Another volcaniclastic sample (dashed green line, Figure 4.10) shows an increase in permeability between 5MPa and 15MPa. This is likely due to the sample not being in equilibrium with the confining pressure before the testing was started. A linear regression fit of the average microfracture curve was performed. The gradient of this fit was $-1.416e^{-19}$.

When compared to the microfracture linear regression fit it can be seen that vesicular porosity sample have a shallower gradient. The observed difference in the gradients has been attributed to the different pore structures. The steeper gradients observed in the microfractured samples has been attributed to the progressive closure of microfractures as the confining pressure is increased.

It can be seen from Figure 4.9 and Figure 4.10 that there is a large difference in the response to increased confining pressure. The two gradients show that the microfractured samples have a larger reduction in permeability than the vesicles samples. Attempts were made to correlate the microstructural quantitative measurements (i.e. microfracture density, circularity, aspect ratio etc.) with permeability but no correlations could be found.

4.1.4 Summary of Controlling Factors of Permeability

The microstructural analysis has revealed much about the pore structure of the samples from Ngatamariki. It is apparent the broad lithological units of the samples do not define the type of pore structure in each sample, with the volcaniclastic and primary tuff units showing both microfractured samples and vesicular samples (note; only one primary tuff thin section was usable with the other samples having their pore structure defined by the response of permeability to increased confining pressure). Samples with microfractured pore structures tended to have relatively low porosity values (<8%), while samples displaying vesicular pore structure tended to have higher porosities (>10%). The identified pore structure type (i.e. vesicles or microfracture) also plays a large role in the permeability with microfractures typically having lower porosities and permeabilities than vesicular samples.

Of all the quantitative microstructural analysis only vesicle circularity appear to correlate with permeability. The lack of correlation between the other quantitative microstructural measurements and permeability can likely be attributed to the photomicrograph thin section images not being truly representative of the sample. This is reflected in the difference between thin section porosity and Archimedes porosity (Figure 3.3), where no clear correlation between the two can be found. A study by (Heap et al. 2014) found a clear correlation between thin section porosity and true connected water porosity. Figure 3.3 shows that no correlation could be found between the two types of porosity in this project. This suggesting that the photomicrograph images are not representative of the true connected water porosity. This could be due heterogeneity of the sample resulting in photomicrograph images that do not represent the porosity of the sample.

The type of pore structure also appeared to dictate the response of permeability with increased confining pressure, with microfractured samples showing progressively lower permeability with increase confining pressure. Vesicular samples showed a relatively low decrease in permeability

with increased confining pressure with the largest decrease in permeability between the two lowest confining pressure (5MPa to 15 MPa). These samples showed relatively little response to further increases in confining pressure beyond 15MPa. Two samples were identified as possibly having the microstructure incorrectly identified by thin section analysis. These samples displayed porosity and permeability characteristics that conflicted with the thin section interpretation. From this it was concluded that thin section analysis provides good assessment of a small section of the rock, however, many of the samples displayed heterogeneity therefore the interpretation provided by the thin section may not be truly representative of the whole sample.

4.2 Burial Diagenesis

4.2.1 Background

Burial diagenesis is the process of changing physical and mechanical properties within a rock mass as a result of increasing pressures associated with the progressive burial of said rock mass (Lewis & McConchie 1994). This process begins from the moment of deposition and lasts until the resulting materials are moved into the realm of metamorphism (McIlreath & Morrow 1990). Burial diagenesis results in compression, consolidation and ultimately compaction of the material. In an idealised model, burial diagenesis would predict the following changes in mechanical properties within a homogenous material: an increased density and sonic velocity with depth while also causing decreased porosity and permeability (McIlreath & Morrow 1990; Barton 2007; Cook 2010; Glassley 2010). This is most prevalent in unconsolidated materials as they have relatively high initial porosity due to the deposition method (Guéguen & Palciauskas 1994). The Tahorakuri Formation provides an ideal setting to observe the effects of burial diagenesis, as the material consists of initially unconsolidated volcaniclastic material. Also, the thickness of the unit (0.8 - 1.7 km) offers the ability to test and analyse samples from a large range of depths. The Tahorakuri formation has also undergone complex post depositional alteration and mineralisation related to the Ngatamariki geothermal system that has influenced both its physical and mechanical properties. Burial diagenesis has been studied in several other geothermal fields including; Tiwi in Philippines (Stimac et al. 2004), Eromanga basin in Australia (Dillinger et al. 2014) Wairakei in New Zealand (note only porosity with depth correlated) (Mielke 2009), Salton Sea in California (Tewhey 1977) and described by (Glassley 2010). Stimac et al. (2004) observed large fluctuations in porosity with depth which they attributed to changes in lithology. These fluctuations were as large as 7%. It was also observed that porosity and permeability decreased to the point where it affects the ability of the rock mass to be used as a geothermal resource.

Samples from a range of depths within the Tahorakuri Formation (1354 - 3280 m) have been analysed to investigate the effect of burial diagenesis on tested mechanical properties. The following physical properties have been analysed: porosity, permeability, density and sonic velocity. The effect of burial diagenesis on porosity and permeability is of special interest as these two interrelated properties are primary controlling parameters in the economic use of geothermal systems for energy production.

4.2.2 Density

The density measurements from the samples ranged from 2080 kg/m^3 to 2670 kg/m^3. When plotted against depth there are no clear correlations between density and depth. However, when a trend of increasing density with depth is observed with large fluctuations (Figure 4.11). This suggests that burial diagenesis is affecting the density of the sampled rocks at Ngatamariki, however other factors are causing large variations within the data. These large variations in the density of the Tahorakuri formation can likely be ascribed to the variation in lithologies seen in this formation, described by Eastwood (2013) and observed in hand samples and thin section analysis (Section 7.1). These lithologies have different microstructure and mineralogy which have a direct impact on the densities of the rock. While the effect of burial diagenesis appears to influence these samples, the factors mentioned above also appear to play a large role in controlling the density within the Tahorakuri formation. One factor that is not taken into consideration is the effect of elastic deformation due to the lithostatic stresses. It may be that there are changes in physical and mechanical properties when the samples are removed from depth as a result of the decreased pressure. Density testing was performed at atmospheric pressure ≈0.1 MPa while the in-situ pressure for the samples is as high as 34 MPa, as seen in section 2.5.

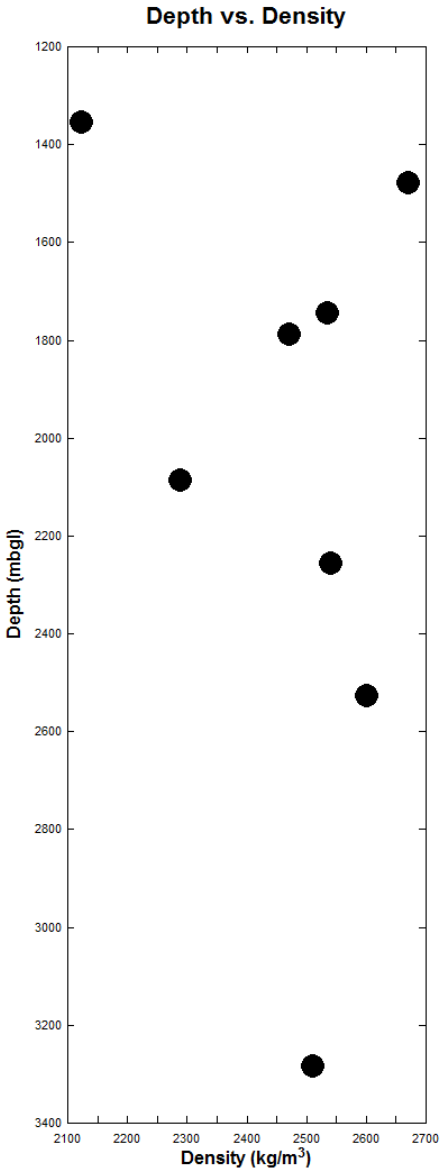

Figure 4.11 Depth vs density at Ngatamariki, with samples from same depth densities averaged.

4.2.3 Porosity

The samples tested show a large range in porosity from 2.5% to 20.9%. When plotted vs depth no clear correlation could be found between porosity and depth. However, an overall trend of decreasing porosity with depth is observed. The porosity has a reverse trend to that observed in density versus depth (Figure 4.11). This is an expected and well documented relationship between porosity and density (Akinyemi et al. 2012; Rahmouni et al. 2013; Wyering et al. 2014). The method for porosity testing has the same short comings of density where tests are performed at atmospheric pressure therefore do not take into account the effects of lithostatic stress on the elastic proporties of the rock. The porosity test method used is the standard test method, as in-situ porosity is difficult to perform and beyond the scope of this project.

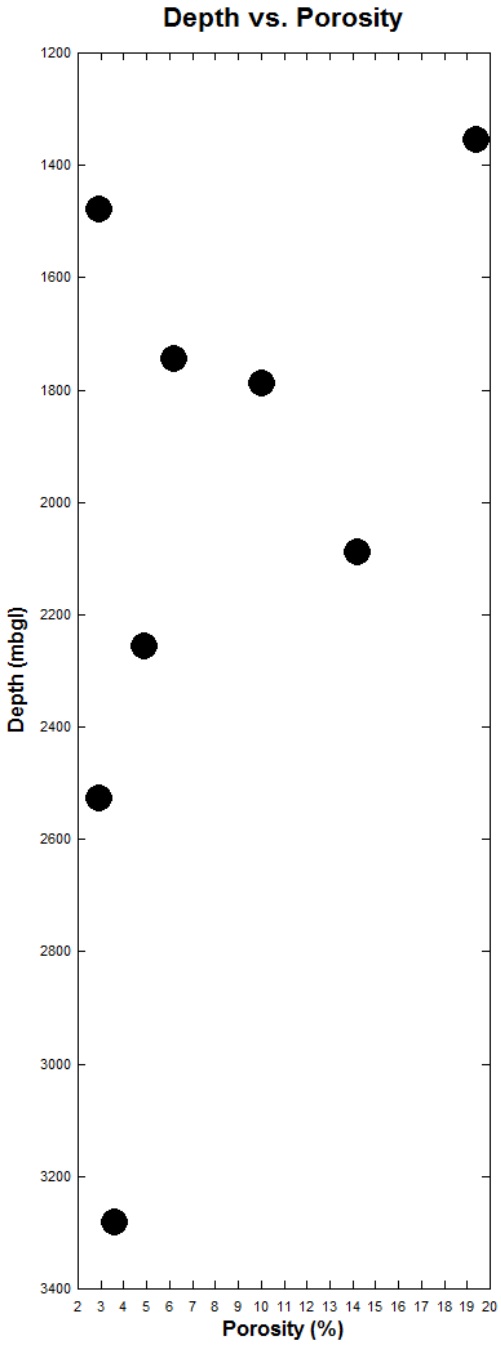

Figure 4.12 Depth vs. porosity at Ngatamariki

4.2.4 Density vs. Porosity

When density is plotted against porosity a clear linear trend can be seen where increasing porosity correlates with decreasing density (Figure 4.13). The two tonalite samples (green) appear to be on a separate trend line to the samples from the Tahorakuri Formation. This is likely due to the compositional differences in the tonalite when compared to all other tested samples. The deviation from the trend of the Tahorakuri formation suggests that specific gravity of the minerals that comprise the tonalite (primarily quartz) are slightly lower than that of the Tahorakuri Formation samples. This may be attributable to the relatively high specific gravity alteration minerals found in many of the Tahorakuri Formation samples like chlorite, epidote and calcite (Pellant & Taylor 2000).

There is grouping of samples from same depths (NM11 2083-2087 mbgl) around a central density/porosity value (14.2% porosity, 2287 kg/m^3 density). There is some variation around this central point due to the heterogeneous nature of volcaniclastic deposits resulting in variations in both density and porosity. These variations primarily fall along the linear trend suggesting a correlation between porosity and density within samples from a single depth. There are several minor outliers, however, these can likely be explained by slight variations in specific gravity, along with the associated errors involved in laboratory testing.

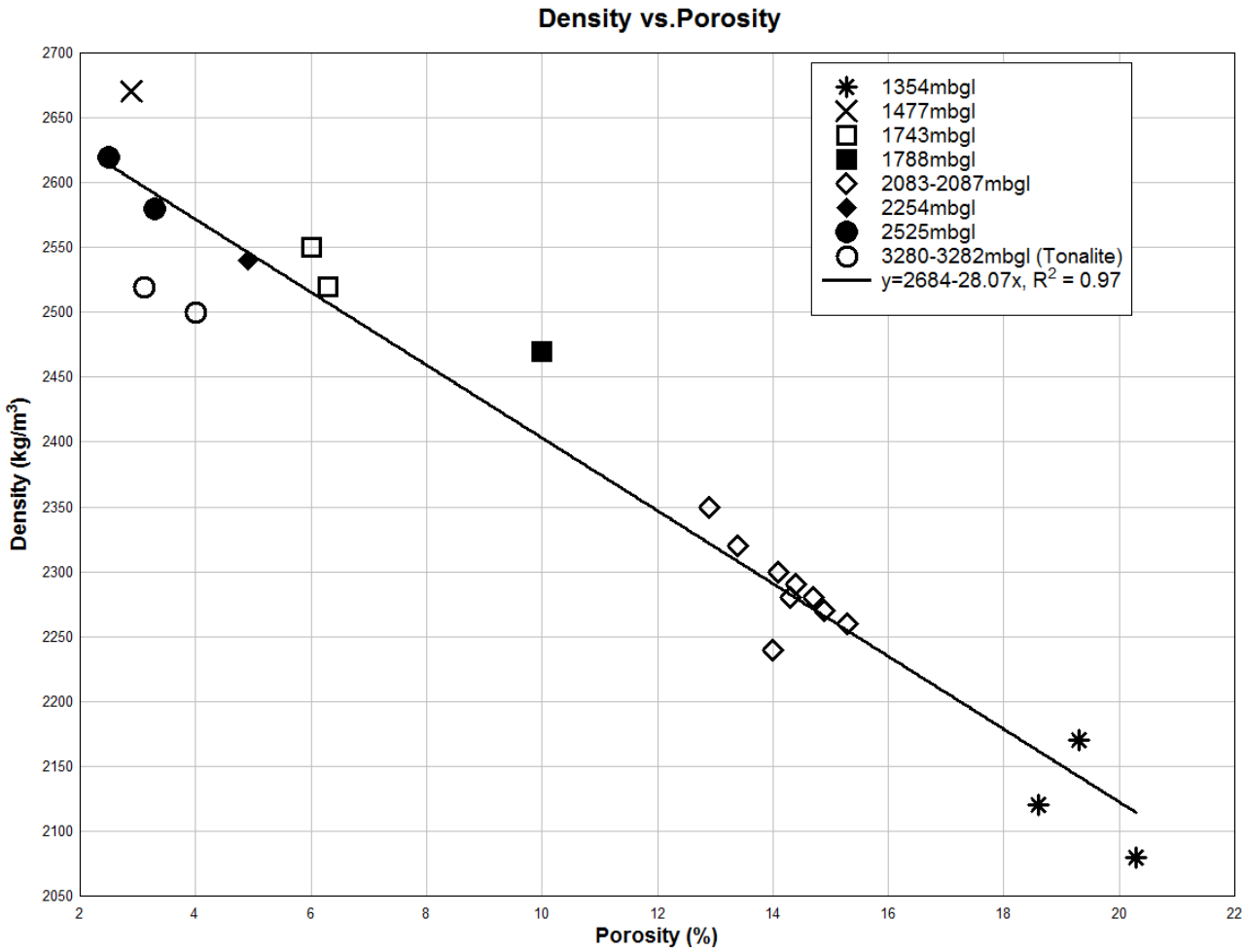

Figure 4.13 Density vs. porosity of sample from Ngatamariki Geothermal field.

4.2.5 Effect increased depth on mineralogy

At Ngatamariki, increased depth is associated with increased geothermal fluid temperatures (Catherine Boseley 2010) with the thermal gradient steepest around NM2 and NM3. The effects of hydrothermal alteration can be observed in thin section by the transformation and replacement of certain minerals. Two key minerals observed in thin section were calcite and epidote. Both of these are secondary minerals emplaced by hydrothermal fluids with epidote indicating temperatures of 220-340 ˚C and calcite indicating temperatures of 90-320 °C (Reyes 1990). With increased temperature epidote can replace interstitial calcite (Tewhey 1977). The effect of increased depth/temperature on the mineralogy was performed using thin sections of several lithologies. This was completed using the shallowest and deepest sample from each lithology types. Two units were chosen due to their different trends of porosity and density with depth. The first is the volcaniclastic units which display an unusual trend of decreasing density and increasing porosity with depth. The second is the primary tuff units which shows an increase in density and a decrease in porosity with depth.

The volcaniclastic samples chosen were: NM3 1743 C (shallow) and NM11 2087.4 A (deep). Both samples contain calcite, however the shallower sample has markedly more than the deep sample. The shallow sample had no visible epidote while the deep sample was composed of ~10-20% epidote in the form in both veins and radial structures. This suggests a higher temperature for the deeper sample as epidote has a higher temperature range. It is possible that the epidote has replaced some of the calcite as observed in Salton Sea (Tewhey 1977). The deep sample also show higher alteration in feldspar minerals and overall had increased lithic clasts. Figure 4.14 shows an epidote vein from sample NM11 2087.4 A. The epidote has caused cementation of microfractures found within the sample resulting in a porosity and permeability decrease. This is direct evidence of geothermal alteration reducing porosity and permeability of the rock. Radial epidote was also observed in the deep sample (Figure 4.16 and Figure 4.17) and consist of long spindly epidote grains extending from a central point. When observed in fluorescent light the radial epidote structures are associated with areas of connected porosity (Figure 4.17). It is therefore likely that these radial epidote structures were formed in void spaces within the rock.

There is no indication within the mineralogy that explains the increase in porosity and decrease in density observed in volcaniclastic units within the Tahorakuri Formation. There is evidence of

alteration minerals within the samples suggesting either replacement of primary minerals or infilling of pore space.

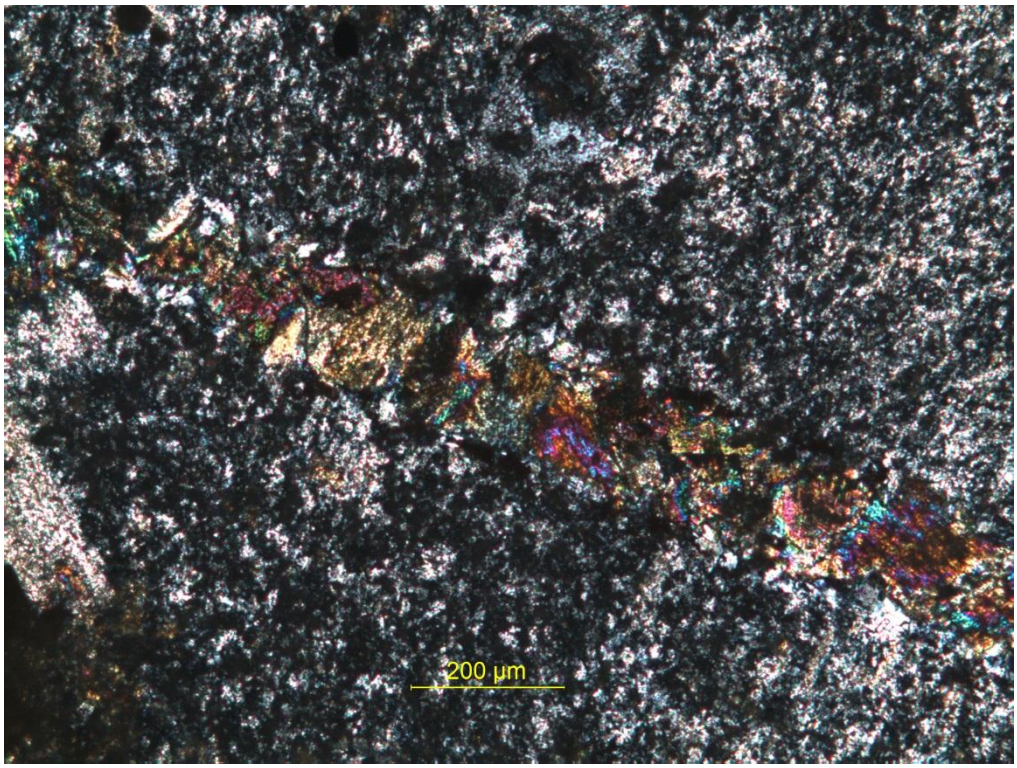

Figure 4.14 Epidote vein observed in TS8, NM11 2087.4 A. Causing a reduction in both porosity and permeability.

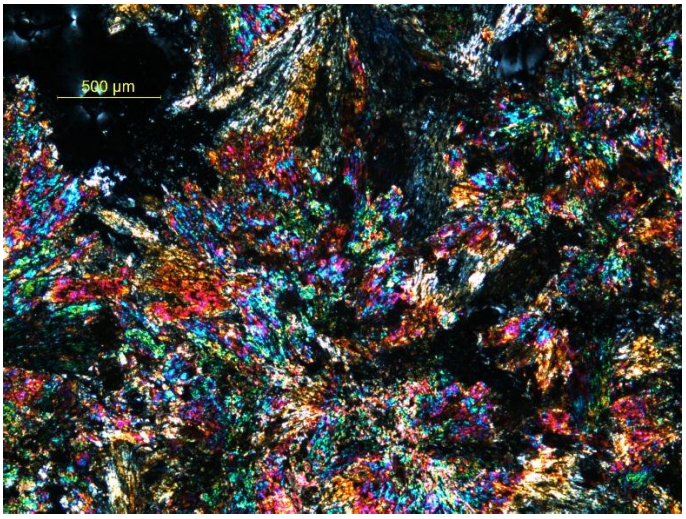

Figure 4.15 Radial epidote observed in sample NM 11 2083 A, in plane polarise light the radial structure is evident

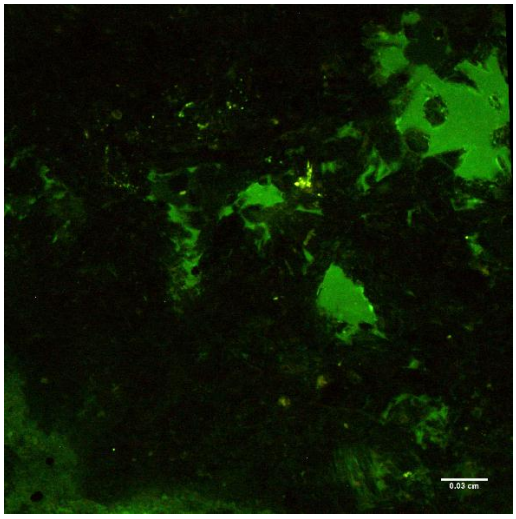

Figure 4.16 Connected porosity observed in radial epidote, sample NM 11 2083 A

The primary tuff samples chosen were NM2 1354.2 B (shallow) and NM2 1788 A (deep).This lithology has a very similar trend with depth as the volcaniclastic with the shallow sample showing relatively high calcite content and the deep sample showing lower calcite content. The deep sample also contained epidote, like the volcaniclastic this suggests that increased temperature with depth. The deep sample also showed epidote forming in interstitial space of resorbed feldspars minerals (Figure 4.17) however no epidote veins were observed in thin section

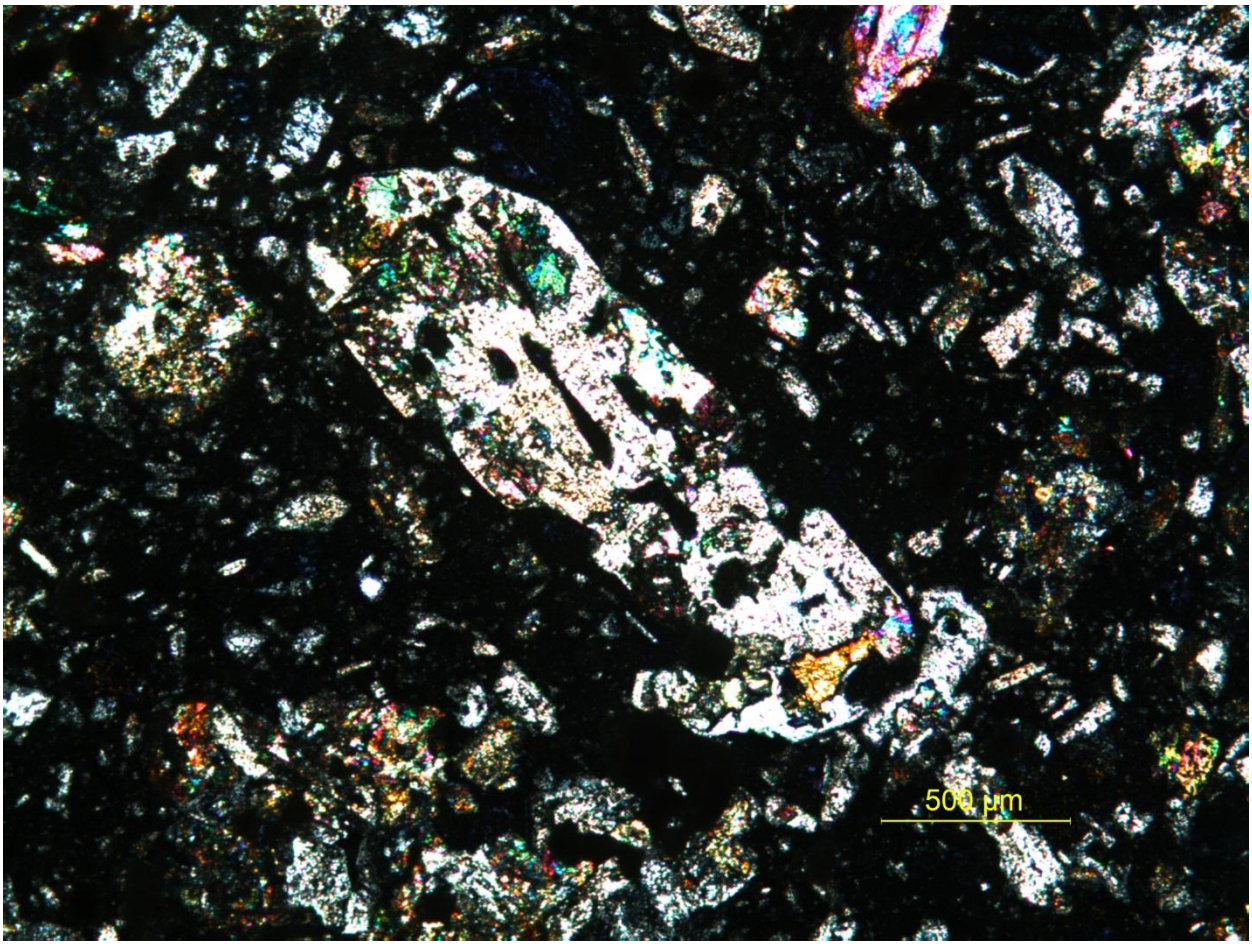

Figure 4.17 Resorbed feldspar with epidote forming in the interstitial cavities of the deep sample (NM2 1788 A)

The introduction of these secondary minerals has resulted in interstitial spaces in the matrix becoming completely or partially occupied by these minerals. This results in a decrease in the porosity and permeability.

Both the primary tuff and the volcaniclastic samples showed variations in hydrothermally deposited minerals with depth. All observed alteration appeared to reduce the porosity and permeability by cementing microfracture and filling open vesicles. This suggests that increased depth correlates with increased hydrothermal alteration which in turn would suggest a decrease in porosity and an increase in density with depth. This trend of decreasing porosity and increased density was observed within the primary tuff units however the volcaniclastic units have a trend of increased porosity and a decreased density with depth. It is therefore suggested that while the hydrothermal alteration must contribute to the effects of burial diagenesis by reducing porosity and increasing density the primary textures of the deposited lithologies plays a much larger role in controlling the mechanical properties.

4.2.6 Ultrasonic Wave Velocity

Oven dried sonic velocities ranged from 3124 m/s to 4149 m/s for P-wave velocities and 1850 m/s to 2488 m/s for S-wave velocities. Saturated sonic velocities ranged from 2975 m/s to 4491 m/s for P-wave velocity and 1690 m/s to 2488 m/s for S-wave velocities. The P-wave results show that the saturated samples have a noticeable increase in wave velocity compared to the dry samples, while the saturated and dry S-wave velocities remained relatively similar. This phenomenon has been observed in other studies (Heap et al. 2013; Heap et al. 2014) and is likely due to nature of the wave forms. The saturation of the samples causes and increase in the in both the frame modulus and bulk density, however usually the modulus increases by a greater relative amount. As the equation for P-wave velocity has frame modulus divided by density this resulting in P-wave (sat) > P-wave (dry). As the S-wave velocity equation has shear modulus divided by the bulk density saturation causes an increase in bulk density but shear modulus resulting in S-wave (dry) > S-wave (sat) (Guéguen & Palciauskas 1994). Figure 4.18 shows a large amount of variation with depth but with a general trend of increasing ultrasonic velocity with depth. When lithologies are identified, (Figure 4.19) trends appear within each lithological unit. The ignimbrite and tuff samples show an increasing P-wave velocity with depth while the volcaniclastic samples show a decreasing P-wave velocity with depth. These observed changes are likely due to variations in both the porosity and the density.

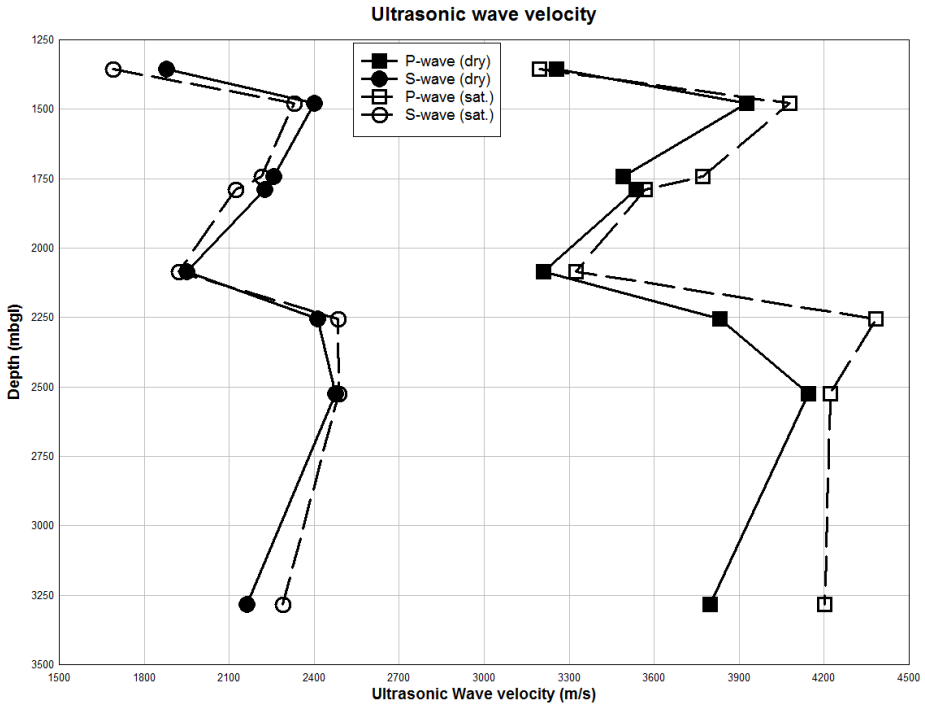

Figure 4.18 Depth vs. ultrasonic wave velocity with both saturated and dry samples

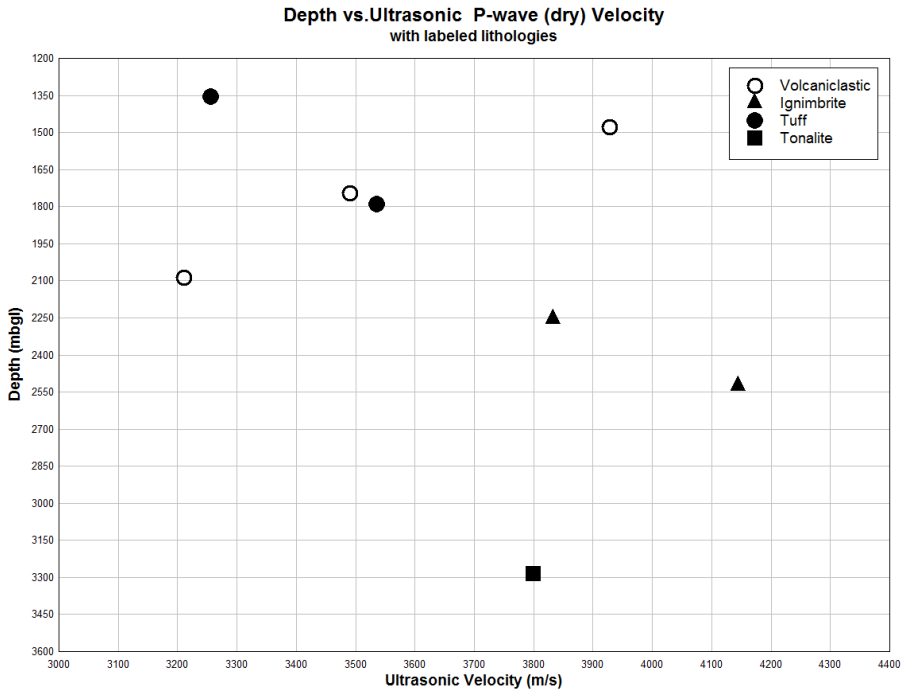

Figure 4.19 Depth vs. ultrasonic wave velocity with lithological units shown and lithological trends plotted.

With increased P-wave velocity the following changes in mechanical properties have been observed; increased dry density, decreased porosity, increased compressive strength, and increased tensile strength in a range of rock types (Barton 2007; Vasconcelos et al. 2008; Khandelwal 2013; Wyering et al. 2014). By plotting several of these properties, such trends emerge for the tested samples. In Figure 6, when ultrasonic velocity is plotted vs. density a clear trend can be observed where increasing density is correlated with increasing sonic velocity. There is also a clear trend where decreasing porosity correlates with increasing P-wave velocity (Figure 4.21). Several other microstructural properties were also plotted vs P-wave velocity. Crack density, average pore area and aspect ratio (Figure 4.22, Figure 4.23 and Figure 4.25) show no correlation with sonic velocity. Average pore circularity (Figure 4.24) shows no clear correlation with sonic velocity however, a relationship potentially exists between increasing ultrasonic velocity and decreasing circularity, however there is a large amount of scatter within the data set. Further tested would be required to confirm this relationship. From this it can be deduced that the sonic velocity of samples from the Tahorakuri formation and the Ngatamariki Intrusive Complex are primarily controlled by the density and porosity with potential influence from the microstructural property.

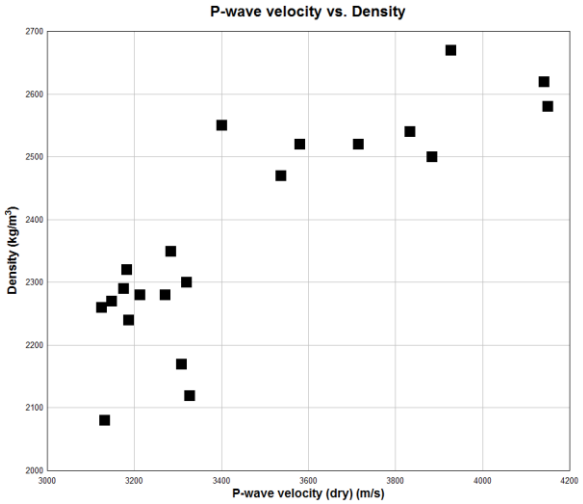

Figure 4.20 P-wave velocity vs. dry density

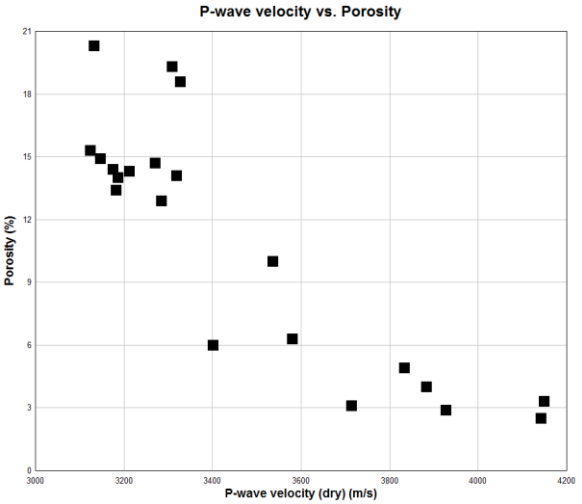

Figure 4.21 P-wave velocity vs. porosity

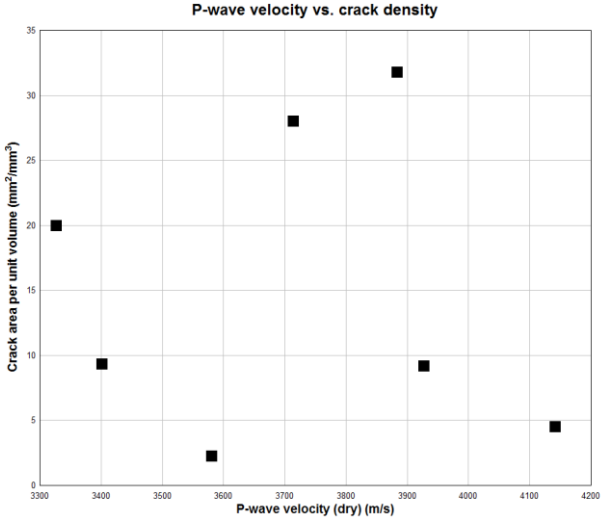

Figure 4.22 P-wave velocity vs. crack density

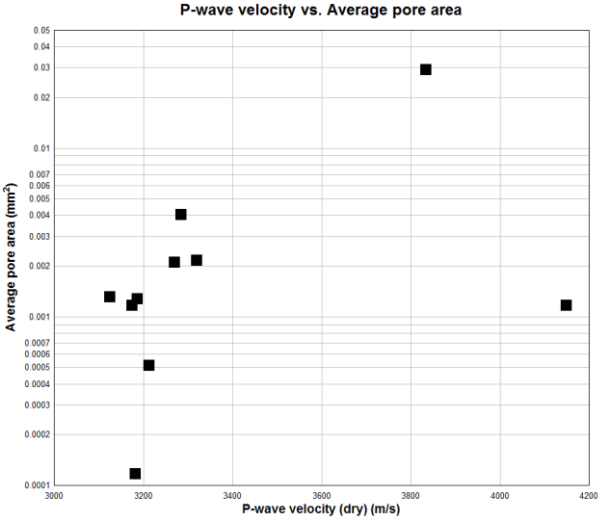

Figure 4.23 P-wave velocity vs. average pore area

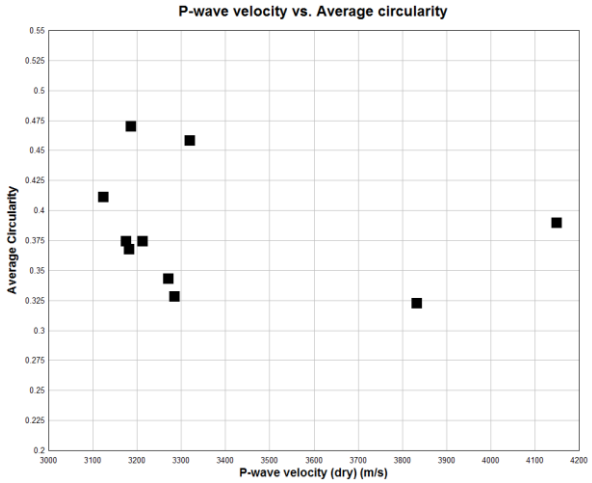

Figure 4.24 P-wave velocity vs. average circularity

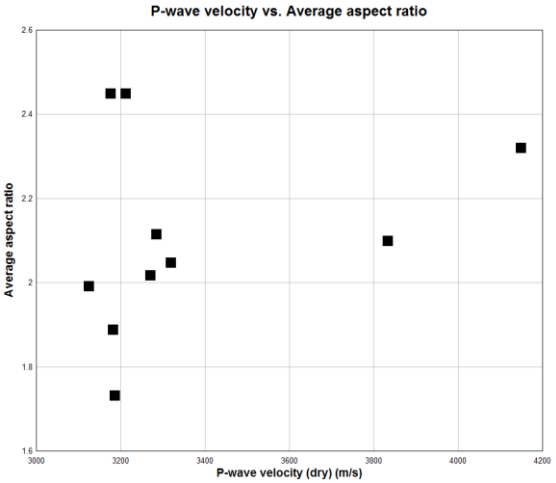

Figure 4.25 P-wave velocity aspect ratio

4.2.7 Permeability

Using the methods outlined in Section 2.5 the lithostatic pressure for each sample was calculated using the data from this and many other projects. The calculated lithostatic pressures take into account the depth of the samples as well as the variability in unit thickness across the field. The results were used to ascertain which confining pressure was appropriate to represent the in-situ lithostatic pressure. It is then possible to observe the effect of burial diagenesis on permeability at Ngatamariki.

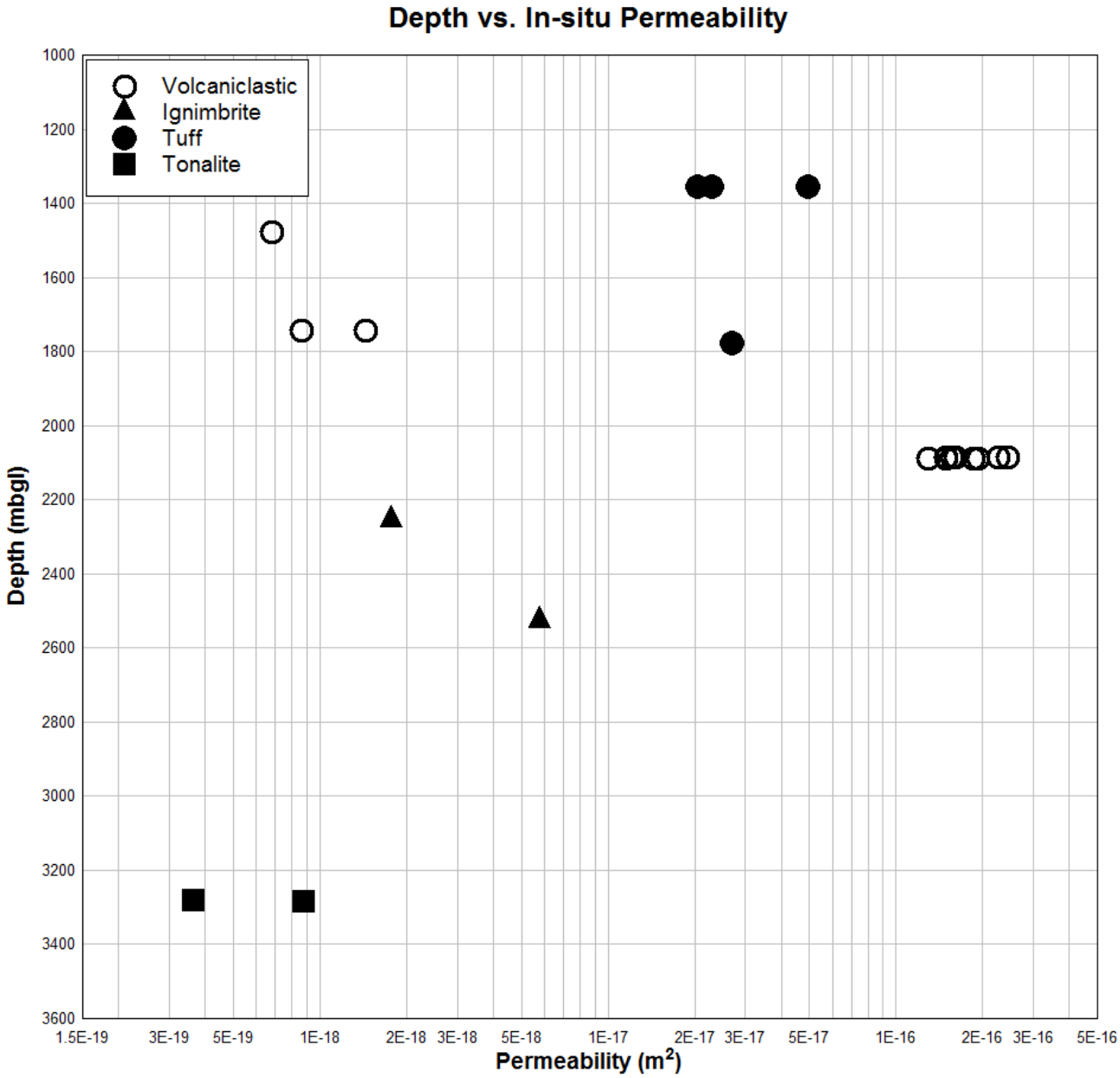

Figure 4.26 shows the in-situ matrix permeability plotted against depth. It can be seen that there are large fluctuations in permeability with depth. When all lithologies are considered, a trend of decreasing permeability with depth can be observed with several large fluctuations. However, when each lithology is inspected on its own, only the primary tuff shows a decrease in permeability with depth. The tonalite of the Ngatamariki Intrusive Complex has the lowest permeability when corrected for lithostatic pressure. Within the Tahorakuri Formation the volcaniclastic samples have both the highest and lowest permeability. It can be seen that most lithologies show relatively good grouping, however the volcaniclastic samples have two distinct clusters with the shallower samples having a lower permeability than the deeper samples.

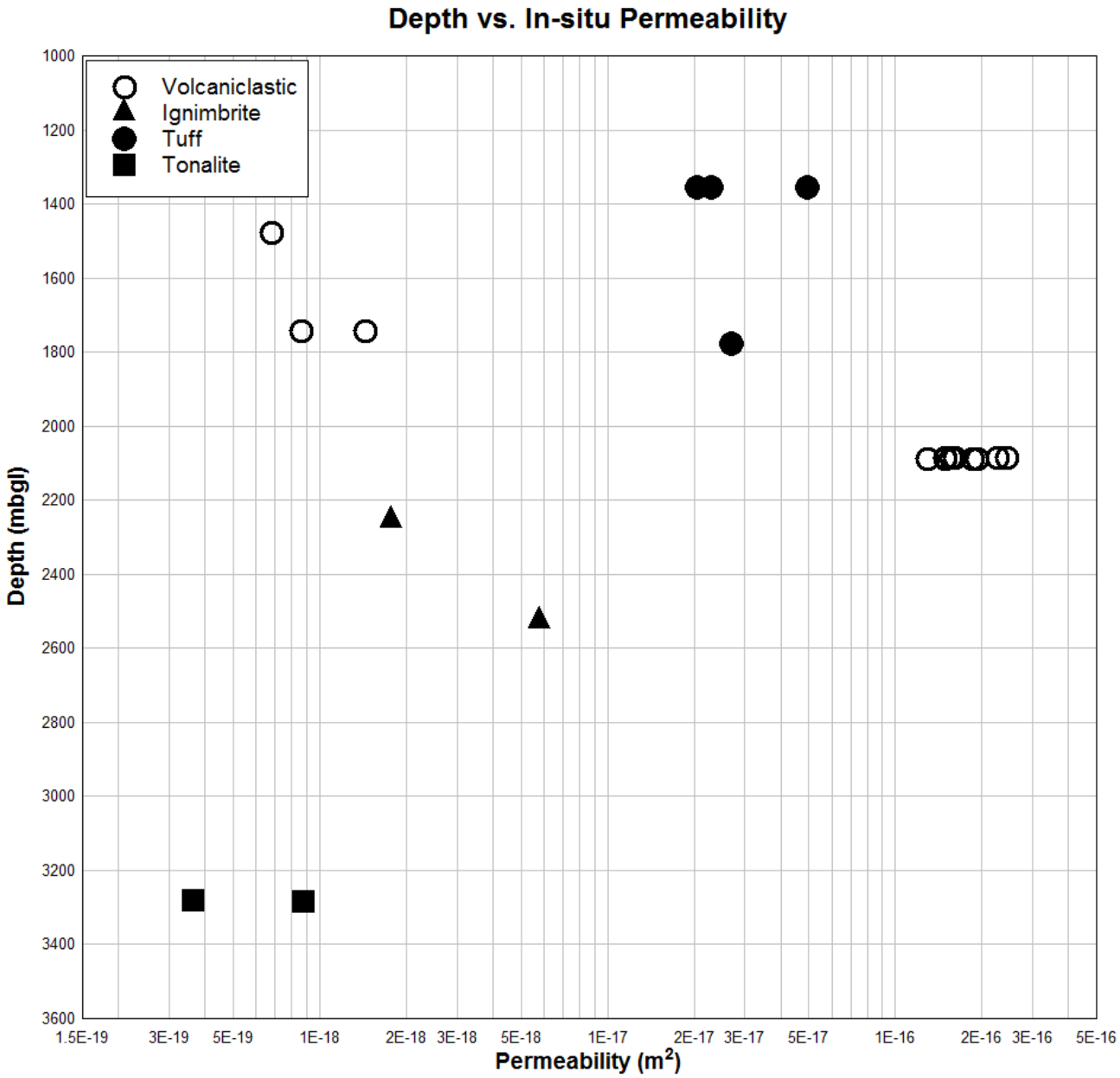

Figure 4.26 Depth vs. Permeability corrected for lithostatic pressure with lithologies identified. No clear correlation between permeability and depth, however trend of decreasing permeability with depth with large fluctuations.

4.2.8 Lithology Correction

The relationship between depth and the physical and mechanical properties within the Tahorakuri Formation does not define a clear trend, suggesting that there are other factors influencing on physical properties besides depth. The Tahorakuri Formation has a large variability in both the primary lithology as well as secondary alteration and mineralization. The samples that were tested can be broken down into four main lithologies as described in Section 3.2. These are: primary tuff, volcaniclastic units, ignimbrite and the intrusive tonalite. Figure 4.27 shows the physical properties from the Tahorakuri Formation plotted against depth with colour coded lithologies (note that the values plotted are averaged from the test results). With the lithologies identified, visible groupings of physical properties within each lithology become apparent. For example the Ignimbrites have a relatively low permeability, fast sonic wave velocity, low porosity and high density. The variations in lithology has resulted in large fluctuation within the physical and mechanical properties with depth. This has made identifying large scale burial diagenesis trends within the Tahorakuri Formation difficult. It appears that lithology plays a larger role in controlling the physical and mechanical properties than burial diagenesis. It is possible to look at each individual lithology within the Tahorakuri Formation and observe the change in physical properties with depth. However, due to limited data and complex post deposition alteration and mineralization, it is difficult to isolate the effects burial diagenesis. Below is a description of the changes in in mechanical properties within each lithology with depth:

Primary Tuff: Two depth data points exist. With increasing depth there is decreasing permeability, porosity and increasing density, and sonic velocity.

Volcaniclastic: Three depth data points exist. With increasing depth there is decreasing density, sonic velocity and increasing permeability and porosity.

Ignimbrite: Two depth data points exist. With increasing depth there is decreasing porosity and increasing density, sonic velocity and permeability.

Tonalite: Only one depth data point exists therefore, no trends with depth can be ascertained.

Of all three lithology types only the primary tuff displays the typical characteristics of burial diagenesis The Ignimbrites show density, porosity and sonic velocity results that would be expected from burial diagenesis however the permeability increases with depth. The volcaniclastic samples display characteristics that are the opposite of what would be expected of burial diagenesis.

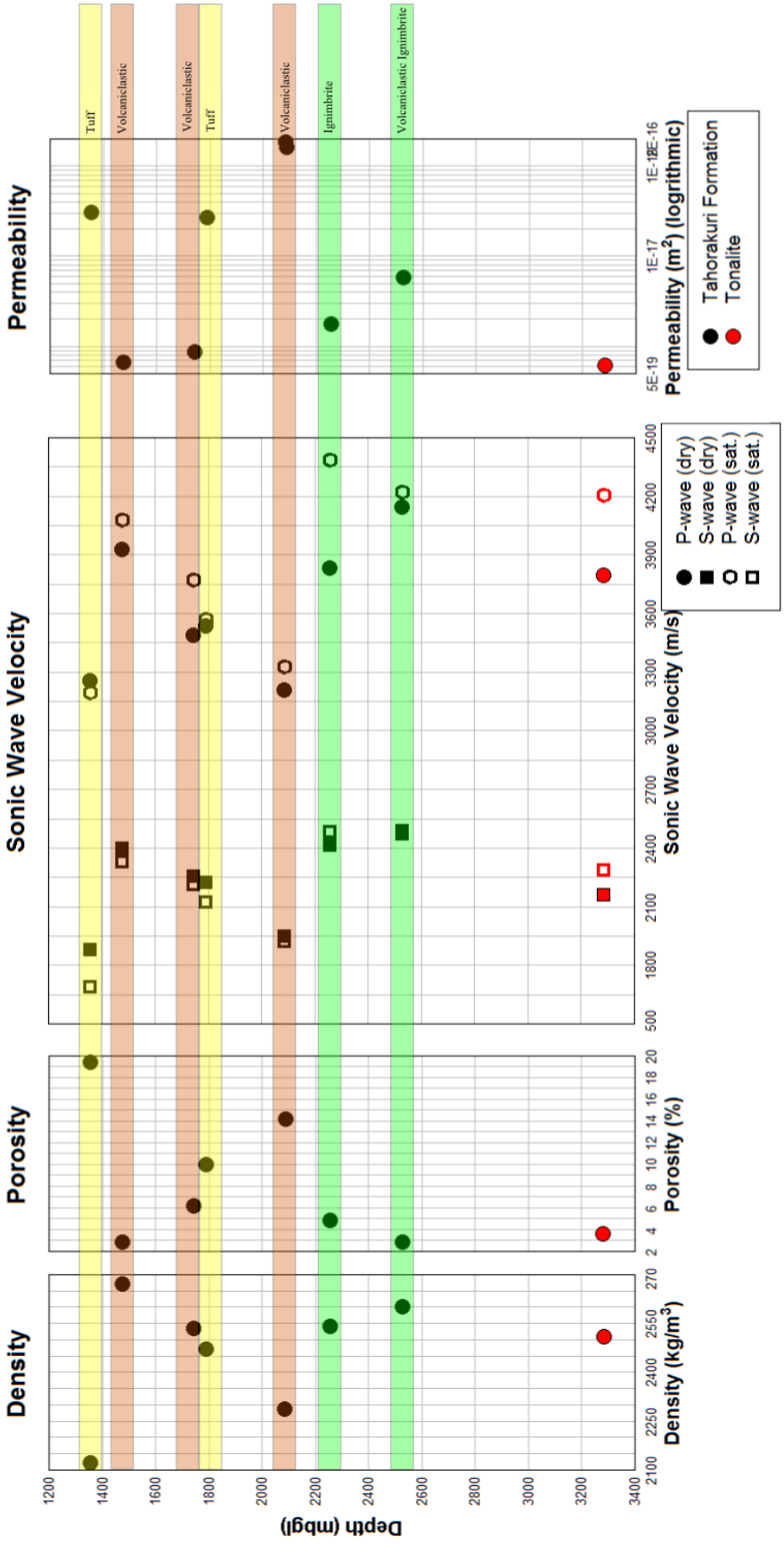

Figure 4.27 Mechanical properties of the Tahorakuri Formation with depth. Colour coding of different lithologies that were tested within the Tahorakuri

4.2.9 Comparison to burial diagenesis in other geothermal fields

4.2.9.1 Tiwi Geothermal field, Philippines

When compared to the Tiwi geothermal field in the Philippines, the Tahorakuri Formation shares several similarities while also have several points of difference. Both contain a trend of decreasing porosity with depth with several large fluctuations in porosity. Both Stimac et al. (2004) and this thesis attribute a large portion of the variation observed to changes in lithology. However, the lithological changes at Tiwi are much greater than at Ngatamariki as the Tiwi Geothermal field comprises of andesite, breccia, conglomerate, paleosol and sandstone units. The characteristics and mechanical properties of these lithologies are vastly difference and therefore a large range in porosity is expected. While the Ngatamariki Geothermal Field has a large range of lithologies, this project focuses on one formation in which primary tuff, volcaniclastic units and ignimbrite were observed. These rock types share a similar source and have only minor differences in mineralogy and method of emplacement yet there is a similar range in porosity to that observe at the Tiwi geothermal field. In fact over a similar depth range the Ngatamariki geothermal field has a much larger variation in porosity and permeability. Porosity vs depth was plotted for each lithological unit at Tiwi with linear regression trends applied. Each lithology show a decrease in porosity with depth. There was a large amount of scatter within these trends with correlation coefficients ranging from R^2 0.12-0.54, displaying the large variation of physical properties within each lithology. At Ngatamariki the primary tuff and the ignimbrite samples showed a trend of decreasing porosity with depth (note not enough samples to provide perform a regression trend line). However the volcaniclastic samples showed a trend of increasing porosity with depth. This trend within the volcaniclastic has been attributed to variations in the primary texture. Overall Tiwi and Ngatamariki appear similar, with a range of lithological units that cause large fluctuations within the physical properties with depth. An overall trend of decreasing porosity and permeability with depth was observed at both fields.

4.2.9.2 Salton Sea

Samples from Salton Sea showed a trend of calcite being replaced by epidote with increase depth/geothermal fluid temperature. This was also observed at Ngatamariki with primary tuff and volcaniclastic samples showing increased epidote and decreased calcite with depth. The samples at Salton Sea consisted of sandstone siltstone and shales. A trend of decreased porosity with increased depth was observed in the samples from Salton Sea. This trend was observable through the different lithology types. When compared to the Salton Sea, Ngatamariki has much larger porosity fluctuations.

4.2.10 Summary of burial diagenesis

The effects of broad scale burial diagenesis at Ngatamariki was investigated with testing of physical and mechanical properties. The results show a trend of increasing density, ultrasonic velocity and decreasing porosity, permeability with depth. While a trend could be observed no clear correlation between these properties and depth could be established. The Tahorakuri Formation is defined as a volcaniclastic and sedimentary deposit between the Whakamaru group ignimbrites and the greywacke basement (Coutts 2013) that was deposited over 1.22Ma (Eastwood 2013). It is comprised of thick sequences of sediments, lithic tuff, breccias and welded quartz-poor Ignimbrite. As the unit consists of several different lithologies correlating changes in physical properties with depth is difficult as each of these lithologies has different mechanical properties relating to their depositional mechanism. Within the broad lithologies large variations in rock characteristics were observed. This was most prevalent in the volcaniclastic units, having densities ranging from 2287 to 2670 kg/m^3 and porosities ranging from 3 to 14%. There was also differences in the microstructure with some volcaniclastic samples displaying microfractured pore structure while others showed a vesicular pore structure.

Exposure of a rock to high temperature geothermal fluids also modifies the physical properties through alteration, replacement and dissolution. Ngatamariki has thermal gradient where temperature increases with depth around a central “hot spot”. As the temperature increases with depth changes associated with the geothermal fluids could easily be mistaken for the effects of burial diagenesis. As the samples were taken from a range of depth the temperature of the hydrothermal fluid in which they were exposed varies. Petrophysical analysis of the thin sections showed mineralization of veins with geothermal minerals like calcite and epidote, resulting in a

reduction in porosity and permeability. Vesicles were observed in the thin sections however the origin (depositional or hydrothermal) is unknown.

The contribution of variations in lithology coupled with the complex post depositional environment has resulted in an extremely complex system. This makes distinguishing the effects of burial diagenesis difficult. A trend of decreasing porosity and permeability with increasing sonic velocity and density was observed with large fluctuations. These fluctuations have been attributed to the variations in lithology, microstructure and alteration. Other studies of burial diagenesis in geothermal systems have observed similar changes in mechanical properties with depth (Tewhey 1977; Stimac et al. 2004; Mielke 2009; Dillinger et al. 2014).

4.3 Further development of geothermal resource

This study has observed the effects of burial diagenesis within the Tahorakuri formation, with decreasing porosity and permeability and increasing density and sonic velocity with increased depth. However, large variations in these mechanical properties with depth were observed with the highest porosity and permeability values recorded at 2083 - 2087 mbgl. Other studies in geothermal fields have found similar results with Stimac et al. (2004) also observing large variations in porosity that depth was attributed to the changes in lithology observed. Stimac et al. (2004) observed variations in porosity to be ~2-3 % with an average of 5% for samples found below 2000 mbgl. In this study samples below 2000 mbgl have a similar average porosity value however there is a much larger variation in porosity with the largest porosity below 2000 mbgl being 19.2% and lowest being 2.5%. This indicates that burial diagenesis is not the primary control on permeability and porosity. Results from this project indicate that variations in primary texture and lithology are the likely cause of the observed fluctuations in mechanical properties.

In this study it is assumed that the two mechanical properties of interest for potential for further development and deep drilling (>3 km) is the porosity and permeability.

Figure 4.27 show the variation in permeability and porosity with depth. It is observed that the lithology largely dictates the porosity and permeability however, the volcaniclastic samples display a large range of both porosity and permeability. Another factor is the effect of increased lithostatic load on these mechanical properties. Figure 4.9 and Figure 4.10 in section 4.1.3 show the effect of changing confining pressure on permeability. Increased confining pressure associated with lithostatic stress has the potential to reduce porosity and permeability. It was observed that an increase in confining pressure resulted in a large decrease in permeability for samples with pore structure dominated by microfractures. Samples that contained a vesicular pore structure showed only a minor decrease in permeability with increased confining pressure. The distribution of these pore structures appear to be controlled by lithology and appear at a range of depths.

At Ngatamariki the effect of burial diagenesis is minor and high permeability and porosity exist at depths of 2500 -3000 mbgl. These factor warrant further development of the geothermal resource.

5 Conclusions

The Ngatamariki Geothermal Field is the site of New Zealand's newest geothermal power station. An understanding of the reservoir rock's physical properties will provide optimisation of the high temperature fluid extraction and therefore increased efficiency. The objective of this project was to measure the intact physical and mechanical properties of a range of reservoir rock. In particular matrix permeability measurements were made of intact rock using a permeameter, over a range of confining pressures. As the samples were extracted from a range of depths it was possible to perform permeability testing at confining pressures representative of the in-situ pressure conditions from which they were extracted. Microstructural analysis was performed in conjunction with the physical testing to allow comparisons between the physical properties and the microstructural textures, mineralogy and pore structure. This was performed to gain an understanding of the relationship between microstructure and the observed physical properties. From this four main conclusions have been made:

- The physical properties of the tested samples appear to be controlled by the broad lithological units observed. Minor variations within the physical properties are attributed to variations in lithostatic stress and hydrothermal alteration. However, the volcaniclastic units show a large variation in porosity, density, sonic velocity, permeability and microstructure. This has been attributed to the volcaniclastic rocks having a large variation in composition with a range of pumice and lithic components and depositional processes resulting vastly different primary textures.

- No clear correlation exists between the quantitative microstructure analysis and permeability. Pore circularity showed a trend of increased circularity with increased permeability, however large variations within the data were observed and further testing is required to confirm the correlation. There is a correlation between connected porosity and

permeability, with a power law regression fit showing a correlation coefficient of 0.65. The microstructural analysis also identified a relationship between microfractured samples and low porosity (<12%) and permeability, with vesicular samples correlated with high porosity (>12%) and permeability.

- Samples displaying a microfractured pore structure showed progressively lower permeability with increased confining pressure when compared to samples with a vesicular microstructure. The decrease in permeability of the microfractured samples remains relatively constant with the increased confining pressure. The samples displaying vesicular pore structure show a smaller decrease in permeability with increase confining pressure, with the largest decrease occurring between 5 and 15MPa. Further increases in confining pressure had only a minor effect on the permeability. This suggests that samples displaying vesicular pore structure do not experience a notable decrease in permeability with increased confining pressure. The variation in the pore structure of Tahorakuri Formation may be due to variations in depositional environments. Sediments buried at the margins of paleo-basins, may have compacted slowly resulting in more spherical pores. This may result in areas of greater matrix permeability at paleo-basin margins.

- The effects of burial diagenesis was observed in the physical properties of the tested samples at Ngatamariki. However, the observed changes in the physical and mechanical properties showed large variations that correlate with the variation in lithology. The effect of hydrothermal alteration was also observed in thin section as the cementation of microfractures and filling of void spaces within the rocks. The large variation in the physical and mechanical properties with depth suggests that lithology, and hydrothermal alteration also play a large role in controlling the physical and mechanical properties of the reservoir rocks.

- The results of this project show potential for further development of the geothermal resource, with high porosity and permeability observed within the Tahorakuri Formation at depth. The effect of burial diagenesis while observable does not appear to be the controlling factor of the physical properties with depth. Two key lithologies, the primary

tuff and volcaniclastic units were identified as they displayed high porosity and permeability values. These units also show little decrease in permeability with increased confining pressure and therefore could provide both porosity and permeability at great depth (>3,000 m). These factor warrant further development of the geothermal resource.

5.1 Further research directions

A study of the Tahorakuri Formation at Rotokawa would provide a great comparison of the spatial variability of the physical and mechanical properties of the unit.

Another interesting study would be to analyse the sample of this study using tomography to gain a complete understand the pore structure, its variability and effect on permeability. This could be compared to the fluorescent dye analysis performed in this thesis to provide a review of the effectiveness of this methodology in the heterogeneous samples.

6 References

Akinyemi OD, Alabi AA, Ojo AI, Adewusi OE 2012. Characterization of Density and Porosity of Rocks Samples from Ogun State of Nigeria. Earth Science Research 1(2).

Barton N 2007. Rock quality, seismic velocity, attenuation and anisotropy. New York; London, Taylor & Francis.

Bernabe Y 1986. The effective pressure law for permeability in Chelmsford granite and Barre granite. International Journal of Rock Mechanics and Mining Sciences & Geomechanics Abstracts 23(3): 267-275.

Bertrand EA, Caldwell TG, Hill GJ, Bennie SL, Soengkono S 2013. Magnetotelluric imaging of the Ohaaki geothermal system, New Zealand: Implications for locating basement permeability. Journal of Volcanology and Geothermal Research 268: 36-45.

Bibby HM, Bennie SL, Stagpoole VM, Caldwell TG 1994. Resistivity structure of the Waimangu, Waiotapu, Waikite and Reporoa geothermal areas, New Zealand. Geothermics 23(5–6): 445-471.

Bibby HM, Caldwell TG, Davey FJ, Webb TH 1995. Geophysical evidence on the structure of the Taupo Volcanic Zone and its hydrothermal circulation. Journal of Volcanology and Geothermal Research 68(1–3): 29-58.

Bignall G 2009. Ngatamariki Geothermal Field Geoscience Overview. GNS Science Consultancy Report 2009/94 41p.

Boseley C, Bignall G, Rae AJ, Chambefort I, Lewis B 2012. Stratigraphy and hydrothermal alteration encountered by monitor wells completed at Ngatamariki and Orakei Korako in 2011. Stratigraphy and hydrothermal alteration encountered by monitor wells completed at Ngatamariki and Orakei Korako in 2011.

Boseley CC, William; Urzua-Monsalve, Luis; Powell, Tom; Grant, Malcolm 2010. A resource conceptual model for the Ngatamariki Geothermal Field based on recent exploration well drilling and 3D MT resistivity imaging. World Geothermal Congress 2010: 1146.

Bourbie T, Zinszner B 1985. Hydraulic and acoustic properties as a function of porosity in Fontainebleau Sandstone. Journal of Geophysical Research 90(B13): 11-11,532.

Brace WF, Walsh JB, Frangos WT 1968. Permeability of Granite under High Pressure. Journal of Geophysical Research 73(6): 2225-2236.

Bromley CJ 2002. Putauaki (Kawerau) MT Resistivity Survey. New Zealand Geothermal Workshop.

Catherine Boseley WC, Luis Urzua-Monsalve, Tom Powell and Malcolm Grant 2010. A resource conceptual model for the Ngatamariki Geothermal Field based on recent exploration well drilling and 3D MT resistivity imaging. World Geothermal Congress 2010: 1146.

Chambefort I, Lewis B, Wilson CJN, Rae AJ, Coutts C, Bignall G, Ireland TR 2014. Stratigraphy and structure of the Ngatamariki geothermal system from new zircon U–Pb geochronology: Implications for Taupo Volcanic Zone evolution. Journal of Volcanology and Geothermal Research 274(0): 51-70.

Cole JW 1990. Structural control and origin of volcanism in the Taupo volcanic zone, New Zealand. Bulletin of Volcanology 52(6): 445-459.

Cole JW, Spinks KD 2009. Caldera volcanism and rift structure in the Taupo Volcanic Zone, New Zealand. Geological Society, London, Special Publications 327: 9-29.

Cook JE 2010. The physical, mechanical, and structural effects of diagenesis in siliciclastic rocks. PhD Thesis, University of Wilsconsin-Madison.

Coutts C 2013. 2013 Revision of Ngatamariki Stratigraphy (unpublished Mighty River Power Report).

Darby DJ, Hodgkinson KM, Blick GH 2000. Geodetic measurement of deformation in the Taupo volcanic zone, New Zealand; the North Taupo Network revisited. New Zealand Journal of Geology and Geophysics 43(2): 157-170.

David C, Darot M 1990. Permeability and conductivity of sandstones : Proc International Symposium on Rock at Great Depth, Pau, 28–31 August 1989 V1, P203–209. Publ Rotterdam: A A Balkema, 1989. International Journal of Rock Mechanics and Mining Sciences & Geomechanics Abstracts 27(3): A147.

Dillinger A, Huddlestone-Holmes CR, Zwingmann H, Ricard L, Esteban L 2014. Impacts of Diagenesis on Reservoir Quality in a Sedimentary Geothermal Play. Proceedings, Thirty-Ninth Workshop on Geothermal Reservoir Engineering, Stanford University, Stanford, California.

Eastwood AA 2013. The Tahorakuri Formation: Investigating the early evolution of the Taupo Volcanic Zone in buried volcanic rocks at Ngatamariki and Rotokawa geothermal fields. Masters Thesis, Departoment of Geological Sciences, University of Canterbury.

Glassley WE 2010. Subsurface Fluid Flow. Geothermal Energy, CRC Press. Pp. 51-67.

GNS 2014. GNS Science Annual Report. 4 p.

Grant MA 1982. Geothermal reservoir engineering. New York, Academic Press.

Gueguen Y, Placiauskas V 1994. Introduciton ot the Physics of Rocks. Princeton University Press, Princeton, New Jersey.

Guéguen Y, Palciauskas V 1994. Introduction to the Physics of Rocks. Princeton University Press, Princeton, New Jersey.

Heap MJ, Lavallee Y, Petrakova L, Baud P, Reuschle T, Varley NR, Dingwell DB 2014. Microstructural controls on the physical and mechanical properties of edifice-forming andesites at Volcan de Colima, Mexico. Journal of Geophysical Research: Solid Earth 119(B4): 2925-2963.

Heap MJ, Mollo S, Vinciguerra S, Lavallée Y, Hess KU, Dingwell DB, Baud P, Iezzi G 2013. Thermal weakening of the carbonate basement under Mt. Etna volcano (Italy): Implications for volcano instability. Journal of Volcanology and Geothermal Research 250(0): 42-60.

Heard HC, Page L 1982. Elastic moduli, thermal expansion, and inferred permeability of two granites to 350°C and 55 megapascals. Journal of Geophysical Research: Solid Earth 87(B11): 9340-9348.

Hochstein MP 1971. Seismic, Gravity and Magnetic Studies, Broadlands Geothermal Field, New Zealand. Geothermics 2(2): 333-346.

Houghton BF, Houghton BF, Wilson CJN, McWilliams MO, Lanphere MA 1995. Chronology and dynamics of a large silicic magmatic system: Central Taupo Volcanic Zone, New Zealand. Geology (Boulder) 23(1): 13.

Hunt TM, Whiteford CM 1979. Magnetic map of New Zealand 1:250,000; total force anomalies. Dep. Sci. Ind. Res., Wellington, New Zealand(1979)(8) Maps:colored geophysical surv. map; 1:250,000`.

Hurst AW, Bibby HM, Robinson R 2002. Earthquake focal mechanisms in the central Taupo volcanic zone and their relation to faulting and deformation. New Zealand Journal of Geology and Geophysics 45(4): 527-536.

Jafari A, Babadagli T 2011. Effective fracture network permeability of geothermal reservoirs. Geothermics 40(1): 25-38.

Keller WD, Valduga A 1946. The Natural Steam at Larderello, Italy. The Journal of Geology 54(5): 327-334.

Khandelwal M 2013. Correlating P-wave Velocity with the Physico-Mechanical Properties of Different Rocks. Pure and Applied Geophysics 170(4): 507-514.

Klinkenberg LJ 1941. The permeability of porous media to liquids and gases. API Drilling and Production Practice. American petroleum Institute, New York: 200–213.

Lane SJ, Gilbert JS 2008. Fluid Motions in Volcanic Conduits: A Source of Seismic and Acoustic Signals, Geological Society Publishing House.

Lewis DW, McConchie D 1994. Practical sedimentology 2nd edittion. Chapman & Hall, New York.

McIlreath IA, Morrow DW 1990. Diagenesis (Geoscience Canada repint series). Geological Association of Canada 4.

Mielke P 2009. Properties of the Reservoir Rocks in the Geothermal Field of Wairakei, New Zealand. PhD Thesis, Technische Universität Darmstadt.

Modriniak N, Studt FE 1959. Geological structure and volcanism of the Taupo-Tarawera district. New Zealand Journal of Geology and Geophysics 2(4): 654-684.

Murphy H, Huang C, Dash Z, Zyvoloski G, White A 2004. Semianalytical solutions for fluid flow in rock joints with pressure-dependent openings. Water Resources Research 40(12): W12506.

Nara Y, Meredith PG, Yoneda T, Kaneko K 2011. Influence of macro-fractures and micro-fractures on permeability and elastic wave velocities in basalt at elevated pressure. Tectonophysics 503(1–2): 52-59.

O'Brien J, Mroczek E, Boseley C 2011. Chemical structure of the Ngatamariki Geothermal Field, Taupo Volcanic Zone, NZ. Proceedings of the New Zealand Geothermal Workshop 33.

Olalla C, Hernandez LE, Rodriguez-Losada JA, Perucho Á, González-Gallego J 2010. Volcanic Rock Mechanics: Rock Mechanics and Geo-engineering in Volcanic Environments, CRC Press.

Palmer AS 1982. Kawakawa Tephra in Wairarapa, New Zealand, and its use for correlating Ohakea loess. New Zealand Journal of Geology and Geophysics 25(3): 305-315.

Pellant C, Taylor H 2000. Rocks and Minerals, Dorling Kindersley.

Rahmouni A, Boulanouar A, Boukalouch M, Géraud Y, Samaouali A, Harnafi M, Sebbani J 2013. Prediction of Porosity and Density of Calcarenite Rocks from P-Wave Velocity Measurements. International Journal of Geosciences 4(9): 1292 - 1299.

Read SAL, Barker PR, Reyes AG 2001. Consolidation Proerties of Huka Falls Formations - Linkages to Subsidence at Ohaaki and Wairakei. proceedings 23rd NZ Geothermal Workshop.

Reyes AG 1990. Petrology of Philippine geothermal systems and the application of alteration mineralogy to their assessment. Journal of Volcanology and Geothermal Research 43(1-4): 279-309.

Reyners M, Eberhart-Phillips D, Stuart G, Nishimura Y 2006. Imaging subduction from the trench to 300 km depth beneath the central North Island, New Zealand, with Vp and Vp/Vs. Geophysical Journal International 165(2): 565-583.

Rust AC, Cashman KV 2004. Permeability of vesicular silicic magma: inertial and hysteresis effects. Earth and Planetary Science Letters 228(1–2): 93-107.

Saar MO, Manga M 1999. Permeability-porosity relationship in vesicular basalts. Geophysical Research Letters 26(1): 111-114.

Siratovich PA 2014. Thermal stimulation of the Rotokawa andesite: a laboratory approach. PhD Thesis, College of Science, Department of Geological Sciences, University of Canterbury, Christchurch.

Siratovich PA, Heap MJ, Villeneuve MC, Cole JW, Reuschlé T 2014. Physical property relationships of the Rotokawa Andesite, a significant geothermal reservoir rock in the Taupo Volcanic Zone, New Zealand. Geothermal Energy 2:10.

Spinks KD, Acocella V, Cole JW, Bassett KN 2005. Structural control of volcanism and caldera development in the transtensional Taupo Volcanic Zone, New Zealand. Journal of Volcanology and Geothermal Research 144(1–4): 7-22.

Stimac JA, Powell TS, Golla GU 2004. Porosity and permeability of the Tiwi geothermal field, Philippines, based on continuous and spot core measurements. Geothermics 33(1–2): 87-107.

Tewhey JD 1977. Geologic characteristics of a portion of the Salton Sea geothermal field, Geothermal Resour. Counc., Davis, Calif.

Ulusay R, Hudson JA 2007. The complete ISRM suggested methods for rock characterization, testing and monitoring : 1974-2006 / editors, Resat Ulusay, and John A. Hudson. Commission on Testing Methods, International Society of Rock Mechanics, IRSM Turkish National Group, Ankara.

Underwood EE 1969. Stereology, or the quantitative evaluation of microstructures. Journal of microscopy 89(2): 161-180.

Vasconcelos G, Lourenço PB, Alves CAS, Pamplona J 2008. Ultrasonic evaluation of the physical and mechanical properties of granites. Ultrasonics 48(5): 453-466.

Vutukuri VS, Lama RD 1940. Handbook on mechanical properties of rocks : testing techniques and results II, Clausthal ; Bay Village, Ohio.

Watson A 2013. Geothermal Engineering : Fundamentals and Applications. 1 ed. Dordrecht, Springer.

Wilson CJN, Houghton BF, McWilliams MO, Lanphere MA, Weaver SD, Briggs RM 1995. Volcanic and structural evolution of Taupo Volcanic Zone, New Zealand: a review. Journal of Volcanology and Geothermal Research 68(1–3): 1-28.

Wu XY, Baud P, Wong T-f 2000. Micromechanics of compressive failure and spatial evolution of anisotropic damage in Darley Dale sandstone. International Journal of Rock Mechanics and Mining Sciences 37(1): 143-160.

Wyering LD, Villeneuve MC, Wallis IC, Siratovich PA, Kennedy BM, Gravley DM, Cant JL 2014. Mechanical and physical properties of hydrothermally altered rocks, Taupo Volcanic Zone, New Zealand. Journal of Volcanology and Geothermal Research 288(0): 76-93.

7 Appendix

7.1 Sample descriptions

NM2 1788mbgl

Well: NM2	Unit: Tahorakuri Formation
Depth: 1788mbgl	Lithology: Tuff?
Associated thin sections: ts9	Sample Names: NM2 1788 A

Sample Description:

The groundmass consists of a creamy green with dark green speckles. Visible lithic fragments ranging from sub-rounded to sub-angular. Lithics are generally green in colour however grey and white lithic are also present. Some lithic fragments appear to be pumiceous.

Thin section

Crystal rich thin section with 70% crystals 30% crypto crystalline matrix. Highly altered with large amounts of resorption within the plagioclase phenocrysts. Chlorite crystals appear highly altered. Large mafic minerals likely chlorite and epidote, likely a tuff.

Minerals present	**Abundance**
Chlorite	Trace
Epidote	Minor
Plagioclase	Minor
Quartz	Minor
Opaques	Trace
Major = 51-100%, Minor = 10-50%, Trace = <5%	

Photos

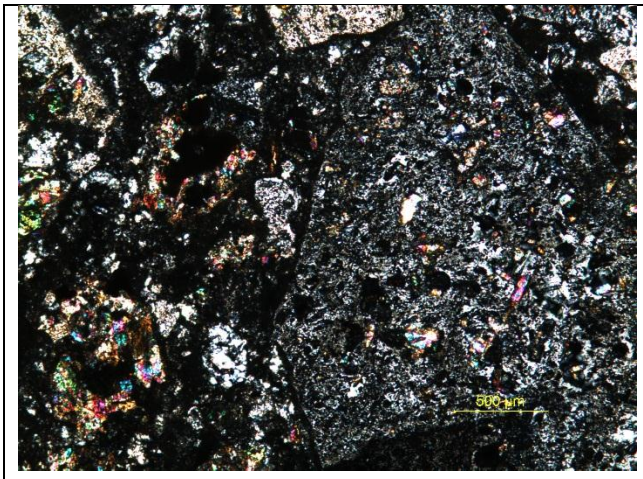

Highly altered and resorbed feldspar (right) groundmass (left)

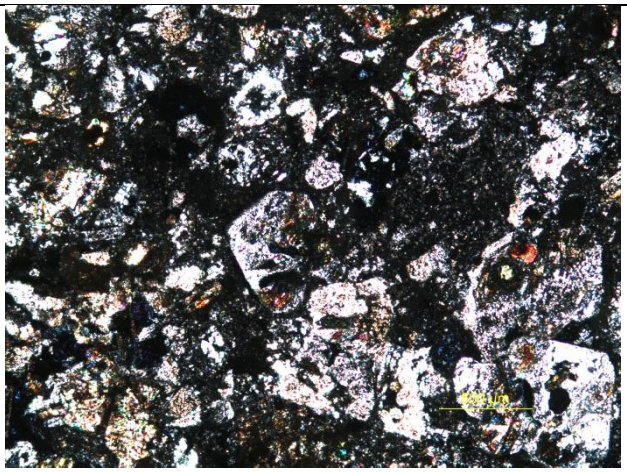

Typical groundmass, note the rounding of the crystals

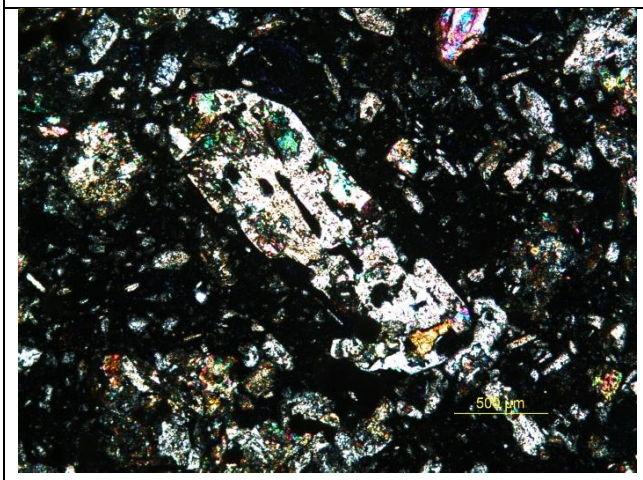

Resorbed feldspar with epidote crystals within the phenocryst

NM2 2254.7mbgl

Well :NM2	Unit: Tahorakuri Formation
Depth: 2254.7mbgl	Lithology: Ignimbrite?
Associated thin sections: TS4	Sample Names: NM2 2254.7 A

Sample Description:

The supplied sample has a light grey groundmass with visible lithic fragments (<2mm). The matrix is to fine to observe with the naked eyes.

Thin section

The groundmass consists of quartz and plagioclase cryptocrystalline matrix. Large quartz and plagioclase phenocrysts up to 2mm in size, with the quartz phenocrysts being fractured. Both Quartz and feldspar phenocrysts exist as sub-rounded and angular. Likely an ignimbrite.

Minerals present	**Abundance**
Quartz	Major
Plagioclase	Minor
Opaques	Minor-Trace
Major = 51-100%, Minor = 10-50%, Trace = <5%	

Photos

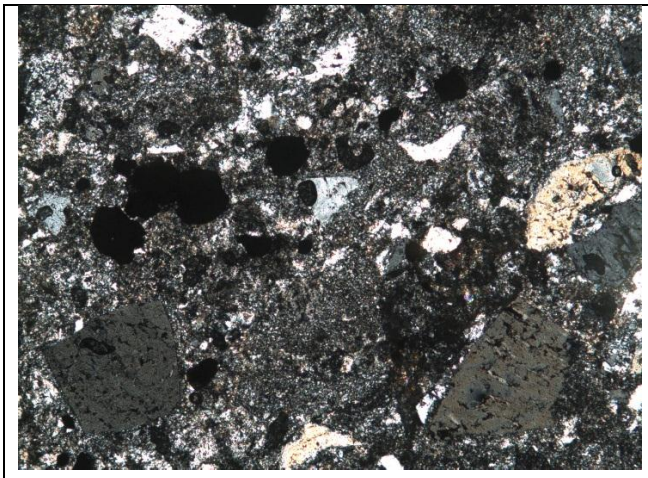

Typical groundmass, cross polarised light

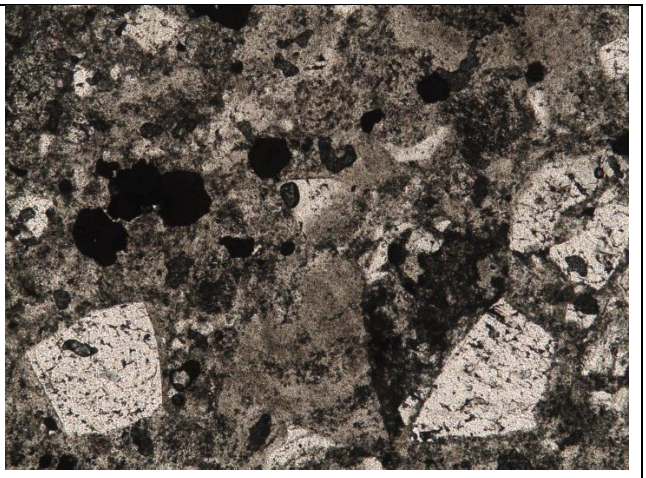

Typical groundmass in plain polarised light, with visible opaques

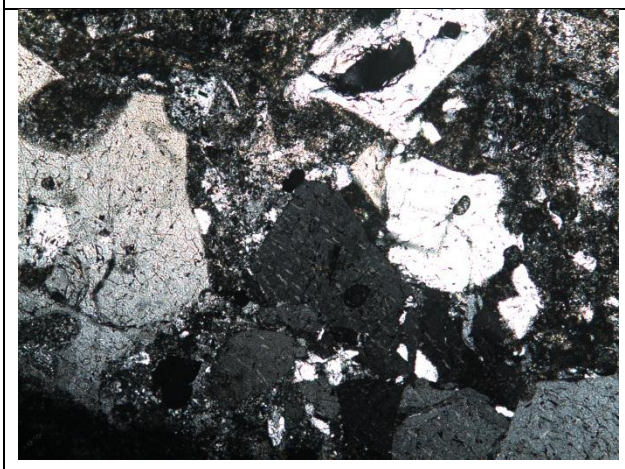

Large quartz crystals within groundmass

NM8a 2525.5m

Well: NM8a	Unit: Tahorakuri Formation
Depth: 2525.5 mbgl	Lithology: Volcaniclastic Ignimbrite
Associated thin sections: TS2, TS12	Sample Names: NM8a 2525.5 B,C

Sample Description:

The majority of the core consist of a light-dark greenish grey, hard, with visible volcaniclastic crystals. The rock is reatively hard and has several visible veins

Thin section

The majority of the sample consists of an altered groundmass with sparse lithic fragments. The groundmass consists of a crypto-crystalline quartz matrix, suggesting that the sample is an ignimbrite. Large angular to sub angular interlocking quartz crystals through the thin section suggest a volcaniclastic nature. Quartz veining is visible in the hand sample along with veins present in both of the thin sections. The quartz veins along with radial epidote suggest secondary alteration and recrystallization. Plagioclase crystals have been altered with some showing pitting. Displacement along fractures within quartz crystals suggest a change in stress environment since emplacement.

Minerals present	**Abundance**
Quartz	Major
Plagioclase Feldspar	Trace
Calcite	Trace
Chlorite	Trace
Epidote	Trace
Opaques	Trace
Major = 51-100%, Minor = 10-50%, Trace = <10%	

Photos

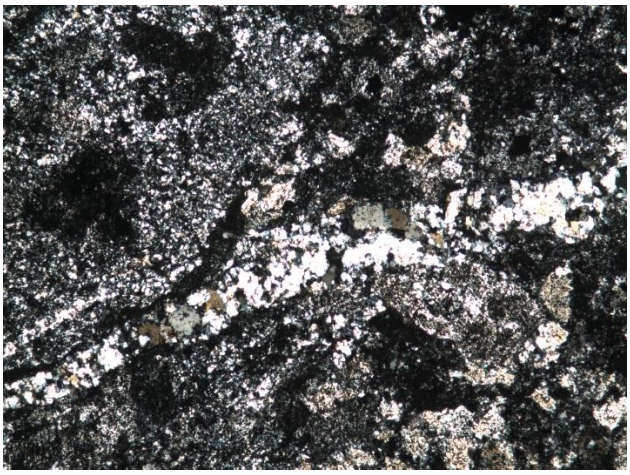

Quartz veining throughout groundmass of thin section

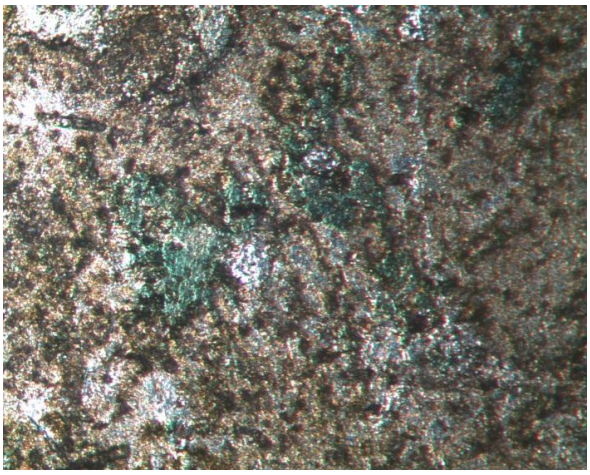

Chlorite crystal inside calcite crystal in plain polarised light

Large quartz crystal with obvious fracture displacement

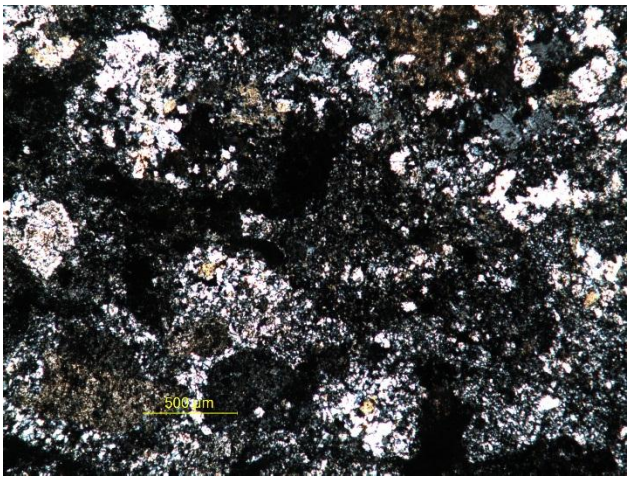

Typical groundmass

NM11 2083-2083.34m

Well: NM11	Unit: Tahorakuri Formation
Depth: 2083.0 – 2083.34mbgl	Lithology: Volcanoclastic Lithic Tuff
Associated thin sections: TS1,TS5,TS10, TS6	Associated samples: NM11 2083 A,B,C, NM11 2083.34 A,B

Sample Description:

The matrix of the core is a greeny grey with white grey and green phenocrysts. No apparent bedding can be seen within the sample. The core had one vertical fracture through the length of the core (which was avoided when samples were taken). Pumice clasts sizes vary from approximately 60mm to <1mm. The larger pumice lithics appear to be highly altered.

Thin section

The ground mass consists of small interlocking quartz and feldspar crystals commonly referred to as crypto crystalline groundmass. This groundmass is a silicified tuff matrix. Within the matrix there are many sub-rounded to rounded volcanoclastic lithic fragments that. There are many signs of secondary mineralisation and recrystallizations. Micro spherulites structures, radial epidote and sieve textures within plagioclase crystals show recrystallization has occurred post deposition.

Minerals present	**Abundance**
Quartz	Major-Minor
Plagioclase	Minor
Epidote	Minor-Trace
Chlorite	Minor-Trace
Calcite	Trace
Anhydrate	Trace
Opaques	Trace
Major = 51-100%, Minor = 10-50%, Trace = <5%	

Photos

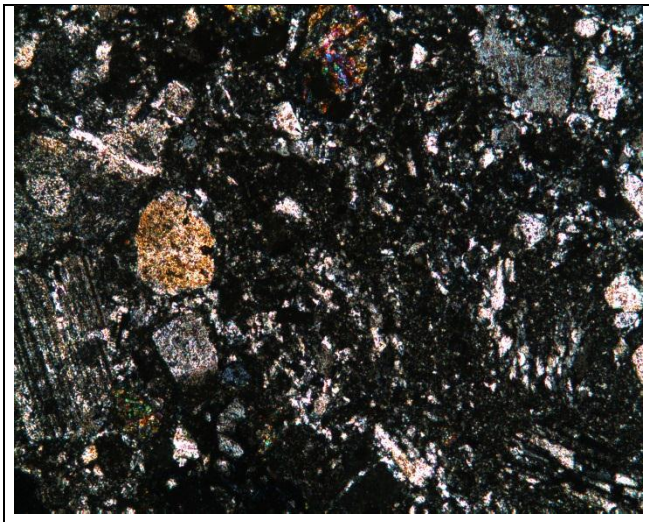

Typical groundmass with feldspar, epidote crystals in a crypto crystalline quartz feldspar matrix

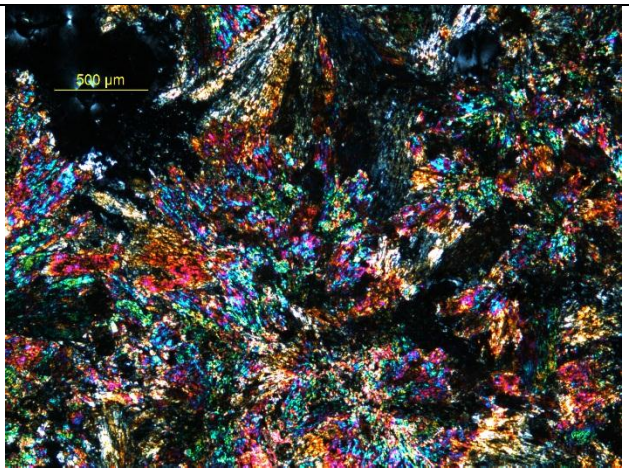

Radial epidote, commonly replacing pumice structures

Volcanoclastic lithic fragments found within the groundmass

NM11 2087.4mbgl

Well: NM11	Unit: Tahorakuri Formation
Depth: 2087.4 mbgl	Lithology: Volcanoclastic lithic tuff
Associated thin sections: TS8,11,3,7	Associated samples: NM11 2087.4 A,B,C,D

Sample Description:

The matrix of the core is a greeny grey with white grey, green and dark green phenocrysts. No apparent bedding can be seen within the sample. Pumice clasts sizes vary from approximately 60mm to <1mm. The larger pumice lithics appear to have altered to epidote with few several pumice clasts appear to be unaltered.

Thin section

The ground mass consists of small interlocking quartz and feldspar crystals commonly referred to as crypto crystalline groundmass. Within the matrix there are many sub-rounded to rounded volcanoclastic lithic fragments, this suggest that the particles have been reworked leading to the lithological description volcanoclastic lithic tuff. There are many signs of secondary mineralisation and recrystallizations. Micro spherulites structures, radial epidote and slieve textures within plagioclase crystals show recrystallization has occurred post deposition. Plagioclase crystals have partial dissolution with what appears to be epidote recrystallized within the plagioclase crystals. It also appears that epidote veins have formed within some of the samples. Dark blue blobs observed in plain polarized and cross polarized light are likely clay minerals.

Minerals present	**Abundance**
Quartz	Major-Minor
Epidote	Minor
Plagioclase	Minor
Opaques/clay	Trace
Anhydrite?	Trace
Chlorite	Minor-Trace
Major = 51-100%, Minor = 10-50%, Trace = <5%	

Photos

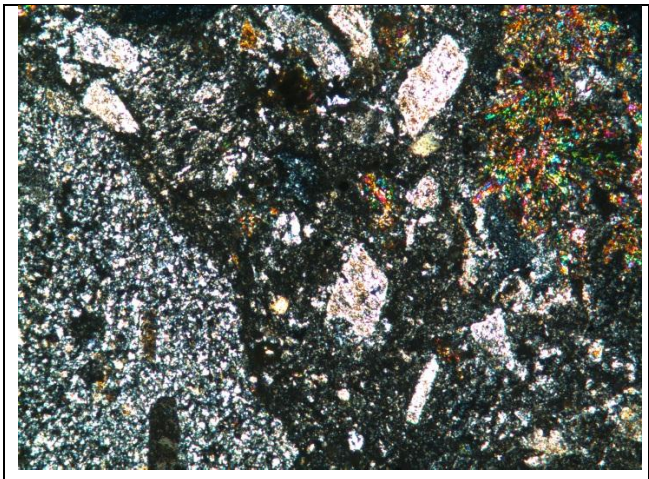

Typical ground mass (centre) with Epidote crystal (right) and part of a large volcanoclastic lithic fragment (right)

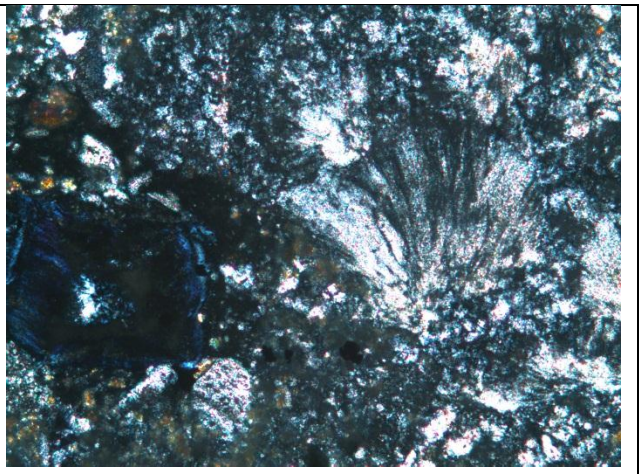

Devitrified glass (right) with a chlorite crystal (left)

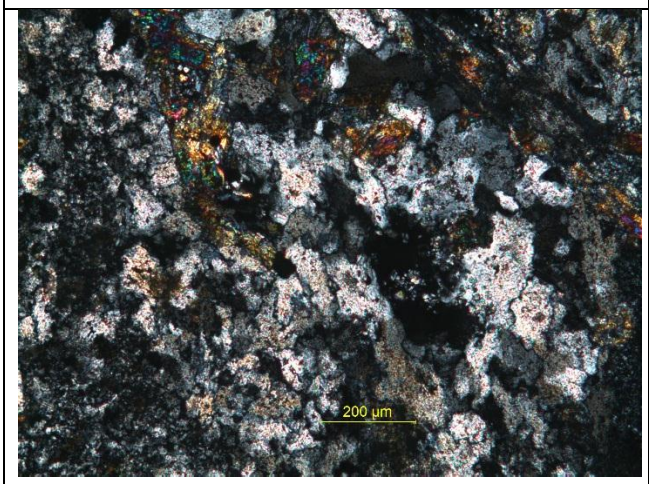

Close up of quartz phenocrysts with large ingrown quartz crystals and epidote

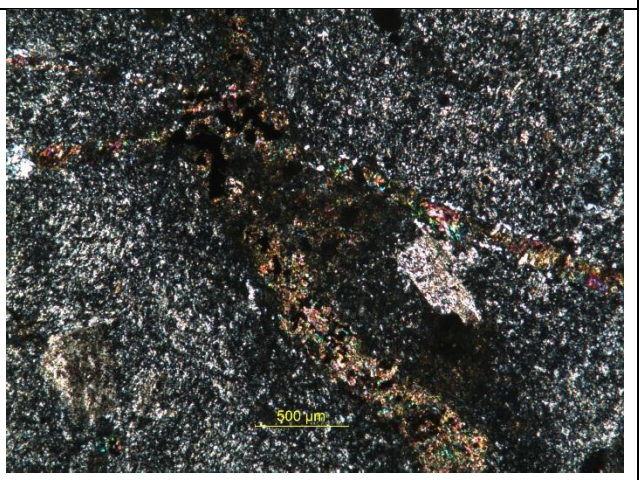

Epidote veining within a volcaniclastic lithic fragment

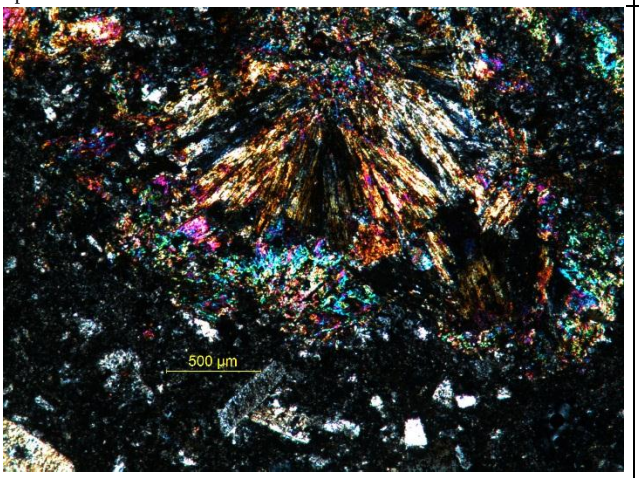

Radial epidote

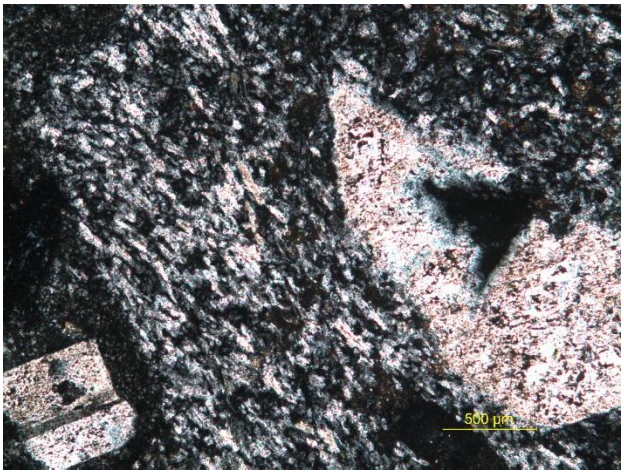

Volcanic lithic with flow directions?

NM 1477.2 mbgl

Well: NM4	Unit: Tahorakuri Formation
Depth: 1477.2 mbgl	Lithology: Volcaniclastic lithic tuff
Associated thin sections: TS13	Sample Names: NM4 1477.2 A

Sample Description:

Dark grey with minor black speckles. Visible lithic fragments dark grey to light grey, up to 3mm in size, sub angular to sub rounded.

Thin section

Interlocking quartz crystal matrix. Quartz veins. Angular opaques with many being perfect squares and rectangles, suspected pyrite. Some observable fractures within the groundmass in cross polarised light.

Minerals present	**Abundance**
Quartz	Major
Opaques	Trace
Sericite	Minor
Clay	Trace
Major = 51-100%, Minor = 10-50%, Trace = <5%	

NM8a 3280-3284.7 mbgl

Well: NM8a	Unit: Ngatamariki Intrusive Complex
Depth: 3280-3284.7 mbgl	Tonalite
Associated thin sections: TS14,15	NM82 3280 C, NM8a 3284.7 C

Sample Description:

Light grey speckled black and white. No visible fracturing, hard.

Thin section

Interlocking quartz crystal groundmass. Large quartz (up to 5mm) phenocrysts are sub-rounded to rounded, highly fractured and showed resorption textures. The Plagioclase crystals appear highly altered. Opaques are clustered near chlorite crystals. Phenocrysts appear glomerporphyritic.

Minerals present	**Abundance**
Quartz	Major
Plagioclase	Minor
Chlorite	Trace
Epidote	Trace
Opaques	Trace
Major = 51-100%, Minor = 10-50%, Trace = <5%	

NM2 1354.2-1354.4 mbgl

Well: NM2	Unit: Tahorakuri Formation
Depth: 1354.2-1354.4 mbgl	Lithology: Tuff
Associated thin sections: TS16,17,18	Sample Names:NM2 1354.2 A,B NM2 1354.4A

Sample Description:

Light grey with visible lithic fragments up to 2mm in size. Lithics appear dark grey to light grey, sub-rounded to angular. Visible void spaces and relatively weak (can be scratched with finger nails).

Thin section

Extremely fine quartz/plagioclase groundmass. Angular plagioclase phenocrysts, devitrified glass and spherulites structures with the groundmass. Phenocrysts primarily sub-rounded quartz and plagioclase. Visible pore space due to washout during thin sectioning process

Minerals present	**Abundance**
Quartz/feldspar? (groundmass)	Major
Calcite	Minor
Quartz (phenocrysts)	Minor
Plagioclase (phenocrysts)	Minor
Opaques	Minor-Trace
Epidote	Minor-trace
Major = 51-100%, Minor = 10-50%, Trace = <5%	

NM3 1743 mbgl

Well: NM3	Unit: Tahorakuri Formation
Depth: 1743 mbgl	Lithology: Volcaniclastic
Associated thin sections: TS19,20	Sample Names NM3 1743 A,C

Sample Description:

Greeny grey groundmass with green lithic fragments (<3mm). Trace black "sparkley" mineral in groundmass

Thin section

Cryptocrystalline quartz feldspar groundmass. Large (<2mm) quartz lithic fragments, rounded to sub-rounded with some showing resorption. Calcite veins and cubic opaques also observed. Visible vesicles in cross polarised light.

Minerals present	**Abundance**
Quartz/Feldspar (groundmass)	Major
Quartz	Minor
Plagioclase	Minor
Epidote	Trace
Opaques	Minor-Trace
Calcite	Minor-Trace
Major = 51-100%, Minor = 10-50%, Trace = <5%	